Stony Brook University

Nuclear Quantum Effects in Ice Phases and Water from First Principles Calculations

A Dissertation presented

by

Betül Pamuk

to

The Graduate School

in Partial Fulfillment of the

Requirements

for the Degree of

Doctor of Philosophy

in

Physics

Stony Brook University

August 2014

Stony Brook University

The Graduate School

Betül Pamuk

We, the dissertation committee for the above candidate for the

Doctor of Philosophy degree, hereby recommend acceptance of this dissertation

María Victoria Fernández Serra - Dissertation Advisor
Associate Professor, Department of Physics and Astronomy

Peter W. Stephens - Chairperson of Defense
Professor, Department of Physics and Astronomy

Joanna Kiryluk - Committee Member
Assistant Professor, Department of Physics and Astronomy

Yan Li - Outside Member
Associate Scientist, Brookhaven National Laboratory

This dissertation is accepted by the Graduate School

Charles Taber
Dean of the Graduate School

Abstract of the Dissertation

Title of Dissertation

by

Betül Pamuk

Doctor of Philosophy

in

Physics

Stony Brook University

2014

Despite the simplicity of the molecule, condensed phases of water show many physical anomalies, some of which are still unexplained to date. This thesis focuses on one striking anomaly that has been largely neglected and never explained. When hydrogen (^{1}H) is replaced by deuterium (^{2}D), zero point fluctuations of the heavy isotope causes ice to expand, whereas in normal isotope effect, heavy isotope causes volume contraction. Furthermore, in a normal isotope effect, the shift in volume should decrease with increasing temperature, while, in ice, the volume shift increases with increasing temperature and persists up to the melting temperature and also exists in liquid water.

In this dissertation, nuclear quantum effects on structural and cohesive properties of different ice polymorphs are investigated. We show that the anomalous isotope effect is well described by first principles density functional theory with van der Waals (vdW-DF) functionals within the quasi-harmonic approximation. Our theoretical modeling explains how the competition between the intra- and inter-molecular bonding of ice leads to an anomalous isotope effect in the volume and bulk modulus of ice. In addition, we predict a normal isotope effect when ^{16}O is replaced by ^{18}O, which is experimentally confirmed. Furthermore, the transition from proton disordered hexagonal

phase, ice Ih to proton ordered hexagonal phase, ice XI occurs with a temperature difference between ^{1}H and ^{2}D of 6K, in good agreement with experimental value of 4K. We explain, for first time for that this temperature difference is entirely due to the zero point energy.

In the second half of this thesis, we expand our study to the other ice phases: ice Ic, ice IX, ice II, ice VIII, clathrate hydrates, and low and high density amorphous ices. We employ the methodology that we have developed to investigate the isotope effect in structures with different configurations. We show that there is a transition from anomalous isotope effect to normal isotope effect in these structures as the density increases. We analyse the bonding mechanism of these structures and make links to the most important anomalies of liquid water.

To my family...

Table of Contents

Contents

List of Figures

List of Tables

Acknowledgements

This thesis would not be possible without contributions from several people. First and foremost, I would like to thank my advisor, Marivi Fernández-Serra, because she is the most important person who made this thesis possible. I owe Marivi who I am as a researcher. She has been my source of inspiration for all these years that I have worked with her. I have looked up to her, and I hope to be like her some day. Every time we had a discussion in her office, when I left that room, I thought to myself that I am doing the right thing, because those discussions kept me excited for my research. She has always been open to my questions, very patient with explaining my mistakes, and has always come up with the most elegant ideas. Looking back, I realise how much I have learned from her for all these years, and I thank her for intellectually transforming me to whom I have become today. In addition, I would like to thank Marivi, Matt, Skylar and Tag for making life in Stony Brook more enjoyable. I will miss Matt's jokes, and I will miss running all around their garden with Skylar and Tag.

I would also like to thank Phil Allen for co-advising me throughout our projects. I have learned a lot from his infinite experience, as he very patiently explained and discussed my research with me. I would also like to thank our collaborators, Peter Stephens, for doing the experiments of ^{18}O, and Rafael Ramírez and Carlos Harrero, for doing the PIMD simulations. Their contributions made my first paper very valuable. I also thank Peter Stephens for being there for me during the hooding ceremony and Phil joining me at the department convocation ceremony. I would also like to thank the thesis committee members, Yan Li, and Joanna Kiryluk for evaluating my thesis. In addition, I would also like to thank my professors from Bilkent University, but especially Tuğrul Senger for giving me the first flavour of what doing research means.

I would like to thank our postdoc Luana, for doing her best in answering my endless questions, and there were a lot of them. I have learned a lot from her. Also, I should thank all my office mates in all these years, Adrien, Jue, Li, Sriram, Judith, Michelle, Dan, Adrian, Simon, Jian, and Jonathan, for sharing an office with no windows with me and making it an enjoyable place to go to, every day. Thanks Michelle, Cip, Dan, and Rahul for proofreading

parts of this thesis. Michelle, I am sure, we will see each other soon in Europe. I should especially not forget to thank Sriram and Luana for my coffee addiction, because all those discussions as well as the jokes we had over coffee made me a real physicist.

Next I would like to thank all the friends I have made during these years in Stony Brook. Especially, I would like to thank Cip and David, for knowing them has been a lot of fun, and also, it is good to know that I have friends when I need a hug.

I also thank Shawn, Karin and Josh, for being my room mates here in the second year. And Karin, thanks for including the experience of being a maid of honour into the memories I have from Stony Brook. And Rahul, you have become like a cousin that I enjoy hanging out with all the time.

Heli, Sriram and Divya, your friendship means a lot, and I am sure we will have many more travels to come, since this is a big world to see. Also, Giulia, Tatsiana, Vasily, and especially Sriram and Divya, thanks for making our travel to India and your wedding an unforgettable experience.

I thank the Brazilians: Luana, Gustavo, Gabriel, and Jose (!) for showing me that two countries can be exactly the same even if there is an ocean in between. And thanks Stalin for introducing me to a lot of fun people other than physicists.

Thanks to Masatoshi for teaching me how to dance tango, for dancing has always been the greatest pleasure for me, and it is a passion I would like to keep. And Panagiotis, thanks for being a fun dancing partner.

I would also like to thank my friends from Bilkent, for I will never forget all those hours of doing homework and studying for the exams with Onur and Barış, and once we are done, meeting with the rest of the group, Özgun, Ozan, Zeynep, Ceren, Anıl, İzzet, Can at MSSF for the fun part of the night. I should also thank Onur, Anil for making our exchange in Lund a very much fun time to remember. Thanks Utku, Coşkun and Ceren, for showing that a phone call is enough for meeting up, despite all the distances in time and place.

Finally, I should thank all my family for their never-ending support. I should start with thanking Dave and Dee, for they have become my American family, during these years I have spent living in the US. From the very beginning, they have welcomed me into their life, inviting me to all family dinners and other fun events. Thank you for being there as my family during the graduation ceremony and we will always be in touch.

I would like to thank Murat's family, for they have become my family

during these years. I thank them for sharing my excitement for my studies.

Special thanks to Hale Ablam and Haluk Amcam, for they are family, too. They have been my first teachers of maths, have gotten me interested in science, and have played a crucial role in my development as an intellectual human being. But more importantly, I will never forget the vacation trips and the Sundays of cooking, eating, drinking, reading, listening to the music, and dancing we did as the super 5. Those are the moments I most cherish from my childhood.

Most importantly, of course, I would like to thank my own family, my parents. There is no real good way of thanking them, for I owe them who I really am. I thank my father for teaching me how to be a completely intellectual person and I thank my mother for her endless passion and ambition, without those I would not be able to complete this thesis. They have always wanted the best from me, and at the same time supported me no matter what, always believing in me. En önemlisi, tabii ki kendi aileme, anneme ve babama teşekkür etmek istiyorum. Onlara teşekkür edebilmenin doğru bir yolu yok, çünkü kim olduğumu onlara borçluyum. Babama, bana tam anlamıyla entellektüel bir insanın nasıl olacağını öğrettiği için, anneme ise bitmek tükenmek bilmeyen tutkusu ve hırsı için teşekkür ederim, onlar olmasa bu tezi tamamlayamazdım. Benden hep en iyisini istediler ve aynı zamanda her ne olursa olsun bana inanarak, beni hep desteklediler.

Lastly, I thank my partner for life, Murat, because I know there is at least one person in this world who has read all of this thesis. Thank you Murat, for holding my hand and following me no matter where I go. Only you could have been the one. I thank you for being yourself and loving me for who I am. Without you, I would not be where I am today.

1 Introduction

Water is the matrix of life. Our lives depend on it. As humans, we have been interacting with water, since the very beginning of our existence. Yet, we still do not have a full understanding of it. The structure of water under different conditions is still puzzling the scientists. Water does not behave like most materials, and its properties are different than normally expected. Each unexpected behaviours is an anomaly of water, which make understanding this liquid very difficult.

In order to interpret the properties of solid ice, liquid water, and gaseous vapour, we first need to understand the structure of a water molecule and how it bonds to its neighbours. Water is composed of hydrogen and oxygen atoms, as was established by the experiments of Cavendish and Lavoisier in the 1780s. Gay-Lussac and Humboldt discovered that its structure is one volume of oxygen to two volumes of hydrogen, H_2O. The ratio of the weights of hydrogen and oxygen was found by Dumas in 1842 as close to 2 to 16. As other stable isotopes (with different atomic masses) of hydrogen and oxygen were discovered, it was established that naturally occurring water is a mixture of different isotopes of hydrogen (^{1}H), deuterium(^{2}H or D), tritium (^{3}H or T), and oxygen ^{16}O, ^{17}O, and ^{18}O.

The intra-molecular bonds of a water molecule are such that each hydrogen atom of the molecule are covalently bonded to the oxygen atom, forming an OH bond. The most simplistic model to understand the electronic structure of a water molecule is to put point charges in agreement with the experimentally observed OH bond lengths and angles and the magnitude of the point charges are modified to reproduce experimental properties such as the dipole moment. However, this model does not take into account how the atomic orbitals are modified as the atoms are brought in contact. In water, the oxygen atoms have two occupied molecular orbitals, called lone-pairs, which are pointed away from the hydrogen atoms and perpendicular to the molecular plane. There exist more complex force field models that are fitted to reproduce properties of water at certain points of the phase diagram, and a few of these that are employed in this dissertation will be introduced in the Chapter 2.

The dominant intermolecular bond that connects a water molecule to its neighbouring molecules is the "hydrogen bond". The lone pair orbitals of the oxygen atom are negatively charged and attract the positively charged

hydrogen atoms of the next molecule. The positions of the lone-pairs of the oxygen and the covalent bond are consistent with the tetrahedral structuring of the liquid water and ice. Therefore the hydrogen of one water molecule points, in general, towards the oxygen of the neighbouring water molecule. The OH–O hydrogen bonding (Hbond) can be considered a weak covalent bond [15].

Furthermore, the dipole-dipole fluctuations of the molecules lead to long-range forces, that are called "van der Waals" forces which become important in the bonding mechanism of liquid water. Van der Waals bonds (vdW bonds) contribute to the structuring of water, even if there is a non-bonding configuration. This type of configuration, in a simplistic picture, is when the oxygen atoms of liquid water point towards each other without a linking hydrogen in between. The complexity of these bonds are well incorporated in density functional theory, which will be introduced in Chapter 2, as well.

Understanding the bonding mechanism of water is the key to interpreting the anomalies of water. It is not possible to go through every single one of these anomalies, as it is beyond the scope of this dissertation, but in this chapter, we will introduce some of the relevant and recently debated anomalies.

One of the most well known anomalies is the fact that ice floats on water. As liquid water freezes to form its solid phase, ice, it expands. Normally, during freezing, the disordered molecules of a liquid form an orderly stacked structure, which results in decreasing the volume, hence increasing the density of the material. However, during freezing under ambient conditions, the disordered liquid water molecules order themselves to form ice, such that the ice molecules bond together to form a hexagonal structure. Ice prefers to form a hexagonal structure, because each molecule can make a hydrogen bond with its neighbours obeying the electrostatic forces of the covalency of its inter- and intra-molecular bonds explained above. Details of this hexagonal structure of ice are the topics of Chapters 3, 4, and 5. The general idea behind ice floating on liquid water is that the hexagonal ice has voids between its molecules, which are called the interstitial site. Forming these interstitial sites results in an expansion of volume and a decrease in the density during freezing, causing ice to float on liquid water.

However, liquid water does not always freeze immediately to solid ice. Liquid water to solid hexagonal ice is a phase transition between two stable phases, but liquid water can go into a metastable phase during cooling. It is possible to cool liquid water below its freezing temperature, as it goes

into this metastable phase, and this is called "supercooled" water. Because supercooled water is metastable, it freezes into ice under any perturbation, making this phase very difficult to probe. As the temperature decreases from liquid water into the metastable phase, the supercooled water stays liquid until $\sim$ 228 K, after which it freezes. One can also obtain glassy ice states that retain the disordered structure of liquid water. These states are called amorphous ices, and they exist in two different densities. A general idea about the structure of amorphous ices will be introduced in Chapter 6 of this dissertation. If the temperature of amorphous ices are increased, an ultraviscous liquid is formed around $\sim$ 150 K. However, it is not possible experimentally to probe supercooled water between these temperatures, and this part of the phase diagram is called "no man's land".

Understanding the supercooled water is important because the response functions of water diverge in this regime. For example, typically, the specific heat, thermal expansion coefficient, and isothermal compressibility are expected to decrease with temperature monotonically. Experimentally, it is known that temperature dependence of specific heat of liquid water has a minimum [16] and then it increases sharply in the supercooled regime [17]. The thermal expansion coefficient of water becomes negative at the temperature of maximum density [18] and diverges at $\sim$ 228K [17]. The isothermal compressibility has a minimum [18] and again diverges at $\sim$ 228K in the supercooled region of the phase diagram [17]. One should also note that these temperatures are different for normal water (H_2O) and heavy water (D_2O); the temperature of specific heat minimum is $\sim$ 310K for H_2O and $\sim$ 330K for D_2O [16], the temperature of maximum density is $\sim$ 277K for H_2O and $\sim$ 284K for D_2O [18, 19], and the temperature of isothermal compressibility minimum is $\sim$ 320K for H_2O and $\sim$ 322K for D_2O [18].

One of the challenges is explaining these anomalously diverging response functions in the supercooled phases, because it is especially difficult to reproduce the experimentally measured anomalies with theoretical simulations. Even though some of the anomalies are reproduced with molecular dynamics or Monte Carlo simulations using empirical force field models, there are quantitative differences between different models [20–23]. In addition, it is still unclear whether these empirical force field models can capture the correct physics of hydrogen bonds in ice and water [6]. To explain these anomalous responses in the supercooled region, the existence of a phase transition between high density and low density liquids with a liquid-liquid critical point has been hypothesized using empirical force field models. [24]. There

are many studies in the supercooled [25–28] and high temperature [21, 23] regimes. Although some of the simulations find this second critical point [27–30], it is not settled that the second critical point is a model independent feature [25, 31–35]. Therefore, there is a clear need for an insight from quantum calculations, such as density functional theory [36].

Although our story will come back to these anomalies eventually, it begins with a completely different anomaly of water and ice. The volume of a material decreases with decreasing temperature. As the temperature decreases and gets close to $T = 0$ K, the volume deviates from a linear decrease. This deviation is due to the quantum vibrations of the nuclei, and the volume of different ions can be distinguished by the energy of vibrations around zero-point, which is directly linked to their mass. Normally, the phonon vibrations of the heavy isotope are smaller and more localized than those of the light isotope. Therefore, the volume of the heavy isotope is smaller than the volume of the light isotope, which is a way to interpret how nuclear quantum effects play a role in the structure of a material. This is the case, for example, for neon, where ^{22}Ne has smaller lattice parameter than ^{20}Ne. The volume of ^{20}Ne expands by 0.6% with respect to ^{22}Ne at the zero-point [37]. This "normal" isotope effect corresponds to a ∼12% zero-point expansion of ^{20}Ne relative to a hypothetical "classical" or "frozen" lattice [38, 39]. Since H_2O and Ne have similar molecular masses, one might expect similar effects. However, the volume of normal ice, H_2O at $T = 0$ is ∼0.1% smaller than that of heavy ice, D_2O [3, 40]. It has rarely been mentioned in the literature that this is opposite of the usual behavior, and no explanation has been offered. Chapters 3 and 4 of this dissertation give an explanation for this anomaly in hexagonal ices.

Furthermore, this anomalous isotope effect in hexagonal ice does not diminish with increasing temperature, as normally expected, but the volumes of H_2O and D_2O get separated close to the melting point, causing an increase in the anomalous isotope effect with increasing temperature. The anomalous inverse isotope effect persists in liquid water up to the boiling point, where the molecular volume of H_2O is smaller than that of D_2O[1, 18] at all temperatures.

Fig. 1 shows experimental results for volume per molecule and isothermal bulk modulus for liquid water. The figure is replotted using reference [1] eq. 34, 38, and 41 for volumes and the corresponding equations of compressibility eq. 35 and 39 for bulk modulus. These equations are derived to fit the results from different experiments with minimum deviation. It is

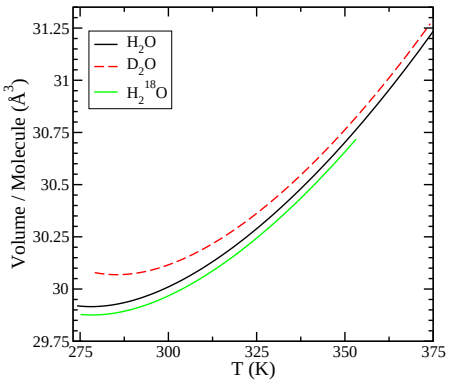

(a) Volume per molecule of liquid water for different isotopes.

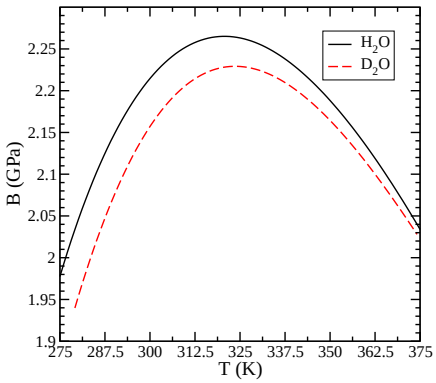

(b) Bulk modulus of liquid water for different isotopes.

Figure 1: Isotope effect on the volume per molecule and bulk modulus of liquid water, replotted using Ref. [1] eq. 34, 38, and 41 for volumes and eq. 35 and 39 for bulk modulus.

clearly stated that the difference between the equation for H_2O and D_2O is only due to the isotope change in the hydrogen atoms, so these results can be trusted to show the isotope effect in the liquid. Therefore, it is clear that the isotope effect persists in liquid water up to the boiling temperature; we can distinguish the volumes of different isotopes. It is anomalous for the replacement of H with D; the volume increases, and the bulk modulus decreases. However, it is normal for the replacement of $H_2{}^{16}O$ with $H_2{}^{18}O$; the volume decreases. These results also show the isotope effect in the temperature for the compressibility minimum in Fig. 1b. The compressibility minimum is at $T = 321$ K for H_2O, while it is slightly larger at $T = 324$ K for D_2O from Ref. [1].

This anomaly is linked to the interplay between the intramolecular covalent bonds and the intermolecular Hbonds of water. Numerous recent studies [2, 11, 41–45] address the contribution of zero-point nuclear quantum effects to the structures of ice and water. The issue is delicate, because of the peculiar electrostatic-covalent nature [15] of the hydrogen bond (Hbond) in water.

It is well known that hydrogen bonded materials show an anti-correlation [46] effect between the OH covalent bond and the OH–O Hbond. As the OH–O distance diminishes, the OH covalent bond weakens (its length increases and vibrational frequency diminishes [47, 48]) while the OH–O Hbond does

the opposite. Therefore, it is expected to observe an anomalous isotope effect in Hbonded materials that present this anticorrelation between intra- and inter-molecular bonds. However, the isotope effect diminishes with increasing temperatures in these structures; for example the anomalous isotope effect between KD_2PO_4 and KH_2PO_4 converges around $T \sim 300$ K, and becomes normal [49]; while it is divergent in ice and still exists up to the boiling point in liquid water. Because it is more complicated to define and analyse Hbonds and OH covalent bonds in liquid water, we turn to ice to understand how nuclear quantum effects change this anti-correlation between these bonds.

Ice has a rich phase diagram with 16 different crystalline phases, which mainly originates from the polymorphism of water. This polymorphism is another result of the uniqueness of the bonding mechanism of the water molecule. In each of the following chapters, we will investigate several of these crystalline phases to understand how nuclear quantum effects change the structure of ices and liquid water.

Another source of richness of the phase diagram is due to the availability of different proton configurations that satisfy Bernal-Fowler "ice-rules" [50]. This leads to additional phase transitions between proton ordered and proton disordered configurations, as a result of a balance between different energies of possible proton configurations and residual entropy, estimated by Pauling [51]. We start our investigation with hexagonal ices, ice Ih and ice XI, where the isotope effect is known to be anomalous from experiments [3, 40]. Applying the methodology we have developed, we investigate the source of this anomalous isotope effect in Chapter 3. Furthermore, we analyse the differences in the structural properties of proton ordered ice XI and proton disordered ice Ih, in terms of lattice parameters, anisotropy of the bulk modulus, and investigate the anomalous isotope effect in the total bulk modulus of these systems in Chapter 4. As we understand the structures of proton ordered and disordered hexagonal ices, we also can use our methods to obtain: i) which phase is the most stable at the zero temperature limit, ii) if there is a phase transition predicted by our theory iii) how the isotope effects change this transition temperature. Experimentally it is known that the transition temperature of D_2O is 4 K larger than H_2O [52, 53], and in Chapter 5, we will show that *ab initio* DFT is a good candidate to predict this isotope effect in agreement with these experimental results.

Once we show that our methodology is a good candidate to investigate hexagonal ices in detail, we move on to different polymorphs of ice. In each section of Chapter 6, we analyse the isotope effect in different ice polymorphs.

We start by cubic ice Ic, which has a structure similar to that of ice Ih. We investigate and reproduce the experimentally shown anomalous isotope effect in clathrate hydrates [5]. Then we move on to high pressure ice phases, ice IX, ice II, and ice VIII. We show that as the density of the ices increase, there is a transition from anomalous to normal isotope effect. Lastly, we analyse amorphous ices, where there is no underlying lattice and the long range order vanishes, which is similar to what happens in liquid water.

In the conclusion, Chapter 7, all the results are summarised, and one last analysis of the bonding mechanism of all the investigated structures is performed. Finally, we return back to Fig. 1, and make links to the above mentioned anomalies of liquid water.

2 Theory

This chapter will focus on the theory and the approximations that will be used throughout this thesis. Although the understanding and development of *ab initio* density functional theory could be a topic of a whole dissertation, we will give a broad introduction to the theory for the sake of completeness. This inclusion is important as DFT is applied in all of the calculations of this thesis. Ref. [54] will be mostly followed for the introduction to the many body theory and DFT. In addition, a general introduction to the two force field models of liquid water, qTIP4P/F and TTM3-F, that have been employed and a comparison of them to DFT will also be given. Then, the phonon calculations and how these calculations are used to obtain Helmholtz free energy with the quasi-harmonic approximation will be explained in the second half of this chapter.

2.1 Introduction to Many Body Theory

Condensed matter systems can be understood by solving the quantum mechanical Schrödinger equation for interacting electrons and nuclei. In the most general form, the Hamiltonian of interacting particles is,

$$\begin{aligned} \hat{H} &= -\frac{\hbar}{2m_e}\sum_i \nabla_i^2 + \sum_{i,I}\frac{Z_I e^2}{|\mathbf{r_i}-\mathbf{R_I}|} + \frac{1}{2}\sum_{i\neq j}\frac{e^2}{|\mathbf{r_i}-\mathbf{r_j}|} \\ &\quad -\sum_I \frac{\hbar^2}{2M_I}\nabla_I^2 + \frac{1}{2}\sum_{i\neq j}\frac{Z_I Z_J e^2}{|\mathbf{R_I}-\mathbf{R_J}|} \\ &= \hat{T}_e + \hat{V}_{eI} + \hat{V}_{ee} + \hat{T}_I + \hat{V}_{II} \end{aligned} \tag{1}$$

where i and j runs over the electrons and I and J runs over the nuclei in the system, m_e and M_I are the masses of the electron and the nuclei respectively, and Z_I represents the nuclear charge. The first term corresponds to the kinetic energy of the electrons, $\hat{T}_e$. The second term is the interaction of the electrons with the nuclei, $\hat{V}_{eI}$, which can be considered as an external potential when we are solving for the electronic energy of the system. Therefore, when we refer to the external potential V_{ext}, this term will be included as well as any other additional potential energy due to an external field. The third term is the Coulomb interaction between the electrons, $\hat{V}_{ee}$ while the

last term is the Coulomb interaction between the nuclei, $\hat{V}_{II}$.The fourth term is the kinetic energy of the nuclei in the system, $\hat{T}_I$.

For a condensed matter system, it is not possible to solve this equation exactly. This is because the many body interactions become more complicated, as the number of particles increases. Therefore, at this point we make approximations to solve the Schrödinger equation for this Hamiltonian. The inverse mass of the nuclei is small compared to the other terms of the Hamiltonian, therefore the mass of the nuclei can be set to infinity and the kinetic energy of the nuclei can be neglected. This is called the Born-Oppenheimer (BO) or adiabatic approximation. Another way of observing BO approximation is by decoupling the Hamiltonian of the kinetic energy of the nuclei from the rest of the Hamiltonian, let us call this the electronic Hamiltonian, i.e $\hat{H} = \hat{T}_I + \hat{H}_e(\mathbf{r}, \mathbf{R})$. Therefore, one can solve the electronic Hamiltonian using the positions of the nuclei as a parameter. And the quantum mechanics due to the kinetic energy of the nuclei can, in principle, be added at any point, if desired.

For the rest of this thesis, BO approximation will be employed in all DFT calculations. However, one must note that this approximation works best for heavy nuclei, and as the atomic nuclei becomes smaller, the error from this approximation starts to become important. Hydrogen is the atom with the smallest mass, therefore the quantum effects due to the nuclei become important in systems with hydrogen, such as water and ice. One way to overcome this problem is to use path integral molecular dynamics [43]. In this thesis, we will consider the nuclear quantum effects by obtaining the phonon energies as will be explained in the following sections.

2.2 Hartree and Hartree-Fock Approximation

Instead of solving the interacting particle system, another simplification is considering non-interacting electrons in an effective external field from the nuclei. Then one can solve time independent Schrödinger equation for N independent one-electron Hamiltonian, instead of solving the Schrödinger equation of N-electron Hamiltonian.

$$\hat{H}_{eff}\psi_i(\mathbf{r}) = \left[-\frac{\hbar}{2m_e}\nabla^2 + V_{eff}(\mathbf{r})\right]\psi_i^\sigma(\mathbf{r}) = \varepsilon_i^\sigma\psi_i^\sigma(\mathbf{r}) \tag{2}$$

In the non-interacting scheme of the electrons, the total energy and the total density can be written in terms of the sum of the values of individual

electrons: $E = \sum_i \varepsilon_i$ and $n(\mathbf{r}) = \sum_i |\psi_i(\mathbf{r})|^2$.

In the Hartree level of the approximation, one can solve for the classically interacting electrons. Then Fock introduced the Pauli exclusion principle by orthogonalizing the electron wave function and setting the ground state wave function equal to a Slater determinant of single electron wavefunctions of spin-orbitals, $\phi_i(\mathbf{r_j}, \sigma_j)$, which are the product of position $\psi_i^\sigma(\mathbf{r_j})$ and function of spin:

$$\Phi = \frac{1}{N!^{1/2}} \begin{vmatrix} \phi_1(\mathbf{r_1}, \sigma_1) & \phi_1(\mathbf{r_2}, \sigma_2) & \phi_1(\mathbf{r_3}, \sigma_3) & ... \\ \phi_2(\mathbf{r_1}, \sigma_1) & \phi_2(\mathbf{r_2}, \sigma_2) & \phi_2(\mathbf{r_3}, \sigma_3) & ... \\ \phi_3(\mathbf{r_1}, \sigma_1) & \phi_3(\mathbf{r_2}, \sigma_2) & \phi_3(\mathbf{r_3}, \sigma_3) & ... \\ . & . & . & ... \end{vmatrix} \tag{3}$$

The expectation value of the independent electron Hamiltonian becomes,

$$\begin{aligned} < \Phi|\hat{H}|\Phi > \; = \; & \sum_{i,\sigma} \int d\mathbf{r} \psi_i^{\sigma *}(\mathbf{r}) \left[-\frac{1}{2}\nabla^2 + V_{ext}(\mathbf{r}) \right] \psi_i^\sigma(\mathbf{r}) + E_{II} \\ & + \frac{1}{2} \sum_{i,j,\sigma_i,\sigma_j} \int d\mathbf{r} d\mathbf{r}' \psi_i^{\sigma_i *}(\mathbf{r}) \psi_j^{\sigma_j *}(\mathbf{r}') \frac{1}{|\mathbf{r} - \mathbf{r}'|} \psi_i^{\sigma_i}(\mathbf{r}) \psi_j^{\sigma_j}(\mathbf{r}) \\ & - \frac{1}{2} \sum_{i,j,\sigma} \int d\mathbf{r} d\mathbf{r}' \psi_i^{\sigma *}(\mathbf{r}) \psi_j^{\sigma *}(\mathbf{r}') \frac{1}{|\mathbf{r} - \mathbf{r}'|} \psi_j^{\sigma}(\mathbf{r}) \psi_i^{\sigma}(\mathbf{r}') \end{aligned} \tag{4}$$

The first terms of this equation involve the kinetic energy of the electrons, the potential due to the external fields, from the nuclei and other fields, and the nuclei-nuclei Coulomb interaction energy. The important improvement comes from the second and the third terms of this equation. The second term involves the direct interaction of the electrons with each other; electron i at position $\mathbf{r}$ directly interacts with the electron j at position $\mathbf{r}'$. The third term involves the exchange interaction, where the electron i at position $\mathbf{r}$ exchanges position with the electron j at position $\mathbf{r}'$. Then the corresponding

Schrödinger equation for the electronic part becomes,

$$\left[-\frac{1}{2}\nabla^2 + V_{ext}(\mathbf{r}) + \underbrace{\sum_{j,\sigma_j}\int d\mathbf{r}'\psi_j^{\sigma_j *}(\mathbf{r}')\psi_j^{\sigma_j}(\mathbf{r}')\frac{1}{|\mathbf{r}-\mathbf{r}'|}}_{\hat{V}_{Hartree}} \right. \tag{5}$$

$$\left. \underbrace{-\sum_{j}\int d\mathbf{r}'\psi_j^{\sigma *}(\mathbf{r}')\psi_i^{\sigma}(\mathbf{r}')\frac{1}{|\mathbf{r}-\mathbf{r}'|}\frac{\psi_j^{\sigma}(\mathbf{r})}{\psi_i^{\sigma}(\mathbf{r})}}_{\text{Exchange: } \hat{\mathrm{V}}_{\mathrm{x}}^{\mathrm{i},\sigma}} \right] \psi_i^{\sigma}(\mathbf{r}) = \varepsilon_i^{\sigma}\psi_i^{\sigma}(\mathbf{r})$$

This is a direct result of the Slater determinant form of the wave function, which makes it antisymmetric, agreeing with the fact that electrons are fermions, and therefore it automatically satisfies the Pauli exclusion principle. While this takes care of the additional energy from the exchange of the electrons, all correlation effects other than the Pauli exclusion are neglected in this approximation.

2.3 Exchange and Correlation Hole

The non-interacting particle scheme is missing the correlation effects due to the interactions of the electrons. For simplicity, let us consider the two-body interactions only. For a completely non-interacting particle scheme, because the probabilities are not correlated, the probability of finding an electron at position $\mathbf{r}$ with spin σ and at position $\mathbf{r}'$ with spin σ' is just the product of individual probabilities: $n(\mathbf{r},\sigma)n(\mathbf{r}',\sigma')$. Therefore, we can separate this from the probability of the interacting particle scheme to obtain the probabilities due to the correlations only:

$$\Delta n(\mathbf{r},\sigma;\mathbf{r}',\sigma') = n(\mathbf{r},\sigma;\mathbf{r}',\sigma') - n(\mathbf{r},\sigma)n(\mathbf{r}',\sigma') \tag{6}$$

Let us now concentrate on the change in the energy when the interactions between the electrons due to Pauli exclusion principle is introduced with Hartree-Fock approximation (HF) on top of the non-interacting Hartree approximation. With further investigation of the exchange term of the Hartree-Fock equation, one can see that in addition to satisfying the Pauli exclusion

principle, this term introduces a subtraction of the self interactions of the electrons that is included in the Hartree part of the equation. This can be thought as the interaction of an electron with a positive exchange hole that surrounds it, resulting in a lowering of the Hartree energy from the direct interaction of the electrons. As a result, the exchange hole can never be positive and because one electron cannot be at $\mathbf{r}$ and $\mathbf{r}'$ at the same time, the integration of the $n_x(\mathbf{r}, \sigma; \mathbf{r}', \sigma')$ over all $\mathbf{r}'$ is exactly one missing electron at position $\mathbf{r}$.

Now, we can separate the pair correlation function into exchange and correlation terms:

$$\Delta n(\mathbf{r}, \sigma; \mathbf{r}', \sigma') = n_{xc} = n_x(\mathbf{r}, \sigma; \mathbf{r}', \sigma') + n_c(\mathbf{r}, \sigma; \mathbf{r}', \sigma') \tag{7}$$

The integration of the correlation hole must be zero, because the total pair correlation function integrates to one. Therefore, it is a redistribution of the density of the hole. This term becomes important for electrons with the opposite spin, since electrons with the same spin are already taken care of by the exchange term via the exclusion principle. An example of correlation effects would be screening, where the collective correlation of the electrons reduce the interaction between any two electrons; which is especially an important effect in metallic systems. The correlation effects are much harder to calculate and incorporate in the approximations, because they include both kinetic and potential interactions of the system. How the exchange and correlation terms are approximated in DFT will be briefly explained in the following sections.

2.4 Introduction to DFT

2.4.1 Homogeneous Electron Gas

The idea of treating electronic energy as a functional of its density was first introduced by Thomas and Fermi in 1930 [54, 55]. They have treated only the kinetic energy of the free electron gas, by obtaining the energy density, $\epsilon = \frac{1}{4\pi^3} \int_{k<k_F} d\mathbf{k} \frac{\hbar^2 k^2}{2m_e} = \frac{1}{\pi^2} \frac{\hbar^2 k_F^5}{10 m_e}$, as a functional of the electron density $n = \frac{k_F^3}{3\pi^2}$, where k_F is the Fermi wave vector spanning the occupied one electron levels up to the Fermi surface. Then Dirac also introduced the local exchange among the electrons to the Thomas-Fermi density functional [54, 56] and

ended up with the local exchange and correlation functional.

$$E_{TF}[n] = \frac{3}{10}(3\pi^2)^{2/3}\int d^3r n(\mathbf{r})^{(5/3)} + \int d^3r V_{ext}(\mathbf{r}) - \frac{3}{4}\left(\frac{3}{\pi}\right)^{1/3}\int d^3r n(\mathbf{r})^{(4/3)} + \frac{1}{2}\int d^3r d^3r' \frac{n(\mathbf{r})n(\mathbf{r}')}{|\mathbf{r}-\mathbf{r}'|} \quad (8)$$

where the first term corresponds to the local Thomas-Fermi approximation to the kinetic electron energy, the second term is the external field, the third term is the local correlation energy and the last term is the electrostatic Hartree energy.

Although the Thomas-Fermi-Dirac density functional is a very crude approximation, which lacks detailed correlations of electrons and treats the system locally, this formalism set the foundation for density functional theory. Instead of solving the Schrödinger equation for the energy of interacting electron wavefunctions with many degrees of freedom, one can instead solve for energy as a functional of a smooth electron density, with only three variables. The generalization and the formulation of this idea came with the Hohenberg-Kohn theorems followed by the Kohn-Sham ansatz, which made DFT applicable to different systems.

2.4.2 Hohenberg-Kohn Theorems

Hohenberg and Kohn theorems (HK) develop an exact variational principle for the ground state energy, as a variational functional of electron density $n(\mathbf{r})$ [57].

Theorem 1: For a system of interacting particles in an external potential $V_{ext}(\mathbf{r})$, the potential is uniquely determined by the ground state electron density, $n_0(\mathbf{r})$

The proof of this theorem is done *reductio ad absurdum*. Let us assume that we have two systems, labeled as (1) and (2), with different external potentials with the same electron densities. The ground state energy of the first system,

$$E^{(1)} = \langle\psi^{(1)}|\,\hat{H}^{(1)}\,|\psi^{(1)}\rangle < \langle\psi^{(2)}|\,\hat{H}^{(1)}\,|\psi^{(2)}\rangle \quad (9)$$

is smaller, because the ground state of the second system, $\psi^{(2)}$ is not the ground state of the first system. Rewriting the second part of this equation in terms of the ground state energy of the second system, and the external

potentials,

$$\begin{aligned} \langle\psi^{(2)}|\,\hat{H}^{(1)}\,|\psi^{(2)}\rangle &= \langle\psi^{(2)}|\,\hat{H}^{(2)}\,|\psi^{(2)}\rangle + \langle\psi^{(2)}|\,\hat{H}^{(1)}-\hat{H}^{(2)}\,|\psi^{(2)}\rangle \\ &= E^{(2)} + \int d^3r[V_{ext}^{(1)}(\mathbf{r}) - V_{ext}^{(2)}(\mathbf{r})]n_0(\mathbf{r}) \end{aligned} \tag{10}$$

eq.9 becomes

$$E^{(1)} < E^{(2)} + \int d^3r[V_{ext}^{(1)}(\mathbf{r}) - V_{ext}^{(2)}(\mathbf{r})]n_0(\mathbf{r}) \tag{11}$$

Similarly for the second system we can write:

$$E^{(2)} < E^{(1)} + \int d^3r[V_{ext}^{(2)}(\mathbf{r}) - V_{ext}^{(1)}(\mathbf{r})]n_0(\mathbf{r}) \tag{12}$$

Adding these last two equations, we end up with the contradicting result:

$$E^{(1)} + E^{(2)} < E^{(2)} + E^{(1)} \tag{13}$$

Therefore, two different external potentials cannot give the same ground state energy E_0.

Theorem 2: A universal energy as a functional of the electronic density, $E[n(\mathbf{r})]$, can be defined for any given external potential. For a particular external potential, $V_{ext}(\mathbf{r})$, the global minimum of the energy functional is the ground state energy of the system, and the density that minimizes the energy is the exact ground state density, $n_0(\mathbf{r})$.

For the proof of the second theorem, let us consider the energy functional of a system under external field, where the kinetic and the interaction energy are also uniquely determined as a functional of electron density:

$$E_{HK}[n] = T[n] + E_{int}[n] + \int d^3r V_{ext}(\mathbf{r})n(\mathbf{r}) + E_{II} \tag{14}$$

Following the first theorem, we can consider the ground state density, $n^{(1)}$ corresponding to the external potential $V_{ext}^{(1)}$:

$$E^{(1)} = E_{HK}[n^{(1)}] = \langle\psi^{(1)}|\,\hat{H}^{(1)}\,|\psi^{(1)}\rangle \tag{15}$$

Now, if we consider another density, $n^{(2)}$ corresponding to a different wave function, it follows that the energy of the first state is immediately smaller than the second state:

$$E^{(1)} = \langle\psi^{(1)}|\,\hat{H}^{(1)}\,|\psi^{(1)}\rangle < \langle\psi^{(2)}|\,\hat{H}^{(1)}\,|\psi^{(2)}\rangle = E^{(2)} \tag{16}$$

Therefore, the ground state energy of the system, E_0 is uniquely determined by minimizing the electronic density to the ground state electron density, $n_0(\mathbf{r})$.

Note that these theorems state that if the exact electronic energy functional is known, the exact ground state energy can be obtained by minimizing it with respect to the variations in the electron density. Therefore, DFT is a theory that only concerns obtaining the ground state energy accurately. In addition, HK theorems do not give any insight into the form of the electronic energy functional.

2.4.3 Kohn-Sham Ansatz

The Kohn-Sham ansatz (KS) states that the exact ground state electron density n_0 can be represented by the ground state density of an auxiliary system of non-interacting particles [58]. In this way, the complicated many-body problem is replaced by an independent particle problem with interacting electronic densities. Separating the kinetic and the potential parts, the KS Hamiltonian becomes:

$$\hat{H}^{\sigma}_{aux} = -\frac{1}{2}\nabla^2 + V^{\sigma}(\mathbf{r}) \tag{17}$$

Following HK theorems, for the KS ansatz, it can be stated that, if the ground state density of the system is known, it exactly determines the Kohn-Sham potential, V_{KS}, the interaction between electron densities. Then, solving Schrödinger-like systems of equations for the density functionals, called Kohn-Sham equations, the Kohn-Sham potential, V_{KS}, determines all the states of the system, with its minimum being the ground state. The ground state of non-interacting particles directly leads to the ground state density, closing the cycle of HK theorems.

KS equations lead to a ground state energy density functional:

$$E_{KS}[n] = T_s[n] + \int d\mathbf{r} V_{ext}(\mathbf{r}) n(\mathbf{r}) + E_{\text{Hartree}}[n] + E_{II} + E_{xc}[n] \tag{18}$$

where $T_s[n]$ is the independent particle kinetic energy, V_{ext} is the external potential due to the nuclei and any other applied field, E_{Hartree} is the classical Coulomb interaction of the electron density, and E_{II} is the interaction between the nuclei. All other many-body interactions from the exchange and the correlation of the electron densities are embedded into the E_{xc} term.

Applying the variational principle to E_{KS} to solve for the ground state energy of the system:

$$\frac{\delta E_{KS}}{\delta \psi_i^{\sigma *}(\mathbf{r})} = \frac{\delta T_s}{\delta \psi_i^{\sigma *}(\mathbf{r})} + \left[\frac{\delta E_{ext}}{\delta n(\mathbf{r},\sigma)} + \frac{\delta E_{Hartree}}{\delta n(\mathbf{r},\sigma)} + \frac{\delta E_{xc}}{\delta n(\mathbf{r},\sigma)} \right] \frac{\delta n(\mathbf{r},\sigma)}{\delta \psi_i^{\sigma *}(\mathbf{r})} = 0 \quad (19)$$

From the definitions of the independent electron kinetic energy;

$$\frac{\delta T_s}{\delta \psi_i^{\sigma *}(\mathbf{r})} = -\frac{1}{2}\nabla^2 \psi_i^{\sigma}(\mathbf{r}) \quad (20)$$

and the electronic density follows,

$$\frac{\delta n}{\delta \psi_i^{\sigma *}(\mathbf{r})} = \psi_i^{\sigma}(\mathbf{r}) \quad (21)$$

Using the method of Lagrange multipliers, $\delta[\langle\psi|\,\hat{H}\,|\psi\rangle - E(\langle\psi|\psi\rangle - 1)] = 0$ eq. 19 leads to the afore mentioned Shrödinger-like Kohn-Sham equations:

$$(H_{KS}^{\sigma} - \varepsilon_i^{\sigma})\psi_i^{\sigma}(\mathbf{r}) = 0 \quad (22)$$

and Kohn-Sham effective Hamiltonian becomes:

$$H_{KS}^{\sigma}(\mathbf{r}) = -\frac{1}{2}\nabla^2 + \underbrace{V_{ext}(\mathbf{r}) + \frac{\delta E_{Hartree}}{\delta n(\mathbf{r},\sigma)} + \frac{\delta E_{xc}}{\delta n(\mathbf{r},\sigma)}}_{V_{KS}^{\sigma} = V_{ext}(\mathbf{r}) + V_{Hartree}(\mathbf{r}) + V_{xc}(\mathbf{r})} \quad (23)$$

Up to this point, the Kohn-Sham density functional theory is an exact theory. In principle, it is possible to solve the interacting many-body problem using these independent particle equations, if one knows all the energy density functionals of the Hamiltonian in eq. 23. Therefore, DFT is an *ab initio* theory.

The difficulty lies in obtaining the energy functional for the many-body interactions, involving the exchange terms and the correlations both from the kinetic and potential energies. All of these many-body terms are included in the exchange and correlation functional:

$$E_{xc}[n] = \langle \hat{T} \rangle - T_s[n] + \langle V_{int} \rangle - E_{Hartree}[n] \quad (24)$$

If $E_{xc}[n]$ term were known exactly, then the exact ground state energy of the system would immediately also be determined. However, the exact form of $E_{xc}[n]$ is not known exactly, and the development of these functionals to obtain a universally working DFT is still a field in progress by itself.

2.4.4 Exchange and Correlation Functionals

Although the exchange and correlation functional is not known explicitly, there exist local, semi-local and non-local approximations. E_{xc} is expressed in terms of the energy density ϵ_{xc}, which itself is a functional of electron density,

$$E_{xc}[n] = \int d\mathbf{r} n(\mathbf{r}) \epsilon_{xc}([n], \mathbf{r}) \tag{25}$$

and approximations are applied to this energy density term.

i) Local density approximation (LDA):

The local density approximation is the simplest approximation one can make to the energy density. In LDA, ϵ_{xc} is assumed to be identical to the homogeneous electron gas energy density:

$$E_{xc}^{LDA}[n] = \int d^3 r n(\mathbf{r}) \epsilon_{xc}^{hom.}[n(\mathbf{r})] \tag{26}$$

Ceperley and Alder determined the form of this energy density functional to a great accuracy [59]. This approximation works best for solids that resemble a homogeneous electron gas, with a smoothly varying electronic density. As a result, it fails for molecular systems, where the electron density goes to zero, with a continuous density form outside the molecular radius. Therefore, LDA functional will not be used in this thesis.

ii) Generalized gradient approximation (GGA):

To accommodate variations in the electronic density, a Taylor-like expansion is applied to include not only the electronic density itself, $n(\mathbf{r})$, but also the gradient of the density, $\nabla n(\mathbf{r})$ in the exchange and correlation energy density functional:

$$E_{xc}^{GGA}[n] = \int d^3 r n(\mathbf{r}) \epsilon_{xc}^{GGA}[n(\mathbf{r}), \nabla n(\mathbf{r})] \tag{27}$$

Therefore, GGA functionals work better for inhomogeneous systems. This form is generalized such that

$$E_{xc}^{GGA}[n] = \int d^3 r n(\mathbf{r}) \epsilon_{x}^{hom}[n(\mathbf{r})] F_{xc}[n(\mathbf{r}), \nabla n(\mathbf{r})] \tag{28}$$

where ϵ_x^{hom} is the exchange energy density functional of the unpolarised electron gas and F_{xc} is a dimensionless term that satisfies physically motivated

constraints on the exchange and correlation hole. This is one of the approaches to the development of different GGA functionals. Another method is developing a functional with parameters fitted to a database. One must be cautious when using these fitted functionals; while they would provide good results for the systems in the fitted database, they may not work as well for other systems, as these functionals are not universal.

At the beginning of Chapter 3, several different GGA functionals will be tested for proton ordered hexagonal ice XI. In the rest of chapters, PBE functional developed by Perdew-Burke-Ernzerhof, will be used [7] as the standard GGA functional. The exchange enhancement factor F_{xc} of PBE is not fitted to any database. Instead it is developed to satisfy physical constraints acting on the exchange and correlation hole, and in this case the main concern of this functional is to satisfy Lieb-Oxford bound. In this thesis, PBE functional will be used to compare the performance of a semi-local GGA approximation to functionals that include non-local van der Waals correlations.

iii) Non-local correlations with van der Waals density functionals (vdW-DF):

Non-local effects are completely missing from GGA functionals. However, quantum fluctuations could induce a dipole moment even in an inert gas, which in turn would induce dipole moments in its neighbours. Therefore, dipole-dipole, dipole-induced dipole, and induced dipole-induced dipole, etc. effects lead to long range correlations. The lowering of the energy due to these correlations are represented by van der Waals interactions. Recently, several energy density functionals that incorporate van der Waals interactions as a non-local functional have been developed. In this thesis, we will follow the development by Dion *et. al* in Ref. [8]:

$$E_{xc}^{vdW} = E_x^{GGA} + L_c^{LDA} + E_c^{nl} \tag{29}$$

where the van der Waals functional uses the exchange part of a GGA functional, which is close to the HF term to avoid overbinding attraction from the exchange term. It uses the local correlations from the LDA functional, and adds non-local correlations $E_c^{nl}[n]$ in the form of a functional:

$$E_c^{nl}[n] = \frac{1}{2}\int d^3r d^3r' n(\mathbf{r})\phi(q, q', |\mathbf{r} - \mathbf{r}'|)n(\mathbf{r}') \tag{30}$$

where the parameters q and q' are themselves functionals of n and its gradient, $q[n(\mathbf{r}), \nabla n(\mathbf{r})]$, evaluated at $\mathbf{r}$ and $\mathbf{r}'$. The constraint on $E_c^{nl}[n]$ follows

such that it must have a r^{-6} dependence of potential at long range separations, which is the signature of van der Waals potential. The non-local correlations also goes to zero for systems with constant electronic density. The advantage of this functional is that it only depends on $|\mathbf{r} - \mathbf{r}'|$, instead of depending on r and r' separately. However, double integrals over the all space is computationally quite expensive, and the application of these van der Waals functionals had to wait another five years for the development of non-local kernel factorisation by Román-Pérez and Soler [60].

In the original vdW-DF functional, revPBE functional [10] has been used for the GGA exchange term [8]. This original functional is tested on ice XI in Chapter 3. We have also changed the exchange flavour of this functional from revPBE to PBE, labelled as vdW-DF$^{\mathrm{PBE}}$ functional. This functional has been shown to perform better for liquid water and hexagonal ice [6, 9, 61]. Therefore, in the main part of this thesis the vdW-DF$^{\mathrm{PBE}}$ functional is compared to the semi-local PBE functional.

2.4.5 Self Consistent Loop to Solve Kohn-Sham Equations

Kohn-Sham equations are solved self consistently. First, an initial guess of the density is used to obtain the external potential, as follows from HK theorems. At this point, either orthogonal single electron plane waves, or localised atomic orbitals can be used to generate the densities. These are two separate approaches to DFT, and the SIESTA package [62, 63] that is employed in this thesis is based on the latter approach.

Then, KS equations are solved using this external potential. The new electronic density is deduced from the ground state, and compared to the initial guess. This new density is used as an input to solve the KS equations again, until the output density is consistent with the input density within a small tolerance, which is determined by the user and depends on the system.

From the output electronic density, the ground state electronic energy and also the forces on the atoms of the system will be calculated for futher analysis of the structures used in this dissertation.

2.4.6 Hellmann-Feynman Theorem and Structural Relaxation

Once the ground state energy is obtained with the self consistent field, as explained above, then the forces on the system can also be calculated. The force conjugate to the position of a nucleus in the system can be written in

terms of the energy as:

$$\mathbf{F}_I = -\frac{\partial E}{\partial \mathbf{R}_I} = -\langle\psi|\,\frac{\partial \hat{H}}{\partial \mathbf{R}_I}\,|\psi\rangle - \langle\frac{\partial \psi}{\partial \mathbf{R}_I}|\,\hat{H}\,|\psi\rangle - \langle\psi|\,\hat{H}\,|\frac{\partial \psi}{\partial \mathbf{R}_I}\rangle - \frac{\partial E_{II}}{\partial \mathbf{R}_I} \quad (31)$$

The ground state electronic density corresponds to the total energy minimum, therefore all the electron-electron interaction contributions lead to a cancellation of the middle terms. The only contribution comes from the explicit dependence on the ionic positions, which are from the external potential and ion-ion interaction terms. Then the forces become:

$$\mathbf{F}_I = -\int d^3r n(\mathbf{r})\frac{\partial V_{ext}(\mathbf{r})}{\partial \mathbf{R}_I} - \frac{\partial E_{II}}{\partial \mathbf{R}_I} \quad (32)$$

Once the forces on the atoms are obtained for that particular ionic positions, then a conjugate gradient approach of variational principle can be used to minimise these forces. In this way, the atomic positions are varied to minimise the total electronic energy by minimising the forces along the energy gradient. The structure is considered to be relaxed, when the atomic forces are smaller than a force tolerance criteria.

2.5 Force Field Models for Water

Although *ab initio* calculations are quantum mechanical calculations with high accuracy, they are computationally quite expensive. Therefore, it is only possible to simulate systems with small number of atoms, and the simulation times are limited. In order to overcome this problem, force field models for the system of interest are developed. A potential model for the interaction force fields of molecules is parametrised. These parameters are either fitted to reproduce experiments or a set of *ab initio* calculations to obtain the empirical or semi-empirical force field models. Then the model Hamiltonian can be solved using the variational principle, for example. The advantage of having these force field models is that they allow for longer simulation times for larger set of atoms. In this thesis, two of these force field models, one fitted to the experiments and one fitted to high level *ab initio* calculations, will be utilised to compare to DFT results. Both of these models put emphasis on an accurate description of the vibrational spectra of liquid water, which is the first important step for the analysis followed in this thesis. The comparisons of these force field models with DFT yield the limitations of both of these models and gives insight into the future improvements of models for water.

2.5.1 qTIP4P/F: quantum Transferable Intermolecular 4-Point Potential / Flexible

The qTIP4P/F force field model [11] is based on an earlier version of the TIP4P/2005 flexible force field model. This is a 4-site model, where three of the sites are the locations of the hydrogen and oxygen nuclei, but the charges are not necessarily located on the same site as the nuclei. The fourth site comes from the location of the negative partial charge, $-q_M$, called M-site: $\mathbf{r}_M = \gamma \mathbf{r}_O + (1+\gamma)(\mathbf{r}_{H_1} + \mathbf{r}_{H_2})/2$, which is fraction of γ along the oxygen atom and the center of mass of hydrogens. The two positive partial charges, $q_M/2$ are located on the hydrogen sites. Intermolecular forces are based on the electrostatic interactions and a Lennard-Jones type potential between the oxygen atoms, following the authors' notation:

$$V_{inter} = \sum_i \sum_{j>i} \left\{ 4\varepsilon \left[\left(\frac{\sigma}{r_{ij}} \right)^{12} - \left(\frac{\sigma}{r_{ij}} \right)^{6} \right] + \sum_{m \in i} \sum_{n \in j} \frac{q_m q_n}{r_{mn}} \right\} \tag{33}$$

where i, j goes through the oxygen sites and m, n goes through the partial charge sites. The flexibility of the molecule is obtained via a Morse potential, where OH stretching modes are accommodated via a harmonic oscillator:

$$V_{intra} = \sum_i \left[V_{OH}(r_{i1} + V_{OH}(r_{i2} + \frac{1}{2} k_\theta (\theta_i - \theta_{eq})^2 \right], \tag{34}$$

$$V_{OH}(r) = D_r \left[\alpha_r^2 (r - r_{eq})^2 - \alpha_r^3 (r - r_e q)^3 + \frac{7}{12} \alpha_r^4 (r - r_{eq})^4 \right]$$

where r_i are the intra-molecular OH covalent bonds and θ_i are the H-O-H bond angle of each molecule.

The inter-molecular parameters of the Lennard-Jones potential are ε, σ, q_M, and γ and are the same as the original flexible TIP4P/2005 model, which was parametrised to fit the temperature of maximum density, and stability of several ice polymorphs [22].

The intra-molecular parameters D_r, α_r, r_{eq}, k_θ, and θ_{eq}, were optimised to reproduce the experimental structure, self diffusion constant, and vibrational absorption spectra of the liquid water. The optimisation of these parameters was obtained by using path integral molecular dynamics simulations, which can incorporate nuclear quantum mechanical contributions [11]. Furthermore, intra-molecular OH stretching modes of this model are

anharmonic, and it reproduces the anti-correlation effects between the intra- and inter-molecular bonds. Therefore, this is a good model to test to establish whether or not it can reproduce the anomalous isotope effect due to the nuclear quantum effects.

2.5.2 TTM3-F: Thole-type Model version 3.0 - Flexible

The TTM3-F semi-empirical force field model [12] is a 4-site model, as well. This is also a flexible model, where molecular angles and bond lengths are allowed to change throughout the simulations. In addition, each molecule is assigned a monomer dipole moment as will be explained briefly.

The oxygen site is charge neutral, the hydrogen site has a static positive charge, and the negative charge is located on the massless M-site, in this case defined as, again following the authors' notation: $\mathbf{r}_M = \mathbf{r}_O + (\gamma/2)(\mathbf{r}_{OH_1} + \mathbf{r}_{OH_2})$. The charges, q_i, and the dipole moment, $\mathbf{p} = \sum_i q_i \mathbf{r_i}$, are assigned by fitting to *ab initio* calculations of the monomer potential energy surface and dipole moment surfaces (DMS). However, a transformation is applied to the charges obtained from the gas phase DMS to get the liquid phase DMS, which should incorporate the increase in the charge on hydrogen atoms with increasing OH separation.

$$\begin{aligned} q_{H_i} &= \left(q_{H_i}^{DMS} + d_r(r_{OH_i} - r_e) + d_\theta(\theta - \theta_e)\right) \\ &- \frac{\gamma}{2(1-\gamma)}\left[\sum_i - \left(q_{H_i}^{DMS} + d_r(r_{OH_i} - r_e) + d_\theta(\theta - \theta_e)\right)\right] \\ q_M &= \sum_i -q_{H_i} \end{aligned} \tag{35}$$

where $q_{H_i}^{DMS}$ are obtained from the *ab initio* calculations, with a fitting parameter γ adjusted for accurate dipole and quadrupole moments. The point charges are smeared with an effective charge density, following Thole's method:

$$n(r) = \frac{1}{(a_i a_j)^{1/2}} \frac{3a_s}{4\pi} \exp\left(-a_s \left(\frac{r}{(a_i a_j)^{1/6}}\right)^3\right) \tag{36}$$

where a_s is the smearing of the charge density, a_i are the atomic polarisabilities for H-site, a_H, and M-site, a_M. In this way, the flexibility and the polarisability are incorporated into the model: the charges are redistributed for the polarisability, as the geometry changes with the flexibility of the model.

Finally, the inter-molecular interactions are taken into account through a van der Waals type potential:

$$V(r) = \frac{\varepsilon}{1 - 6/\lambda} \left\{ \frac{6}{\lambda} \exp\left(\lambda \left[1 - \frac{r}{\sigma}\right]\right) \left(\frac{\sigma}{r}\right)^6 \right\} \tag{37}$$

All the parameters of this model are found by fitting to high level *ab initio* calculations of water clusters, $(H_2O)_n$, with $n = 3 - 6, 20$. This model produced good structural properties and energetics for water clusters and good structure and thermodynamic properties of liquid water. The parameters are adjusted especially to provide the vibrational spectra, with a focus on reproducing the intra-molecular OH stretching frequencies of both water clusters and liquid water [12] . Having a model with an accurate description of the vibrational spectra is the first step to analysing the nuclear quantum effects, therefore this model is also selected to compare to DFT results in this thesis.

2.6 Phonon Calculations

For an accurate description of the nuclear quantum effects of an ice structure, which is the main goal of this thesis, obtaining an accurate electronic structure energy is only the first step. Next, we need energy contributions from the nuclei-nuclei interactions. For this purpose, the phonon energies due to the quantum fluctuations of the ions are calculated to be added to the electronic energy.

In solids, the phonon energies are modelled as ions connected with oscillators, and the corresponding potential energy is obtained by considering the displacements from the equilibrium positions, $u(R)$:

$$V_{II} = \frac{1}{2} \sum_{R,R',\alpha,\alpha'} u_\alpha(R) \underbrace{\frac{\partial^2 V}{\partial u_\alpha(R) u_{\alpha'}(R')}}_{D_{\alpha\alpha'}(R-R')} u_{\alpha'}(R') \tag{38}$$

where, $\alpha = x, y, z$. Then the corresponding equations of motions become:

$$M\ddot{u}_\alpha(R) = -\frac{\partial V}{\partial u_\alpha(R)} = -\sum_{R'\alpha'} D_{\alpha\alpha'}(R - R') u_{\alpha'}(R') \tag{39}$$

with solutions of the form of plane waves: $\mathbf{u}(\mathbf{R}, t) = \boldsymbol{\epsilon} e^{i(\mathbf{k}\cdot\mathbf{R} - \omega t)}$, the eigenvalue problem becomes,

$$M\omega^2 \boldsymbol{\epsilon} = D(\mathbf{k})\boldsymbol{\epsilon} \tag{40}$$

where $\boldsymbol{\epsilon}$ is defined as the polarisation vector and $D(\mathbf{k}) = \sum_R D(\mathbf{R}) e^{-i\mathbf{k}\cdot\mathbf{R}}$ is the dynamical matrix.

In the frozen phonon approximation, the atoms of the system are displaced in the 6 different directions, and the forces on each atom are calculated, as explained in eq. 31. By taking the differences of the forces on the atoms of the relaxed configuration, the dynamical matrix is obtained. Diagonalising the dynamical matrix, immediately yields the eigenvalues $\omega = \sqrt{D(k)/M}$, which correspond to the phonon frequencies of the system.

2.7 Quasi-harmonic Approximation

2.7.1 Helmholtz Free Energy

To include the nuclear quantum effects, the Helmholtz free energy $F(V,T)$ [64] is calculated as a function of volume and temperature within the volume-dependent quasiharmonic approximation (QHA). [6, 65] One can neglect thermal contributions to the electronic free energy because of the large band gap of ice.

To derive Helmholtz free energy, we start with the partition function of on particle in a potential of a harmonic oscillator, for simplicity, with equations of state $\varepsilon_k = \frac{\hbar\omega}{2} + n\hbar\omega$:

$$\begin{aligned} Z &\equiv \sum_n e^{-\varepsilon_n/k_BT} = \sum_n e^{-(\frac{\hbar\omega}{2}+n\hbar\omega)/k_BT} \\ &= e^{-\hbar\omega/2k_BT} \sum_n e^{-n\hbar\omega/2k_BT} \\ &= e^{-\hbar\omega/2k_BT} \frac{1}{1-e^{-\hbar\omega/k_BT}} \end{aligned} \tag{41}$$

where k_B is the Boltzmann constant. In the last step of this derivation, the geometric sum: $\sum_n ar^{ns} = \frac{a}{1-r^s}$ has been used. The single particle partition function can be expanded to a system of solids, by obtaining the frequencies of all particles, at all positions. This can simply be stated by changing ω to ω_k, where k stands for both phonon branches, and phonon wave vectors within the Brillouin zone. Then, the definition of the vibrational free energy

from the partition partition follows:

$$\begin{aligned} F_v &\equiv -k_B T \ln Z = -k_B T \sum_k \left(\ln e^{\hbar\omega_k/2k_BT} - \ln(1 - e^{-\hbar\omega_k/k_BT}) \right) \quad (42) \\ &= -k_B T \sum_k \left(\frac{-\hbar\omega_k}{2k_BT} - \ln(1 - e^{-\hbar\omega_k/k_BT}) \right) \\ &= \sum_k \left[\frac{\hbar\omega_k}{2} - k_B T \ln\left(1 - e^{-\hbar\omega_k/k_BT}\right) \right] \end{aligned}$$

Finally, by including the entropy from the possible disorder in the hydrogen positions to the vibrational free energy, we get the total Helmholtz free energy: $F = E_0 + F_v - TS_H$ as in eq. 43.

$$\begin{aligned} F(V,T) &= E_0(V) + \\ &\quad \sum_k \left[\frac{\hbar\omega_k(V)}{2} + k_B T \ln\left(1 - e^{-\hbar\omega_k(V)/k_BT}\right) \right] \\ &\quad -TS_H \end{aligned} \quad (43)$$

where $E_0(V)$ is the energy for classical (T = 0K or frozen) nuclei, at the relaxed atomic coordinates for each volume. The equilibrium volume and bulk modulus are calculated from the minimum and the curvature at each T. The phonon frequencies, ω_k are calculated with k running over both phonon branches and phonon wave vectors within the Brillouin zone. The last part of the Free energy is related to the entropy due to the proton disorder, S_H. This term is zero for proton ordered phase, ice XI. For proton disordered phase, ice Ih, we use the estimation by Pauling, $S_H = Nk_B \ln(3/2)$, which was obtained by counting hydrogen orientations that obey the ice rules, [51] and experimentally confirmed for fully disordered cases, [66, 67]. We assume that S_H does not change with temperature.

Lastly, the classical limit of the free energy is obtained by taking the classical limit of QHA given in eq. 44.

$$\begin{aligned} F(V,T) &= E_0(V) + \\ &\quad \sum_k \left[k_B T \ln\left(\frac{\hbar\omega_k(V)}{k_BT} \right) \right] - TS_H \end{aligned} \quad (44)$$

2.7.2 Implementation of QHA

QHA takes into account the anharmonicities in the phonon modes due to the change in the volume. Therefore, the direct implementation is done by obtaining the phonon frequencies of the system at each volume to calculate the free energy in eq. 43. This can easily be done with the semi-empirical force field models, but an accurate calculation of the phonon modes with *ab initio* DFT can be computationally expensive. Therefore, in our DFT calculations, the number of phonon calculations is reduced by an indirect implementation of QHA.

The employment of QHA is done starting with the definition of Grüneisen parameters given in eq.(45)

$$\gamma_k = -\frac{\partial(\ln\omega_k)}{\partial(\ln V)} = -\frac{V}{\omega_k}\frac{\partial\omega_k}{\partial V} \tag{45}$$

Rearranging this definition and integrating both sides, we get:

$$\int_{\omega(V_0)}^{\omega_k} \frac{\partial\omega_k}{\omega_k} = -\int_{V_0}^{V} \gamma_k \frac{\partial V}{V} \tag{46}$$

We take the reference point, V_0, as the equilibrium volume of the classical energy $E_0(V)$ in our calculations.

$$\ln\left(\frac{\omega_k}{\omega(V_0)}\right) = -\gamma_k \ln\left(\frac{V}{V_0}\right) \tag{47}$$

This is the first approximation to the QHA, labelled QH1:

$$\omega_k(V) = \omega(V_0)\left(\frac{V}{V_0}\right)^{-\gamma_k} \tag{48}$$

If the Taylor expansion of the logarithm in eq. 47 is taken, then it gives the second approximation to the QHA, labelled QH2 which we used in our calculations for this thesis:

$$\omega_k(V) = \omega(V_0)\left(1 - \gamma_k\frac{V - V_0}{V_0}\right) \tag{49}$$

where γ_k is the Grüneisen parameter of the mode, as shown in eq. 45. Now, instead of calculating $\omega_k(V)$ at every volume, γ_k is obtained from a linear fit

to three (or five depending on the system size) frequencies selected around the classical equilibrium volume, V_0. Then eq. 49 is used to obtain the full volume dependency of the frequencies $\omega_k(V)$ to calculate the total free energy in eq. 43. Hence, the volume dependence of $\omega_k(V)$ is linearised with the QHA at each T, through the Grüneisen parameter calculations.

As shown in recent contributions [6, 65], the QH2 in 49 is an excellent approximation to the full QHA for hexagonal ice. A comparison of these approximations for one of our systems will be presented in Chapter 3 to validate the usage of QH2 in our systems, and we will refer to QH2 as QHA unless otherwise mentioned. Furthermore, Ref. [65] compares QHA with PIMD simulations, and shows that QHA results agrees well with the PIMD calculation for obtaining the quantum volume and bulk modulus of ices.

2.7.3 Volume Change at T = 0 K

The quasi-harmonic volume shift is:

$$\frac{V - V_0}{V_0} = \frac{1}{V_0 B_0} \sum_k \gamma_k \hbar \omega_k \left(n_k + \frac{1}{2} \right) \tag{50}$$

where V_0 is the frozen or classical volume, V is the quantum volume and B_0 is the bulk modulus of the system.

At $T = 0$, $n_k = 0$ and it can be seen that $\Delta V = V - V_0$ is proportional to the average $\langle \gamma_k \omega_k \rangle$.

2.7.4 Cohesive Energy

To determine which structure is the most stable one at zero temperature, cohesive energies of ices are calculated without (E_c^0) and with (E_c) zero point effects. The cohesive energy is defined as the difference between the energy of a molecule within the crystal and the energy of a monomer. The classical cohesive energy, E_c^0 is defined as eq. 51 from the Kohn-Sham energies of the ice and monomer, and similarly, the quantum cohesive energy with zero point effects, E_c is defined as eq. 52.

$$E_c^0 = \frac{E_0^{\text{ice}}}{N_{\text{molecules}}} - E_0^{\text{monomer}} \tag{51}$$

$$E_c = \frac{F^{\text{ice}}(V_0, 0)}{N_{\text{molecules}}} - E_0^{\text{monomer}} - E_{ph}^{\text{monomer}} \tag{52}$$

where the vibrational phonon energy $\sum_k \hbar\omega_k/2$ of the branches calculated for the monomer is E_{ph}^{monomer}.

2.7.5 Bulk Modulus and Pressure

In addition to calculating the energies of the two phases to predict the phase transition, we also make a detailed analysis of bulk modulus of hexagonal ices. For bulk modulus calculations, we change the lattice parameters by 0.15% and obtain the energy of the relaxed configuration within each fixed volume. Then, we make a new fit to the curve of energy as a function of volume, E(V). The curvature of this fit is used to calculate the bulk modulus as in eq. 53.

$$B = V_0 \left.\frac{\partial^2 E}{\partial V^2}\right|_{V=V_0} \tag{53}$$

where energy E(V) is the Kohn-Sham energy, E_0(V), for classical calculations, and the Helmholtz Free energy, F(V), for the calculations including the nuclear quantum effects. V_0 is the equilibrium volume of the corresponding energy.

Similarly, for systems that are stable under pressure, the volume that corresponds to the experimental pressure is obtained from the slope of the energy:

$$P = -\frac{\partial E}{\partial V} \tag{54}$$

Other thermodynamic relations can also be derived from the partition function, by using eq. 43.

2.8 Conclusion

In this chapter, we have briefly explained the foundations of *ab initio* DFT, and the density functional approximations are described. Furthermore, two semi-empirical force field models, qTIP4P/F and TTM3-F, which will be used to compare to DFT results are introduced. Next, the phonon calculations are described to explain the Helmholtz free energy. Most importantly, Grüneisen parameters are defined to develop the methodology for obtaining the Helmholtz free energy within the quasi-harmonic approximation. In this way, a concise explanation of the theory that is utilised in the rest of this thesis is provided.

3 Nuclear Quantum Effects on the Volume of Hexagonal Ices

Hexagonal ice is the phase of ice that is formed when liquid water freezes under ambient conditions. This was also the first of the identified ice phases, therefore it is called ice I. Moreover, it forms with an underlying hexagonal lattice of oxygen atoms, so it is labelled ice Ih. While the oxygen atoms have a hexagonal order, protons of the water molecules of ice Ih are disordered. As the temperature decreases, ice Ih goes under a phase transition to form ice XI and its hydrogen atoms become ordered. Details of the structures of these two hexagonal ice phases will be explained in Chapters 3, 4 and 5.

In this chapter, the structural lattice parameters and volumes of the two phases of hexagonal ice are compared. As explained in the introduction, the nuclear quantum effects become important at low temperatures, and lattice parameters of different isotopes can be distinguished. Therefore, how zero-point vibrations of the lattice affect these structures is investigated through an analysis of the isotope effect in volume. Under normal isotope effect, the volume of a heavy isotope is smaller than that of a light isotope, as in the example of Ne, which has similar atomic mass than water [39]. However, in hexagonal ice Ih, it is experimentally known that this effect is reversed. Heavy ice (D_2O) has larger lattice parameters and volume than regular ice (H_2O) [3, 40], resulting in an anomalous isotope effect. The underlying mechanism behind this anomaly has not been understood before. Moreover, there has not been an investigation of the isotope effect in the oxygen atoms. We provide an explanation of the anomalous isotope effect in hexagonal ices, by calculating the phonon modes and the corresponding Grüneisen parameters. The different signs of the Grüneisen parameter of different modes, corresponding to different bonds, reveals a clear anti-correlation between intra- and inter-molecular bonds.

The details of this anti-correlation will be discussed in the rest of this chapter.

3.1 Structures

3.1.1 Proton Disordered Hexagonal Ice - Ice Ih

The stable phase of ice under ambient conditions is the hexagonal ice, ice Ih. In this phase, the oxygen atoms form an underlying lattice of a wurtzite structure. The wurtzite structure is defined by two lattice parameters: lattice parameter a along the x-y plane, and lattice parameter c along the z-axis. The hydrogen atoms of hexagonal ice can occupy only certain orientations, which satisfy the hydrogen bonding requirements. The hydrogen bonding requirement is defined by the Bernal-Fowler ice rules, where each oxygen is tetrahedrally coordinated to hydrogen atoms, making two covalent bonds and two hydrogen bonds [50]. The hexagonal ice Ih is characterised by the disorder in the occupation of these possible proton orientations that can satisfy the "ice rules".

To take into account the proton disorder in the structure, we have performed our calculations with 96 water molecules, with cell size of $3a \times 2\sqrt{3}a \times 2c$. The protons are oriented such that there is no net dipole moment in the bulk. This structure is shown in Fig. 2.

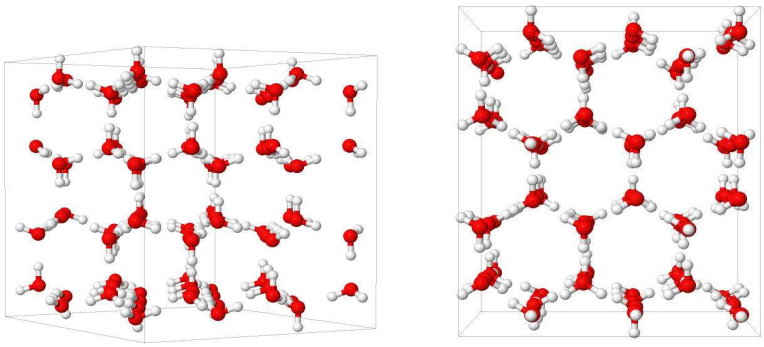

Figure 2: H-disordered ice Ih structure. The image on the left is the top view of the x-y plane; the image on the right is the side view of the x-z plane.

3.1.2 Proton Ordered Hexagonal Ice - Ice XI

As the temperature is lowered from the ambient conditions, the proton mobility of ice decreases, and the transition to the proton ordered phase is frustrated. However, the proton mobility can be enhanced in the presence

of impurities of KOH^- [52, 53, 68] and a phase transition from the proton disordered hexagonal ice Ih phase to the proton ordered hexagonal ice XI phase is observed at around 72 K for H_2O and 76 K for D_2O [52, 53]. Ice XI has 4 molecules in the unitcell with a net dipole moment along the $\hat{c}$ axis. The structure of this phase is shown in Fig. 3.

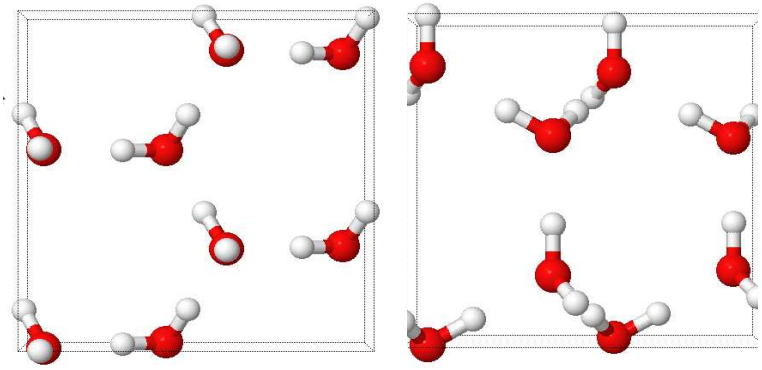

Figure 3: Proton ordered ice XI structure. The image on the left is the top view of the x-y plane; the image on the right is the side view of the x-z plane.

3.1.3 Proton Ordered Hexagonal Ice - Bernal-Fowler Ice

The four protons of ice XI do not follow the hexagonal symmetry of underlying oxygen atoms. Considering the symmetries of the lattice, we have also generated a proton ordered hexagonal lattice where both oxygens and hydrogens follow hexagonal symmetry, which is called Bernal-Fowler ice (BF ice). BF ice has 12 molecules in the unit cell with a net dipole moment along the $\hat{c}$ axis, as shown in Fig. 4.

3.2 Computational Details

Before going into the discussion of the results and the underlying physical mechanisms, one must explain all the details of the computational parameters such that the results are reproducible by everyone. This section goes through these details of parameters that were employed in the SIESTA DFT package.

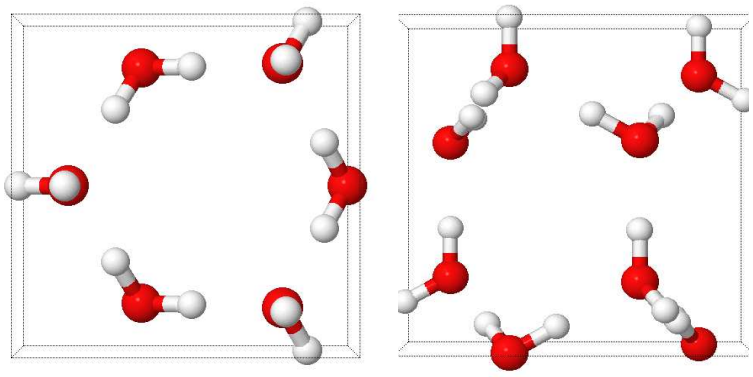

Figure 4: Proton ordered BF ice structure. The image on the right is the top view of the x-y plane; the image on the left is the side view of the x-z plane.

3.2.1 Calculation Details and Parameters

All structural relaxations are performed using a real-space mesh cutoff of 500 Ry for the real space integrals, an electronic k-grid cutoff of 10 Å (corresponding to 38 k-points) for unit cell calculations, a force tolerance of 0.001 eV/Å and a density matrix tolerance of 10^{-5} electrons.

The force constant calculations of proton ordered ice XI structure are performed with a finer real-space mesh cutoff of 800 Ry. We used an atomic displacement Δx=0.06 Å for the frozen phonon calculation.

The force constant calculations of proton disordered ice Ih are performed with a mesh cutoff of 500 Ry. We used an atomic displacement Δx=0.08 Å for the frozen phonon calculation.

The phonon frequencies, $\omega_k(V_0)$ and Grüneisen parameters $\gamma_k(V_0)$ are obtained by diagonalizing the dynamical matrix, computed by finite differences from the atomic forces in a $(3 \times 3 \times 3)$ supercell, at volumes slightly below and above V_0. We tested these parameters to obtain force constants in phonon calculations as accurate as possible, so that the Grüneisen parameter calculations have minimum noise. The Grüneisen parameters are calculated for 5 volumes around the minimum varied with an isotropic change in the lattice parameters for Γ point calculations of ice XI. In order to cover the full Brillouin zone of H-ordered ice XI, 729 k-points are selected, dividing each reciprocal lattice vector into 9 equal sections. Therefore, the Grüneisen parameters are calculated for 3 volumes for a k-point sampling of ice XI and at

the Γ point of H-disordered ice Ih due to increase in the system size. Results of our error estimation will be presented below.

3.2.2 Atomic Basis Sets

We used a basis set of triple-ζ polarized (tζ+p) atomic orbitals in the first set of all calculations. The SIESTA basis set input file, with information about the cutoff radii of the orbitals is given in Appendix A. We present the same information for double-ζ polarized (dζ+p) atomic orbital basis set that has been used in previous studies [9]. In order to compare the performance of this basis set, we calculated the lattice parameters of the proton ordered (H-ordered) ice XI structure at the Γ point with the PBE functional. The first two lines of Table 2 show that a triple-ζ polarized orbital basis improves the results as compared to plane wave calculations [69].

3.2.3 Validation of QHA and Error Analysis

To test the validity of the QHA in ice Ih, Fig. 5 compares the QHA result for $V(T)$ with fully anharmonic PIMD simulations [2], using the q-TIP4P/F force field [11] in both cases. Differences between the QHA and PIMD increase with temperature, but their overall agreement is satisfactory.

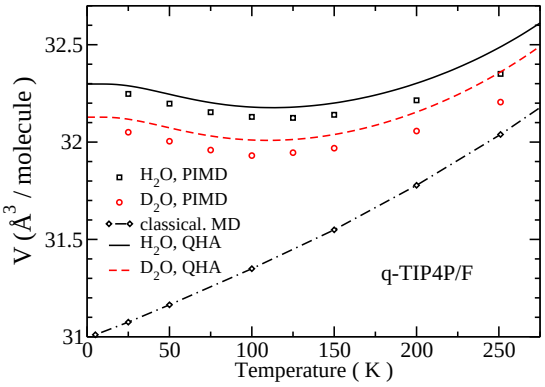

Figure 5: Volume per molecule for different isotopes calculated using the q-TIP4P/F force field both with PIMD [2] simulations and the QHA.

In particular, with this force field both calculations predict a normal isotope effect [2], which includes a lattice contraction when H is replaced by D and a convergence of H and D volumes with increasing T, contrary

to the experimental result. To complement these results, we have repeated the calculations using the polarizable TTM3-F[12, 70] potential. This force field has recently been shown to outperform q-TIP4P/F when compared to experiments in PIMD simulations of $H_2{}^{18}O$ and $D_2{}^{18}O$. Results provided in Table 3 show that this polarizable force field also fails to reproduce the anomalous isotope effect. However, as it will be discussed, TTM3-F improves over q-TIP4P/F, displaying a stronger anti-correlation effect.

In addition, QH1, and QH2 levels of approximation are compared to the full QHA, labeled QH0. As seen in Fig 6, QH2 performs better than QH1. Indeed it is an excellent approximation to the full QHA, in which the frequencies are calculated at each volume. Using DFT instead of the empirical potential the differences between QH1 and QH2 are much smaller, as seen in the error estimation below.

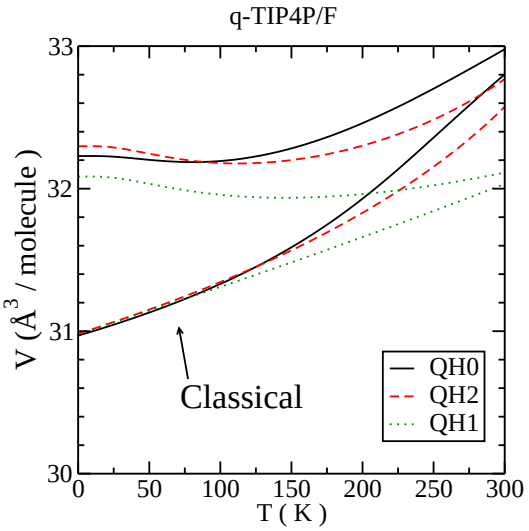

Figure 6: Volume per molecule for H_2O and for the classical limit calculated using q-TIP4P/F using different versions of the QHA. QH0 stands for the full QHA, and QH1 and QH2 are explained in the text.

We present here an analysis of the main numerical sources of error in our calculations, beyond any DFT approximation. These error estimation calculations are performed with tζ+p basis as descibed in Ref. [6]. We have identified three:

(i) Numerical evaluation of Grüneisen constants:

We choose 5 volumes slightly below and above V_0 to calculate ω_k and γ_k for the calculations where the phonons are obtained for Γ-sampling only. However, we choose 3 volumes when the QHA is computed using phonons obtained by sampling the full (4 molecules, hexagonal) Brillouin zone. To estimate the error involved in calculating Grüneisen constants from 3 or 5 volumes we compare the vdW-DF$^{\rm PBE}$ functional volume QHA results obtained using Γ-sampling phonons. As seen in Table 1, the volume decreases by ∼0.03% when 5 volumes are used instead of 3. The magnitude of the isotope shift is hardly affected.

Table 1: Isotope-dependent volume per molecule (Å^3) at $T = 0$ K for H-ordered ice XI structure with the vdW-DF$^{\rm PBE}$ functional at Γ point. *cla* represents the classical result. (i) shows the V(T=0) as function of the number of volumes chosen to calculate ω_k and γ_k, (ii) as function of the Δx atomic displacement used to compute the force constants, and (iii) as function of the two different QHA methods, QH1 to QH2.

(i) # of volumes	5	3
cla	30.88	30.88
H_2O	31.01	31.02
D_2O	31.10	31.11
$H_2{}^{18}O$	30.98	30.99
(ii) Δx for phonons	0.06 Å	0.08 Å
cla	30.88	30.88
H_2O	31.02	30.97
D_2O	31.11	31.07
$H_2{}^{18}O$	30.99	30.95
(iii) QHA method	QH1	QH2
cla	30.88	30.88
H_2O	31.00	31.01
D_2O	31.09	31.10
$H_2{}^{18}O$	30.97	30.98

(ii) Frozen phonon approximation:

The second possible source of error is the atomic displacement Δx used to compute the force constants by finite differences, within the frozen phonon approximation. We compare vdW-DF$^{\rm PBE}$ volumes at Γ with mesh cutoff of 800 Ry using 3 volumes to compute ω_k and γ_k. Phonons are calculated using two different displacements: $\Delta x = 0.06$ Å and $\Delta x = 0.08$ Å. Table 1 shows that this is the largest source of error. Volumes for the same isotope are

modified by $\sim 0.14\%$ when $\Delta x = 0.08$ Å changes to $\Delta x = 0.06$ Å. However, the volume isotope shift is almost unchanged.

(iii) Numerical quasiharmonic approximation:

The last source of error is due to the method of linearising the volume dependence of the frequencies in the quasiharmonic approximation. This has already been discussed above, using the q-TIP4P/F model, but we present results using DFT in this section. We compare results for the QH1 and QH2 linearisations using the vdW-DF$^{\mathrm{PBE}}$ functional (Γ-sampling for phonons). The real-space mesh cutoff is 800 Ry and the atomic displacement is Δx=0.06 Å for force constant calculations. We used 5 different volumes to obtain the frequencies and Grüneisen constants. As seen in Table. 1 QH1 predicts smaller volumes than QH2, with a difference of $\sim$0.03%. This is much smaller than the differences obtained using the q-TIP4P/F force field. As expected, both give the same sign and almost no change for the isotope effect. Overall, as seen above, QH2 gives better results when compared to the experiments.

3.3 Results

3.3.1 Initial results with different functionals

First, electronic structure calculations are performed for all three hexagonal ices. The structure is relaxed within a volume fixed by the lattice parameters to obtain the Kohn-Sham energy, and this calculation is repeated for a variety of lattice parameters to get the optimal lattice parameters, and the corresponding volume at the energy minimum.

The level of approximation within DFT depends on the choice of the functional. The initial calculations were performed with a variety of functionals and compared with the experiments. Some of the most common functionals in the *ab initio* calculations of water, within semi-local generalized gradient approximation (GGA) are the PBE and revPBE functionals [7, 10]. With the recent developments of incorporating non-local van der Waals forces into the exchange and correlation functional, we also performed calculations with vdW-DF (also referred in the literature as DRSLL) functional [8], which was implemented recently [60]. The exchange part of the original functional was replaced with PBE, to compare the importance of van der Waals interactions to this functional separately, and this combination is labelled as vdW-DF$^{\mathrm{PBE}}$. In addition, we extended our initial set of functionals to the WC, vdW-DF$^{\mathrm{WC}}$, BLYP, and a more recetly developed vdW-DF2 (also sometimes referred in

the literature as LMKLL) functionals. This initial test of functionals are performed with ice XI, which has 4 molecules in the unit cell, making it computationally affordable to perform such a series of calculations. The initial set of frozen lattice parameters, a and c, their ratio and the corresponding classical volume at the Kohn-Sham energy minimum are given in Table 2.

Table 2: A summary of results with different functionals. a and c lattice parameters, their ratio (c/a), corresponding volume per molecule of proton ordered and proton disordered ices, for several DFT functionals. Proton ordered ice XI with PBE functional is calculated for double-ζ polarized and triple-ζ polarized atomic orbital basis sets. All phonon calculations are at the Γ point. Structural experimental results are for $T = 10$ K. All lengths and volumes are in Å and Å^3.

Ice	XC	a	c	c/a	V0	H_2O	D_2O
XI	PBE (dζ+p)	4.44	7.25	1.633	30.94		
XI	PBE (tζ+p)	4.39	7.17	1.633	29.98	29.91	30.05
XI	revPBE	4.52	7.42	1.642	32.84	32.88	32.98
XI	WC	4.26	6.96	1.634	27.32	27.13	27.19
XI	BLYP	4.50	7.33	1.629	31.14	32.23	32.12
XI	vdW-DF$^{\mathrm{PBE}}$	4.44	7.23	1.628	30.88	31.01	31.10
XI	vdW-DF$^{\mathrm{revPBE}}$	4.56	7.43	1.629	33.45	33.73	33.76
XI	vdW-DF$^{\mathrm{WC}}$	4.32	7.03	1.627	28.35	28.10	28.19
XI	vdW-DF2	4.54	7.36	1.621	31.97	31.86	31.83
XI	PBE [69]	4.40	7.20	1.636	30.23		
XI	revPBE [69]	4.53	7.45	1.642	33.13		
BF	PBE	4.39	7.17	1.633	29.98		
BF	vdW-DF$^{\mathrm{PBE}}$	4.44	7.23	1.628	30.88		
Ih	PBE	4.39	7.17	1.633	29.91	29.93	30.04
Ih	vdW-DF$^{\mathrm{PBE}}$	4.44	7.24	1.630	30.90	31.16	31.23
Ih	Expt. [3]	4.497	7.321	1.628		32.054	
Ih	Expt. [3]	4.498	7.324	1.628			32.082

Comparing the results from different functionals, it can be realized that PBE and WC functionals predict the volume to be smaller than the experimental lattice parameter, while revPBE overestimates the volume. Inclusion of van der Waals forces on these functionals always increases the volume, softening the Hydrogen bonding of the system. However, vdW-DF$^{\mathrm{WC}}$ does not improve over WC results, while vdW-DF$^{\mathrm{PBE}}$ brings results much closer to the experiments than PBE alone. On the other hand, inclusion of van

der Waals with BLYP would shift the results above the experiments, since BLYP itself is already close to the experimental results. Similarly, inclusion of van der Waals forces with revPBE, which already makes ice softer compared to PBE, elongates the hydrogen bonds even more, increasing the volume more. In addition, the isotope effect is almost zero at zero temperature with the vdW-DF$^{\mathrm{revPBE}}$ functional, and this will be discussed in more detail in the following sections. The only functional that predicts a normal isotope effect with Γ point phonon calculation, is vdW-DF2, hence it is not a good candidate to investigate nuclear quantum effects. Therefore, the best functionals to compare the GGA to vdW-DF functionals are PBE and vdW-DF$^{\mathrm{PBE}}$. Hence, we have performed the rest of the calculations with these two functionals.

For the comparison of basis sets, we have performed calculations with the PBE functional with dζ+p and tζ+p basis, and compared our results to the plane wave calculations of Ref. [69]. It is clear that the tζ+p basis improves the results and moves them significantly closer to the plane wave calculations. Therefore, for obtaining the structural properties, such as lattice parameters and volume, tζ+p basis can be considered a good basis.

From the frozen lattice parameter calculations, we realize that the lattice parameters do not change when the protons are fully ordered with a hexagonal symmetry as in BF-ice, or ordered as in ice XI. In both ordered ices, the structures have a net dipole moment along the $\hat{c}$ directions. Comparison to the proton disordered ice Ih with no net dipole moment shows that the ordering mainly changes the c lattice parameter. Proton disordered ice Ih with the PBE functional has the same lattice parameter as the H-ordered ice XI, whereas the proton disordered system with the vdW-DF$^{\mathrm{PBE}}$ functional has a larger volume than the H-ordered structure due to the change in the c lattice parameter.

3.3.2 Phonon Band Diagrams of Proton Ordered Phases

Obtaining the isotope effect from Γ point phonon calculations is not accurate enough, especially for a small system with 4 molecules, like ice XI. In order to improve the results of ice XI, a $3 \times 3 \times 3$ cell is obtained and the force constants matrix of the unit cell within this supercell is calculated within the frozen phonon approximation. Then the phonon bands along certain hexagonal symmetry points are calculated.

As it is shown in Fig. 7, there exist small and negative phonon modes

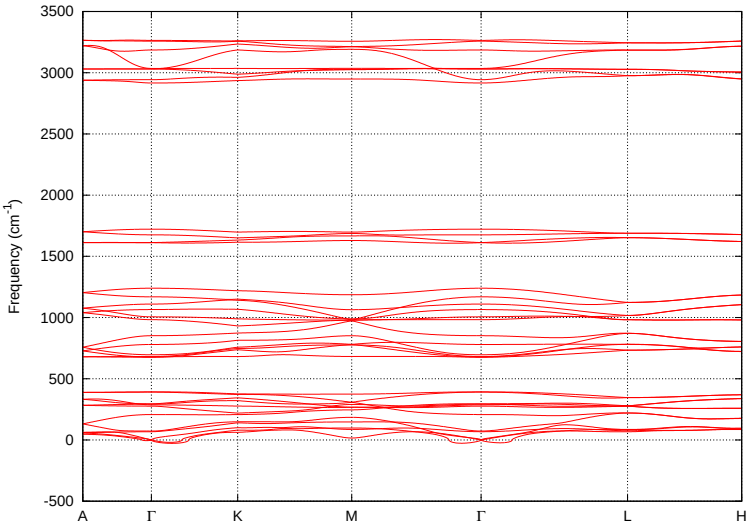

Figure 7: Phonon bands of proton ordered ice XI.

at certain directions, close to the Γ point. These imaginary modes, shown as negative modes in the band diagram might correspond to an instability in the system, which might be due to the proton ordering not obeying the hexagonal symmetry of the system. This was the underlying reason we have obtained an ice, obeying Bernal-Fowler rules with full hexagonal symmetry, both in oxygens and in hydrogens. As explained before, this fully symmetric ordering of the protons over partially symmetric ordering of the protons, did not change the lattice parameter and volume. Furthermore, Fig. 8 shows that this system also has negative phonon modes, hence it can be concluded that these modes do not result from breaking of the symmetry of the system.

Investigating these negative modes shows that they are due to numerical errors in the force constants calculations and phonon frequency calculations. They are almost always orders of magnitude smaller than the rest of the phonon modes, and there are numerical errors within the convergence of force constants matrix. Therefore, in all of the calculations, they are not taken into account, by setting the mode and the corresponding Grüneisen parameter to zero. Because ice XI and BF-ice give similar lattice parameters, and because the negative frequency modes are entirely numerical errors, we conclude that they will give similar structural results. From now on, we assume that BF-ice and ice XI will give similar results, therefore we concentrate only on proton

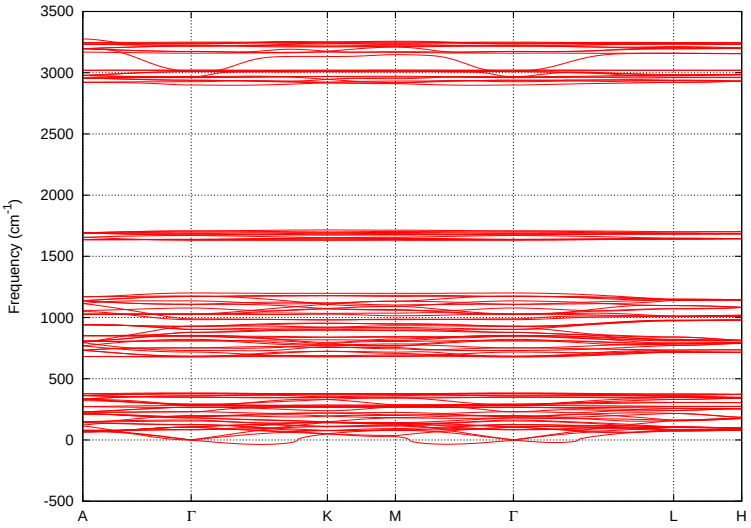

Figure 8: Phonon bands of proton ordered BF-ice.

ordered ice XI and compare it to proton disordered ice Ih.

3.3.3 Projected Phonon Density of States and Grüneisen Parameter

After the analysis of the phonon band structure of the proton ordered structures, we move on to obtaining the phonon modes not only along certain symmetry directions, but also in the full Brillouin zone, for ice XI. This is done by dividing the Brillouin zone of ice XI into $9 \times 9 \times 9 = 729$ k-points, all of them with equal weights. Ice Ih phonon modes are calculated at the Γ point of the 96 molecule cell, which corresponds to 24 k-points when the unitcell is compared to ice XI.

For this estimation, we have performed a careful analysis of the phonon density of states and corresponding Grüneisen parameters, γ_k, of both phases. Correct estimation of Grüneisen parameter plays a crucial role, because the average value $\langle \omega_k \gamma_k \rangle$ determines whether a system has normal or anomalous isotope effect. Negative γ_k's imply a softening of the modes with decreasing volume, favouring larger bulk modulus for a lighter isotope.

Within each structure, considering how frequencies and Grüneisen parameters are grouped together, we can separate the phonon modes into 6 bands. Fig. 9 also shows the average values of the Grüneisen parameters

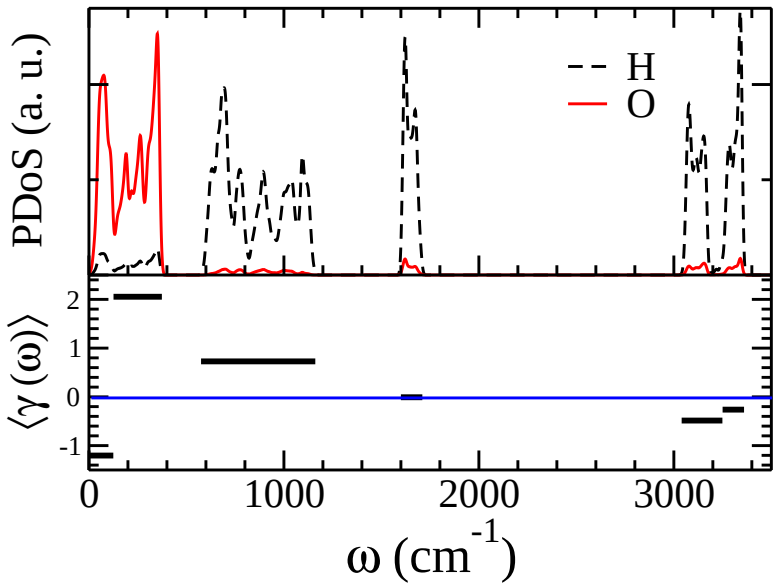

Figure 9: Phonon density of states projected on hydrogen and oxygen for H_2O of proton ordered ice XI.

corresponding to each band.

The highest frequencies correspond to anti-symmetric ($\omega \sim 3314$ cm^{-1} for H_2O) and symmetric ($\omega \sim 3115$ cm^{-1} for H_2O) stretching modes of the O-H covalent bond with a weight mostly on the Hydrogens. The stretching modes have negative γ_k's, favouring anomalous isotope effect.

The bending modes ($\omega \sim 1646$ cm^{-1}) are very harmonic and their γ_k is always around zero, hence, these modes do not play a significant role in the determination of the anomaly of the isotope effect. These modes do not contribute to the interplay between covalent bond stretchings and the Hydrogen bond network.

Libration modes ($\omega \sim 847$ cm^{-1}) are also dominated by the Hydrogens, while the translational modes ($\omega \sim 271$ cm^{-1}) are mostly dominated by Oxygens. But these two modes contribute to the strength of the Hydrogen bonding network, and they clearly have positive γ_k, favouring the normal isotope effect. There is also a band with small frequencies ($\omega \sim 74$ cm^{-1}) that has negative γ_k. This band is also associated with the stretching modes of the Hydrogen bond, and the negative Grüneisen parameters are responsible for the negative thermal expansion of hexagonal ice. [3]

Therefore, there is an anti-correlation between the translational and librational modes, which determine the strength of the Hydrogen bond and the stretching modes which determine the strength of the OH covalent bond. The anomalous isotope effect is a result of a fine balance between cancellations of contributions from each band [6, 71].

3.3.4 Volume Change at T = 0 K

The effect of the Grüneisen parameters on the anomalous isotope effect at the $T = 0$ K limit can be seen easily from the eq. 50. At $T = 0$, $n_k = 0$, it can be seen that $\Delta V = V - V_0$ is proportional to the average $\langle \gamma_k \omega_k \rangle$. The anomalous isotope shift observed when replacing H by D implies that $\Delta V(H_2O) < \Delta V(D_2O)$.

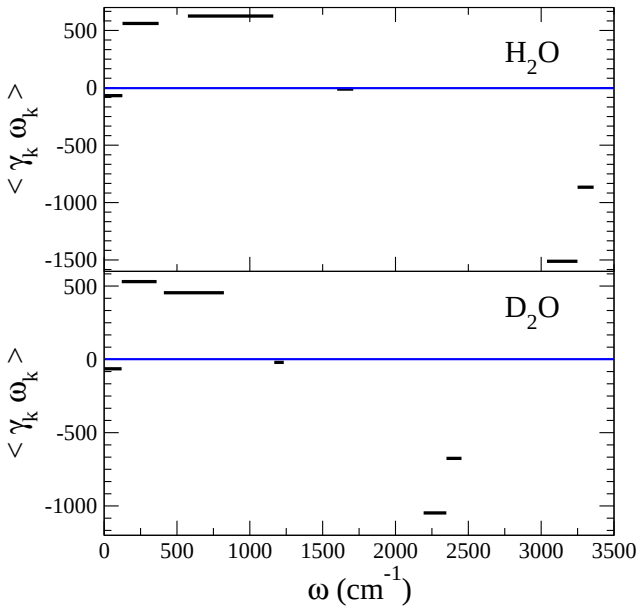

Figure 10: $\langle \gamma_k \omega_k \rangle$ for each phonon branch calculated using vdW-DF$^{\text{PBE}}$. Top: H_2O, bottom: D_2O. The continuous horizontal line indicates $\langle \gamma_k \omega_k \rangle = 0$

Figure 10 shows $< \gamma_k \omega_k >$ for each branch as a function of the frequency for H_2O and D_2O. For both molecules, the translation and libration branches, less energetic than the OH stretching branches, have positive Grüneisen constants. The bending modes have a Grüneisen constant very close to 0, so they contribute very little to the sum. The stretching modes of the covalent OH

bond have negative Grüneisen constants and larger frequency. Therefore, it is clear that in ice Ih, the isotope shift depends on a fine balance between the contribution of the H-bond-related frequencies with $\gamma_k > 0$ and the branches related to the OH covalent bond with $\gamma_k < 0$.

3.3.5 Volume as a Function of Temperature

Table 3 shows the $T = 0$ K volumes for several isotope combinations of H, D, ^{16}O, and ^{18}O, for all the DFT functionals [7, 8, 10, 60] and the force fields used in this study. Also included in this table is a 32 beads PIMD result for a single unit cell (Γ sampling) using the PBE-DF, compared to a calculation with the QHA for an identical system. The simulation was done at $T = 200$ K [6].

As the experimental study from Röttger *et al.* did not consider $H_2{}^{18}O$, high resolution X-ray diffraction experiments of the three isotopes H_2O, D_2O and $H_2{}^{18}O$ were performed. Results are presented in Table 3.

With the exception of vdW-DF$^{\mathrm{revPBE}}$, all of the XC functionals predict an anomalous isotope effect at $T = 0$ K when H is replaced by D, in agreement with experiments. However, the isotope effect has the normal sign for the O atom. Experiments confirm this result, with a 0.06% volume contraction when ^{18}O replaces ^{16}O (T=100K) [6]. The comparison of structures (ii) and (iii) shows that the results are largely independent of the ordering of the protons. Agreement with experiments improves as Brillouin zone integration is improved. With respect to their generalized gradient approximation (GGA) counterparts, vdW-DFs soften the afore-mentioned anticorrelation effect, reducing the magnitude of the H→D isotope shift, but have little effect on the O shift. When phonons from the full Brillouin zone are accounted for, the vdW-DF$^{\mathrm{revPBE}}$ fails to predict the isotope shift at $T = 0$. However the anomalous shift for this functional is recovered at $T > 100$ K [6]. Overall, vdW-DF$^{\mathrm{PBE}}$ has proven to be very robust for a variety of structural and dynamical properties of water [8, 15, 72]. It also gives our best lattice constant for ice at T=0 K.

Table 3: DFT volume (in Å^3/molecule) for proton ordered (H-ordered) and proton disordered (H-disordered) ice Ih for different isotopes, obtained with the quasiharmonic approximation (QHA) or path integral (PIMD) simulations, which are obtained within our collaboration[6]. k-mesh is the effective number of **k** points for sampling the 4-molecule hexagonal Brillouin zone in the phonon calculation (one for Γ-sampling). IS(A-B)=$\frac{V(A)}{V(B)}-1$, is the relative isotope shift for the exchange of isotope A by B. The exchange and correlation (XC) functionals are: PBE [7], vdW-DF$^{\rm PBE}$ [8, 9], revPBE [10], and vdW-DF$^{\rm revPBE}$ [8]. The force fields (FF) are q-TIP4P/F[11] and TTM3-F[12] V_{cla} is the volume for classical nuclei. Also shown are the experimental results from ref [3] and the ones obtained within our collaboration ref [6]. Note they are at different temperatures.

T(K)	k-mesh	Ice	Method	XC/EFF	V_{cla}	H_2O	D_2O	$H_2{}^{18}O$	IS(H-D)	IS(^{16}O -^{18}O)
200	1	XI	PIMD[6]	PBE		31.02	31.21		−0.61%	
200	1	XI	QHA	PBE	30.6	30.00	30.16	29.98	−0.53%	+0.07%
0	24	Ih	QHA[6]	q-TIP4P/F	30.98	32.30	32.13	32.24	+0.53%	+0.18%
0	24	Ih	QHA	TTM3-F	31.66	31.67	31.67	31.67	+0.002%	+0.002%
0	24	Ih	QHA	PBE	29.91	29.93	30.04	29.91	−0.35%	+0.07%
0	24	Ih	QHA	vdW-DF$^{\rm PBE}$	30.90	31.20	31.30	31.14	−0.32%	+0.19%
0	1	XI	QHA	PBE	29.98	29.91	30.05	29.89	−0.47%	+0.07%
0	1	XI	QHA	vdW-DF$^{\rm PBE}$	30.88	31.01	31.10	30.98	−0.29%	+0.10%
0	1	XI	QHA	revPBE	32.84	32.88	32.98	32.85	−0.30%	+0.09%
0	1	XI	QHA	vdW-DF$^{\rm revPBE}$	33.45	33.73	33.76	33.70	−0.09%	+0.09%
0	729	XI	QHA	PBE	29.98	30.09	30.19	30.07	−0.33%	+0.07%
0	729	XI	QHA	vdW-DF$^{\rm PBE}$	30.88	31.17	31.22	31.14	−0.16%	+0.10%
0	729	XI	QHA	revPBE	32.84	33.18	33.23	33.15	−0.15%	+0.09%
0	729	XI	QHA	vdW-DF$^{\rm revPBE}$	33.45	33.95	33.94	33.92	+0.03%	+0.09%
10		Ih	Exp[3]			32.054(5)	32.082(3)		−0.089(18)%	
100		Ih	Exp[3]			32.047(3)	32.072(5)		−0.079(18)%	
100		Ih	Exp[6]			32.079(4)	32.103(4)	32.058(4)	−0.076(18)%	0.064(18)%
220		Ih	Exp[3]			32.368(4)	32.437(3)		−0.212(15)%	
220		Ih	Exp[6]			32.367(4)	32.429(4)	32.357(4)	−0.191(17)%	0.032(17)%
qζ+dp										
0	24	Ih	QHA	PBE	30.51	30.52	30.68	30.49	−0.52%	+0.10%
0	24	Ih	QHA	vdW-DF$^{\rm PBE}$	31.24	31.52	31.60	31.49	−0.25%	+0.10%
0	729	XI	QHA	PBE	30.48	30.64	30.78	30.60	−0.46%	+0.13%
0	729	XI	QHA	vdW-DF$^{\rm PBE}$	31.08	31.45	31.52	31.41	−0.32%	+0.13%

Therefore, in the following we use this functional and the QHA to explore the volume of ice Ih in structure (ii), including full Brillouin zone phonon integration, as a function of isotope masses and temperature. However, the results, and in particular the anomalous isotope effect, are very robust and largely independent of the XC functional, harmonic approximation, system size, and proton ordering.

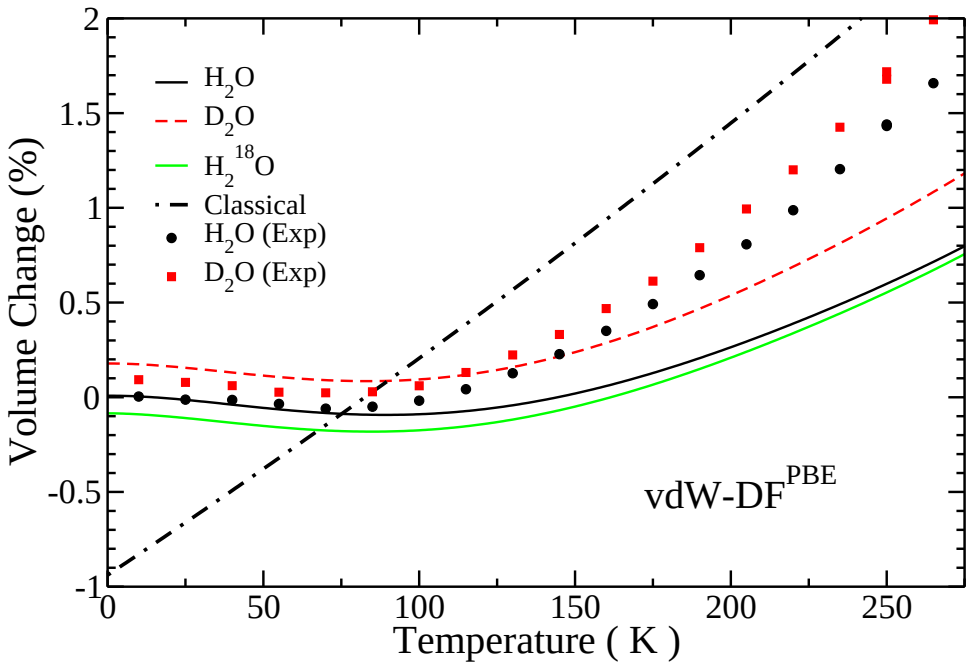

Figure 11: Volume change $V(T)/V_{\mathrm{H_2O}}(0) - 1$, relative to H_2O at $T = 0$, for different isotopes calculated using the QHA with the vdW-DF$^{\mathrm{PBE}}$ functional. Also shown are the experimental results from Ref. [3].

Fig. 11 shows $V(T)$ of ice Ih for standard isotope substitutions of H and O. Experimentally, the anomalous H→D isotope effect increases from 0.09% at $T = 10$ K to 0.25% at $T = 250$ K, and this increase is reproduced by our calculations (from 0.16% to 0.32%). The classical volume becomes larger than any of the quantum results above 100 K.

This implies that, for larger temperatures, a classical isobaric *ab initio* molecular dynamics simulation of ice will overestimate its volume, relative to a quantum PIMD simulation.

Substitution of ^{16}O by ^{18}O affects mainly the low frequency modes, dom-

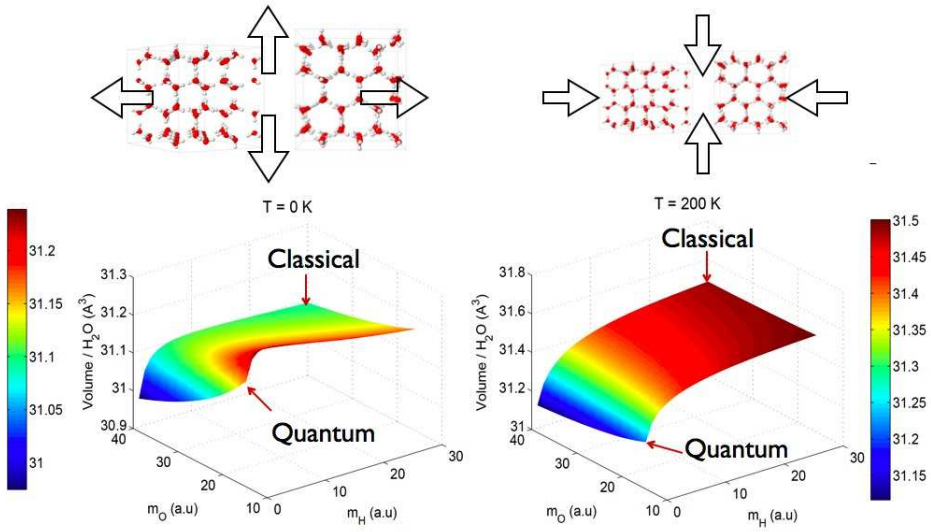

Figure 12: Volume as a function of atomic mass of oxygen and hydrogens for $T = 0$ K (on the left) and $T = 200$ K (on the right). The colour shows the volume increase from small (blue) to large (red) volume. Note that at T=0K, the classical limit is below the quantum volume, while it is above at T=200K.

inated by positive values of γ_k, producing a normal isotope effect. The temperature dependence of the isotopic O substitution is also normal, and the volume shift is 50% smaller at T=220 K than at T=100 K. This is illustrated in Fig. 12, where the volume per molecule is plotted as a function of oxygen and hydrogen mass for two different temperatures, starting from the quantum regime (H_2O) and moving towards the classical regime where the oxygen and hydrogen mass goes to infinity. At $T = 0$ K, around the quantum regime, an increase in the hydrogen mass results in an increase in the volume, demonstrated in the red points on the plot. However, an increase in the oxygen mass results in a decrease in the volume, demonstrated in the blue points. Moreover, the volume in the classical limit is smaller than the quantum volume at $T = 0$ K, but at large temperatures, $T = 200$ K, the volume at the classical limit is always larger than the quantum limit.

Somewhat surprisingly, the net effect at $T = 0$, relative to classical nuclei, is dominated by quantum oxygen, resulting in a quantum volume ∼1% larger, This small expansion (10 times smaller than that of Ne) is a consequence

of two competing anharmonicities: the contraction effect of H-dominated stretching modes and the expansion effect of librational and translational modes. As T increases, the contribution of the stretching modes becomes dominant, causing the net quantum effect to change sign and to become anomalous above $\sim$70 K. This dominance increases with T, making the volume shift four times larger at the melting temperature than at T=0. These results are not inconsistent with the requirement that, at high enough T the isotope shift is isotope independent, but we find that the convergence towards the classical limit starts at T>$\sim$900 K.

Our results may also have significant implications for the understanding of nuclear quantum effects in liquid water (in which the anomalous isotope shift is experimentally larger than in ice [18]). PIMD simulations, using the q-TIP4P/F and TTM3-F EFFs, produce a less structured liquid than classical MD simulations [11, 12, 42]. However, as we have seen, these EFFs do not reproduce the anomalous isotope effect in ice, because they fail to describe accurately the derivatives of the frequencies, which govern the anharmonicities and the nuclear quantum effects in the structure and dynamics. This suggests that these models may be inadequate to reproduce some quantum effects in the liquid as well as in the solid. Therefore, the observed loss of structure in the liquid, for quantum vs classical nuclei, should be reanalyzed with an EFF that reproduces the anomalous quantum effects in ice.

Note that all these results are obtained with tζ+p basis, as published in Ref [6]. After publication of this work, came the improvement of the basis sets, and we have developed the method to reevaluate the volume dependency of Kohn-Sham energy with qζ+dp basis, as will be explained in Section 4.2. The improvement in the volume calculations does not change any of the discussion and conclusions of this chapter, but improving the energy will become more important in the following chapters. Therefore, the improved results of the volume calculations are included in the Table 3 and we will refer to these numbers in the rest of the discussions of this thesis.

3.4 Conclusion

We have shown that the anomalous nuclear quantum effects on the volume of hexagonal ices can be fully understood using the quasi-harmonic approximation with density functional theory. The main reason of the anomaly is the anti-correlation between inter-molecular Hydrogen bonds, dominated by the low frequency modes with positive Grüneisen parameters, and intra-

molecular covalent bonding, dominated by the high frequency modes with negative Grüneisen parameters. The theory with a correct description of these anharmonicities should correctly reproduce not only the phonon frequencies, but also the derivatives of the frequencies. Therefore, the EFFs tested in this study still have room for improvement on how they describe these anharmonicities, and DFT is the level of the theory needed for this type of study. We have also shown that inclusion of non-local forces with the vdW-DF functional improves over the semi-local PBE functional and is the best candidate to predict the experimental results so far.

4 Nuclear Quantum Effects on the Bulk Modulus of Hexagonal Ices

Similar to the anomalous nuclear quantum effects in the volume of hexagonal ices, it is expected that there is also an anomalous isotope effect in the bulk modulus. The bulk modulus of the heavy ice (D_2O) is expected to be smaller than the bulk modulus of normal ice (H_2O) [73]. Moreover, the anisotropy in the wurtzite structure reveals itself, not only in the lattice parameters, but also in the bulk modulus along different directions. This can be analysed extensively with a detailed calculation of the different components of the strain tensor.

In addition to lattice parameter experiments, there is a clear need for precise bulk modulus experiments, due to a dispersion of experimental values in the literature (see Ref. [4] and the references therein). For comparison with our calculations, we report some of the frequently referred experimental values [4, 13, 74]. Furthermore, understanding how the bulk modulus changes in different directions of lattice parameters would give a better insight into the anisotropy of the structures. There is a clear anisotropy when lattice parameters are considered, but how the compressibility is affected by this anisotropy is not well understood. The dispersion in the experimental results as well as the lack of theoretical analysis of anisotropy in the bulk modulus needs to be addressed.

In this chapter, we will show the anisotropy of the hexagonal ices by calculating the related strain tensor components. By re-evaluating Helmholtz free energy with more converged computational calculations than in the previous chapter, we also calculate the nuclear quantum effects in the bulk modulus.

4.1 Initial Analysis of the Structure and Preliminary Calculation of the Frozen Bulk Modulus

In order to obtain a fast and accurate calculation of the bulk modulus, three methods were used for ice XI unit cell calculations. The structure is obtained from the equilibrium lattice configuration with $V_0 = 29.92$Å in the Table 4. We have changed the volume of the cell by changing both lattice parameters by 0.15%. As the volume changes, we have:

(i) relaxed all the atoms in the cell (labelled "Relax All");

(ii) rescaled only the O-O distance, keeping the O-H covalent bond length constant (labelled "Rescale Oxygen");

(iii) rescaled all the atomic positions, without relaxation (labelled "Rescale All" in the table).

These methods also give an insight into the structure of the hexagonal ice XI, in terms of how the energy, pressure and the bulk modulus change, when different bond lengths are constrained. All the rescaling is done with respect to the relaxed configuration at the minimum of the $E_0(V)$ curve. Then we have calculated the Kohn-Sham energy, E_0 and pressure of the new system. All calculations are performed with the PBE functional and the tζ+p basis set, as explained in the previous chapter.

The bonds that correspond to the molecules directed along the x-y plane are labelled 1. The bond of a molecule directed along the z direction is labelled 3, and the other bond of the same molecule that is along the x-y plane is labelled 2. This labelling is also shown in the Fig. 13.

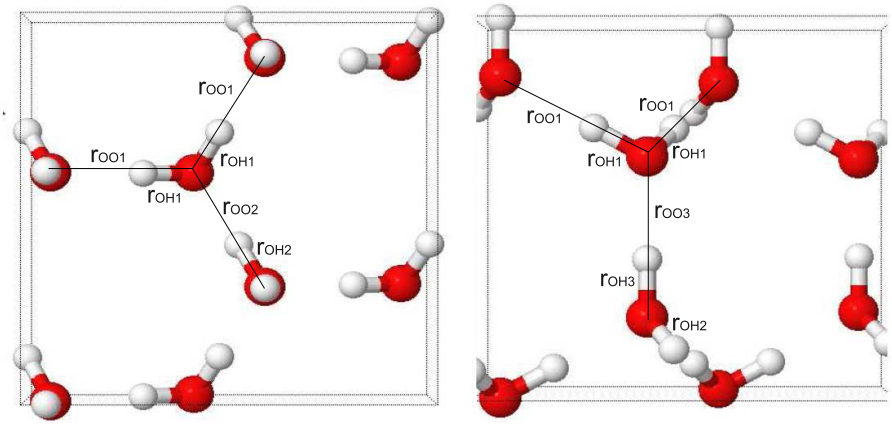

Figure 13: Unit cell of the H-ordered ice XI structure. The image on the right is the top view of the x-y plane; the image on the left is the side view of the x-z plane. Red symbolizes the Oxygens and white symbolizes the Hydrogens. r_{OO} and r_{OH} shows the O-O distances and O-H distances as labelled in Table 4 below.

Table 4 shows how the O-O distances and O-H covalent bond lengths change with volume for each method. The O-O distances are the same, when only oxygen atoms are rescaled and all atoms are rescaled. However, these distances are underestimated when the volume is rescaled to lower volumes

from $V_0 = 29.92$Å and overestimated for larger volumes. When only the oxygen atoms are rescaled, the O-H distances are kept the same as those of V_0. Similar to O-O distances, when everything is rescaled to lower volumes, O-H distances are underestimated.

Table 4: Bond lengths as the atomic positions are rescaled with volume change using different methods with the PBE functional. V is the volume per molecule. All the distances are in units of Å and volume in Å^3.

	Relax All			Rescale Oxygen			Rescale All		
V	r_{OO1}	r_{OO2}	r_{OO3}	r_{OO1}	r_{OO2}	r_{OO3}	r_{OO1}	r_{OO2}	r_{OO3}
29.65	2.6801	2.6802	2.6817	2.6774	2.6828	2.6847	2.6774	2.6828	2.6847
29.78	2.6841	2.6841	2.6859	2.6828	2.6854	2.6873	2.6828	2.6854	2.6873
29.92	2.6881	2.6881	2.6900	2.6881	2.6881	2.6900	2.6881	2.6881	2.6900
30.05	2.6922	2.6922	2.6941	2.6935	2.6908	2.6927	2.6935	2.6908	2.6927
30.19	2.6962	2.6962	2.6977	2.6989	2.6935	2.6954	2.6989	2.6935	2.6954
	Relax All			Rescale Oxygen			Rescale All		
V	r_{OH1}	r_{OH2}	r_{OH3}	r_{OH1}	r_{OH2}	r_{OH3}	r_{OH1}	r_{OH2}	r_{OH3}
29.65	1.0074	1.0074	1.0072	1.0067	1.0068	1.0065	1.0007	1.0008	1.0005
29.78	1.0070	1.0071	1.0069	1.0067	1.0068	1.0065	1.0037	1.0038	1.0035
29.92	1.0067	1.0068	1.0065	1.0067	1.0068	1.0065	1.0067	1.0068	1.0065
30.05	1.0064	1.0065	1.0062	1.0067	1.0068	1.0065	1.0097	1.0098	1.0096
30.19	1.0060	1.0061	1.0059	1.0067	1.0068	1.0065	1.0128	1.0128	1.0126

In addition to calculating the bulk modulus from the curvature of the energy, as given in eq. 53 (labelled B_0^E in Table 5), the bulk modulus can also be obtained from the slope of the volume dependency of the pressure, as given in eq. 55:

$$B_0^P = -V_0 \left.\frac{\partial P}{\partial V}\right|_{V=V_0} \tag{55}$$

Table 5 shows the bulk modulus calculated from eq. 53 and eq. 55 for each of these three methods. Rescaling all the distances without any relaxation clearly gives non-physical bulk modulus results, as the experimental bulk modulus of hexagonal ice is reported to be between 8-12 GPa [4, 13, 74]. Rescaling O-O distances while keeping the O-H covalent bond seems to give a $\sim 50\%$ higher bulk modulus compared to relaxing all the atoms in the cell, which seems to give the most physical results. Also, comparing B_0^E and B_0^P, relaxing all the atoms give similar results for isotropic change in the lattice parameters. Therefore, the most physical results are obtained by B_0^E from

Table 5: Bulk modulus of the system calculated both from energy and pressure for different rescaling methods with the PBE functional. Note that volume is the unit cell volume of 4 molecules and is given in units of Å^3. Bulk modulus results are in GPa.

	Relax All	Rescale Oxy	Rescale All
V_0	119.615	119.632	119.670
B_0^E	17.924	46.253	220.057
B_0^P	16.815	27.286	116.272

eq. 53 and full cell relaxations are very important for accurate calculations. It should be noted that the B_0 is very sensitive to the fitting to the energy. This shows that obtaining accurate bulk modulus results is difficult both theoretically, as well as experimentally.

4.2 Fast and Accurate Calculations with tζ+p and qζ+dp Basis Sets

Even though results with the tζ+p basis are accurate enough for general structural purposes, for precise order-disorder free energy values, the energy must be very well converged. Recently, a systematic method to obtain the finite-range atomic basis sets for liquid water and ice has been proposed [36]. We use quadrupole-ζ double polarized (qζ+dp) basis obtained with the new proposed framework, to calculate the energy of the relaxed configuration of the tζ+p basis in order to refine the Kohn-Sham energy calculations. SIESTA input files for both basis sets are given in Appendix A.

The relaxation calculations with the qζ+dp basis is computationally more expensive. In order to address this, we propose to calculate the structural relaxations with a computationally affordable basis, the tζ+p basis in this case, and then perform an energy calculation of the relaxed configuration with the qζ+dp basis. To test the validity of this method, we have performed full structure relaxations with the qζ+dp basis with the vdW-DF$^{\text{PBE}}$ functional only with ice XI structure, since four molecule calculations are computationally affordable. As shown in Fig. 14, for the same configuration, the energy difference between the tζ+p basis and the qζ+dp basis is 948.6 meV, whereas the energy changes only by 1.3 meV when the configurational relaxation is performed for the qζ+dp basis.

In addition, the equilibrium volume V_0 at the Kohn-Sham energy mini-

mum shifts from the tζ+p basis to the qζ+dp basis for the same configuration, but more importantly, there is no volume shift when the qζ+dp basis configurational relaxation is performed. For the tζ+p basis, the error compared to the qζ+dp basis is -0.23% in lattice constant a, is -0.28% in c, and is -0.71% in the total volume. When we perform the qζ+dp basis calculations at the tζ+p basis relaxed configurations, we get exactly the same equilibrium lattice parameters and volume as the full relaxations with the qζ+dp basis. This shows that we can perform structural relaxations with a computationally affordable basis and then calculate the energy of these configurations with a very well converged basis. With this method, we get two fold convergence, both in electronic energy, i.e. along y-axis of Fig. 14, and in structural volume , i.e. along x-axis of Fig. 14. Once, the curve for Kohn-Sham energy as a function of volume, $E_0(V)$ is obtained, the classical volume is calculated from the minimum of a third order polynomial fit to this data.

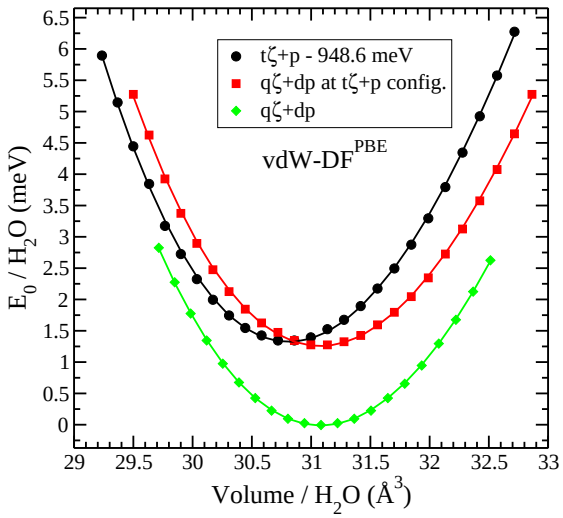

Figure 14: Relative Kohn-Sham energy as a function of volume for the vdW-DF$^{\mathrm{PBE}}$ functional. The equilibrium energy of fully relaxed structure with the qζ+dp basis is set to 0 eV. The equilibrium energy of fully relaxed structure with the tζ+p basis is set is shifted by 948.6 meV to show them in the same frame. The qζ+dp basis energy difference between the fully relaxed structure and the tζ+p basis relaxed structure is 1.3 meV. The dots are the calculated data and the lines are a third order polynomial fit to the data.

For the free energy calculations which include the nuclear quantum effects, the vibrational modes are calculated using the frozen phonon approximation. All the force constant calculations are performed with the tζ+p basis. There are two reasons for this: the tζ+p basis giving a good first approximation to the configurational information, and the high computational time cost of the qζ+dp basis. In addition, the largest error in the free energy calculations comes from the initial E_0(V) contribution, which we reduce significantly with this introduced method. The error from the zero point energy contribution is much smaller compared to the electronic energy contribution. Therefore, the phonon frequency calculation details and the parameters used to obtain the force constants matrix are the same as in Chapter 3.

4.3 Antiferroelectric Proton Ordered Ice XI: Ice aXI

The proton ordering of structure of ice XI is determined to be ferroelectric by experiments [75–78]. However, there is a debate about whether the proton ordering is ferroelectric or antiferroelectric from a theoretical standpoint. Force field models give different predictions as the most stable phase depending on the model and parametrization [79, 80]. However, DFT calculations agree with the experiments that the most stable phase of ice XI is ferroelectric ordered phase [81, 82]. Therefore, we have included one more phase to our hexagonal ices to compare the bulk modulus properties of antiferroelectric ordered ice aXI to those of ferroelectric ordered ice XI and disordered ice Ih. Our main aim in the following chapter will be to study the nuclear quantum effects in the transition temperature between proton disordered ice Ih, ferroelectric proton ordered ice XI, and antiferroelectric proton ordered ice aXI. Therefore, it is important to understand its structural properties first in this chapter.

The structure of antiferroelectric proton ordered ice, which we have chosen to label, ice aXI, is presented in Fig. 15. Ice aXI has 8 molecules in the unit cell with dipole moment pointing in opposite directions such that the system has no net dipole moment.

4.4 Classical Lattice Parameter

In order to interpret the dynamics behind the phase transition, first, we determine the lattice parameter of each system. Lattice parameters are kept constant within each relaxation, and varied systematically to cover the E(a,c)

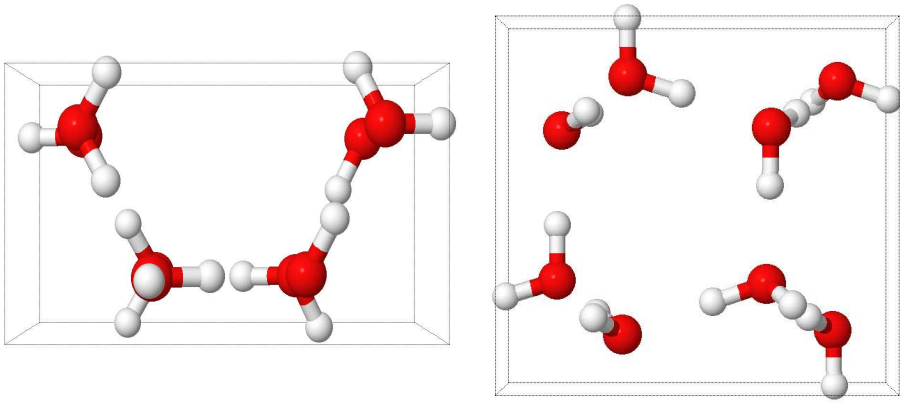

Figure 15: Antiferroelectric proton ordered ice XI structure. The image on the left is the top view of the x-y plane; the image on the right is the side view of the x-z plane.

surface. The optimal lattice parameters are selected considering the minimum of the E(a,c) surface, the E(V) curve, and the proximity to the zero pressure region. The optimum lattice parameters with highly converged qζ+dp atomic orbital basis are shown in Table. 6.

We also present experimental lattice parameters from Ref. [76] as they study neutron diffraction of both ice XI and ice Ih, in detail. They compare the orthorhombic structure of ice XI with the hexagonal structure of ice Ih. Since we keep the hexagonal symmetry in our ice XI calculations, we compare the experimental lattice parameter a, of ice Ih to the experimental lattice parameters $\sqrt{(ab/\sqrt{3})}$ of ice XI. In this case, we see that the experimental lattice parameter a changes very slightly from the ordered to disordered phase, whereas the lattice parameter c changes significantly [76].

We have calculated that proton disordered ice Ih with the PBE functional has the same lattice parameter as both proton ordered ices, ice XI and ice aXI. Ice Ih with the vdW-DF$^{\mathrm{PBE}}$ functional has a larger volume than ferroelectric proton ordered ice XI, and this change in the volume is due to the change in the lattice parameter c, which is in good agreement with the experimental results, again showing the importance of inclusion of van-der Waals forces in these calculations. On the other hand, the antiferroelectric proton ordered ice aXI has larger volume than both ice Ih and ice XI. The lattice parameter

Table 6: a and c lattice parameters, their ratio (c/a), and the corresponding volume per molecule, Volume/H_2O= $a^2c\sqrt{3}/2/N_{H_2O}$, for the force field model (FF) and exchange and correlation functional (XC). All lengths are in Å and volumes in Å^3.

FF/XC	Ice	a	c	c/a	Volume/H_2O
TTM3-F	Ih	4.54	7.41	1.632	33.07
TTM3-F	aXI	4.55	7.41	1.629	33.21
TTM3-F	XI	4.54	7.43	1.637	33.16
PBE	Ih	4.42	7.21	1.631	30.49
PBE	aXI	4.42	7.21	1.631	30.49
PBE	XI	4.42	7.21	1.631	30.49
vdW-DF^{PBE}	Ih	4.45	7.27	1.634	31.17
vdW-DF^{PBE}	aXI	4.46	7.25	1.624	31.18
vdW-DF^{PBE}	XI	4.45	7.25	1.629	31.08
Expt. [3] 10K H_2O	Ih	4.497	7.321	1.628	32.05
Expt. [3] 10K D_2O	Ih	4.498	7.324	1.628	32.08
Expt. [76] 5K D_2O	Ih	4.497	7.324	1.629	32.07
Expt. [76] 5K D_2O	XI	4.501	7.292	1.620	31.98

a of this structure is smaller than that of ice Ih, and lattice parameter c is larger than that of ice Ih. The difference in the volume from ice XI is only due to the change in the lattice parameter a. Comparing vdW-DF^{PBE} results to the experimental lattice parameter changes between ordered and disordered phases indicates that this functional gives similar lattice changes to the experiments between the ferroelectric proton ordered ice XI and proton disordered ice Ih. Moving on to the TTM3-F force field model, ice Ih has a smaller volume than ice XI, which is opposite to the experimental results; and ice aXI has the largest volume. The change in volume with TTM3-F is due to the lattice parameter a when ordering is from ice Ih to antiferroelectric ordered ice aXI, and is due to the lattice parameter c when ordering is from ice Ih to ferroelectric ordered ice XI. The changes in the lattice parameter c is opposite with TTM3-F to those from the vdW-DF^{PBE} functional. This shows that only a DFT calculation with vdW-DF^{PBE} functional predicts the correct lattice structure and volume behaviour, as compared to the experimental results, demonstrating the importance of using *ab initio* calculations with the inclusion of non-local van der Waals forces to correctly predict these values.

4.5 Strain Tensor and Bulk Modulus Relations

Now that we have developed the computational methods to obtain the bulk modulus of the system, and established the structural anisotropy in the system with a detailed optimization of the lattice parameters, we can focus on calculating the anisotropy in the bulk modulus of hexagonal ices. In order to do this, let us first obtain the relationships between the different directional components of the total bulk modulus, by calculating the strain tensor.

When there is a small uniform deformation on a solid, the axes are distorted in orientation by $\epsilon_{\alpha\beta}$. [83] Then the displacement of an atom due to this deformation can be defined as:

$$\begin{aligned} \mathbf{R}(\mathbf{r}) &\equiv (x\epsilon_{xx} + y\epsilon_{yx} + z\epsilon_{zx})\hat{x} + (x\epsilon_{xy} + y\epsilon_{yy} + z\epsilon_{zy})\hat{y} \\ &\quad +(x\epsilon_{xz} + y\epsilon_{yz} + z\epsilon_{zz})\hat{z} \\ &= u(\mathbf{r})\hat{x} + v(\mathbf{r})\hat{y} + w(\mathbf{r})\hat{z} \end{aligned} \tag{56}$$

From the displacement, the coefficients of the strain tensor can be defined by the relation

$$e_{\alpha\beta} \equiv \epsilon_{\alpha\beta} = \frac{\partial u_\alpha}{\partial x_\beta} + \frac{\partial u_\beta}{\partial x_\alpha} \tag{57}$$

where α and β runs over the $\hat{x}, \hat{y}, \hat{z}$ directions.

Within the approximation of Hooke's law, we can write the elastic energy density as a quadratic function of the strains as follows,

$$\frac{\Delta E}{V} = \frac{1}{2}\sum_{\lambda=1}^{6}\sum_{\mu=1}^{6}\tilde{C}_{\lambda\mu}e_\lambda e_\mu \tag{58}$$

where $1 \equiv xx$; $2 \equiv yy$; $3 \equiv zz$; $4 \equiv yz$; $5 \equiv zx$; $6 \equiv xy$.

Noting that only certain combinations enter the stress-strain relations, the elastic stiffness constants are symmetrical;

$$C_{\alpha\beta} = \frac{1}{2}\left(\tilde{C}_{\alpha\beta} + \tilde{C}_{\beta\alpha}\right) = C_{\beta\alpha} \tag{59}$$

Furthermore, we change the lattice parameters along the lattice directions in the hexagonal ice system. Therefore, we are interested only in symmetry-preserving strains: $e_{xx} = e_{yy} = \Delta a/a$ and $e_{zz} = \Delta c/c$ and there are no shear

strains. This reduces the elastic stiffness constants to the upper left 3×3 part of the elasticity tensor. Then eq. 58 becomes;

$$\begin{aligned}
\frac{\Delta E}{V} &= \frac{1}{2}[\tilde{C}_{11}e_1e_1 + \tilde{C}_{22}e_2e_2 + \tilde{C}_{33}e_3e_3 \\
&\quad +(\tilde{C}_{12} + \tilde{C}_{21})e_1e_2 \\
&\quad +(\tilde{C}_{13} + \tilde{C}_{31})e_1e_3 \\
&\quad +(\tilde{C}_{23} + \tilde{C}_{32})e_2e_3] \\
&= \frac{1}{2}[C_{11}e_{xx}^2 + C_{22}e_{yy}^2 + C_{33}e_{zz}^2 + 2C_{12}e_{xx}e_{yy} \\
&\quad +2C_{13}e_{xx}e_{zz} + 2C_{23}e_{yy}e_{zz}] \\
&= \frac{1}{2}[2C_{11}e_{xx}^2 + C_{33}e_{zz}^2 + 2C_{12}e_{xx}^2 + 4C_{13}e_{xx}e_{zz}] \\
&= \frac{1}{2}\left[2(C_{11} + C_{12})\left(\frac{\Delta a}{a}\right)^2 + C_{33}\left(\frac{\Delta c}{c}\right)^2 \right. \\
&\quad \left. + 4C_{13}\left(\frac{\Delta a}{a}\right)\left(\frac{\Delta c}{c}\right)\right] \qquad (60)
\end{aligned}$$

More simply, we can also write this as:

$$\frac{\Delta E}{V} = \frac{1}{2}\left(\ \Delta a/a,\ \ \Delta a/a,\ \ \Delta c/c\ \right)\begin{pmatrix} C_{11} & C_{12} & C_{13} \\ C_{12} & C_{11} & C_{13} \\ C_{13} & C_{13} & C_{33} \end{pmatrix}\begin{pmatrix} \Delta a/a \\ \Delta a/a \\ \Delta c/c \end{pmatrix} \qquad (61)$$

Let us now consider dilation under hydrostatic pressure.

$$\delta \equiv \frac{V' - V}{V} = e_{xx} + e_{yy} + e_{zz} \qquad (62)$$

By using the definition of bulk modulus, we can link dilation to energy as $\frac{\Delta E}{V} = \frac{1}{2}B\delta^2$. Combining this with the last part of eq. 60, we can see that when we only change lattice parameter a, the dilation is $\delta = 2\Delta a/a$ and bulk modulus we get corresponds to:

$$\begin{aligned}
\frac{\Delta E}{V} &= \frac{1}{2}[2(C_{11} + C_{12})\frac{\delta^2}{4}] \\
B_a &= \frac{C_{11} + C_{12}}{2} \qquad (63)
\end{aligned}$$

Similarly, when we change only the lattice parameter c, the dilation is $\delta = \Delta c/c$ and bulk modulus we get corresponds to:

$$\begin{aligned} \frac{\Delta E}{V} &= \frac{1}{2} C_{33} \delta^2 \\ B_c &= C_{33} \end{aligned} \tag{64}$$

This shows that calculations for hexagonal ice, by varying values of a and c near the minimum, we acquire theoretical values of three constants of interest, $(C_{11} + C_{12})$, C_{13}, and C_{33}. There are three other elastic constants, that one can only compute by calculating energies of sheared structures: $C_{11} - C_{12}$, C_{14} and C_{44}.

To obtain C_{13} let us again consider hydrostatic pressure. The stress tensor is then $\sigma_{\alpha\beta} = P\delta_{\alpha\beta}$. In 6-component vector notation, we only need the first three components. The relation between stress and symmetry-conserving strain becomes

$$\begin{pmatrix} P \\ P \\ P \end{pmatrix} = - \begin{pmatrix} C_{11} & C_{12} & C_{13} \\ C_{12} & C_{11} & C_{13} \\ C_{13} & C_{13} & C_{33} \end{pmatrix} \begin{pmatrix} \Delta a/a \\ \Delta a/a \\ \Delta c/c \end{pmatrix} \tag{65}$$

If we equate the pressure in the first two equations from the matrix, we get the relations between $\Delta a/a$ and $\Delta c/c$.

$$(C_{11} + C_{12} - 2C_{13}) \frac{\Delta a}{a} = (C_{33} - C_{13}) \frac{\Delta c}{c} \tag{66}$$

This gives us relations between $\Delta V/V$ and $\Delta a/a$ and $\Delta c/c$,

$$\begin{aligned} \frac{\Delta V}{V} = 2\frac{\Delta a}{a} + \frac{\Delta c}{c} &= \left[\frac{2(C_{33} - C_{13})}{C_{11} + C_{12} - 2C_{13}} + 1 \right] \frac{\Delta c}{c} \\ &= \left[2 + \frac{C_{11} + C_{12} - 2C_{13}}{C_{33} - C_{13}} \right] \frac{\Delta a}{a} \end{aligned} \tag{67}$$

Finally, the bulk modulus is defined by $P = -B\Delta V/V$, from the second

equation of the P matrix

$$\begin{aligned} B &= (2C_{13}\frac{\Delta a}{a} + C_{33}\frac{\Delta c}{c}) \\ &\quad (\frac{C_{33}-C_{13}}{2C_{33}-2C_{13}+C_{11}+C_{12}-2C_{13}}\frac{a}{\Delta a}) \\ &= (2C_{13}\frac{\Delta a}{a} + C_{33}\frac{(C_{11}+C_{12}-2C_{13})}{C_{33}-C_{13}}\frac{\Delta a}{a}) \\ &\quad (\frac{C_{33}-C_{13}}{2C_{33}-4C_{13}+C_{11}+C_{12}}\frac{a}{\Delta a}) \\ &= \frac{2C_{13}(C_{33}-C_{13})+C_{33}(C_{11}+C_{12}-2C_{13})}{2C_{33}-4C_{13}+C_{11}+C_{12}} \\ &= \frac{C_{33}(C_{11}+C_{12})-2C_{13}^2}{C_{11}+C_{12}+2C_{33}-4C_{13}} \end{aligned} \tag{68}$$

Now that we know B, $(C_{11}+C_{12})$, and C_{33}, we can use eq. 68 to obtain C_{13}.

4.6 Anisotropy in the Bulk Modulus

Considering the wurtzite structure of ice, with different lattice parameters along different directions as explained above, the bulk modulus of ice is expected to be different with respect to the compressions along the x-y plane and z-axis. Therefore, components of strain tensor are different for displacements along different directions. This anisotropic directionality of the bulk modulus can be compared to the overall isotropic bulk modulus.

In order to calculate the isotropic bulk modulus, B, as explained in eq. 53, we change both lattice parameters by 0.15%, and obtain the curvature of volume dependence of the energy. In addition to the isotropic bulk modulus, we calculate the anisotropic contributions to strain tensor:

i) $(C_{11}+C_{12})/2$ by keeping the lattice parameter c constant while changing the lattice parameter a by 0.15%. This shows how the bulk modulus changes along x-y plane, as given in eq. 63

ii) C_{33} component of the strain tensor, by keeping the lattice parameter a constant while changing the lattice parameter c by 0.15%. Similarly, this shows how the bulk modulus changes along z-axis, as given in eq. 64.

iii) C_{13} component of the bulk modulus using the relation between the isotropic bulk modulus and other obtained components by using eq. 68.

Table 7: The classical bulk modulus and the related components of the strain tensor given in units of GPa. Experimental results are extrapolated to T=0K from eq.4 of Ref [13]. ^{e} is the experimental result from the reference, and ^{c} is the calculated result using eq. 68.

FF/XC	Ice	B_0	$(C_{11}+C_{12})/2$	C_{33}	C_{13}
TTM3-F	Ih	13.74	15.04	20.29	10.82
TTM3-F	aXI	14.13	14.75	20.36	12.17
TTM3-F	XI	14.24	14.39	20.83	13.25
PBE	Ih	14.24	17.41	27.12	7.85
PBE	aXI	14.31	17.52	26.85	7.97
PBE	XI	14.27	17.37	26.28	8.17
vdW-DF$^{\mathrm{PBE}}$	Ih	13.52	15.69	21.92	9.25
vdW-DF$^{\mathrm{PBE}}$	aXI	14.05	16.16	20.77	10.29
vdW-DF$^{\mathrm{PBE}}$	XI	14.32	16.13	22.07	10.58
Expt [13]	Ih	8.48	10.31	14.76	5.63^e
Expt [13]	Ih	8.48	10.31	14.76	5.09^c

In addition, we check eq. 68 against the experimental data of Ref [13] and in the last two rows of Table 7. Using experimental values of B_0, $(C_{11}+C_{12})/2$, and C_{33}, we have calculated C_{13}, and the calculated result compares well with the experiment, considering the dispersion both in the experimental and theoretical results.

As we have mentioned before, there is dispersion in experimental results of the bulk modulus of proton disordered ice Ih and very few of them comment on the anisotropic contributions [4]. The experimental results we present [13] in Table 7 lie on the lower end of this dispersion when the isotropic bulk modulus is compared. However, they still give a qualitative intuition about the order of magnitude of different components of the strain tensor.

Comparing our calculations of the anisotropic bulk modulus along different directions shows that the bulk modulus along the xy-plane, the average of C_{11} and C_{12} is smaller than along z-axis, C_{33}. Therefore, hexagonal ice is softer along the x-y plane than along z-axis.

Furthermore, there are no bulk modulus experiments of proton ordered ice XI, which makes it difficult to comment on structural differences of ice XI and ice Ih. Focusing on the structural differences between the ferroelectric proton ordered ice XI and proton disordered ice Ih, all components of the bulk modulus are similar when a semi-local PBE approximation is considered. Both the isotropic and anisotropic bulk modulus of ice XI is clearly

larger than bulk modulus of ice Ih, when non-local vdW forces are considered via the vdW-DF$^{\mathrm{PBE}}$ functional. This predicts that proton disordered ice Ih is softer than proton ordered ice XI. Both DFT results are consistent with the corresponding lattice parameter calculations. However, there is an inconsistency between lattice parameter and bulk modulus calculations with the TTM3-F force field model, and there is no net trend between different components of the strain tensor. With the TTM3-F force field model, bulk modulus of ice XI is larger than that of ice Ih, and the volume of ice XI is also larger than ice Ih, while it is expected to be the opposite. Therefore, the vdW-DF$^{\mathrm{PBE}}$ functional gives more reasonable bulk modulus results.

4.7 Nuclear Quantum Effects in Isotropic Bulk Modulus

In addition to classical bulk modulus, we can also estimate the contributions from nuclear quantum zero point effects from the curvature of free energy calculations of eq. 43. For this estimation, we have performed a careful analysis of the phonon density of states and corresponding Grüneisen parameters, γ_k, of both phases, as described in eq. 45. The results of the phonon density of states and corresponding Grüneisen parameters have already been shown in Fig. 9 in the previous chapter. Correct estimation of Grüneisen parameter plays a crucial role, because the average value $\langle \omega_k \gamma_k \rangle$ determines whether a system has normal or anomalous isotope effect. Negative γ_k's imply a softening of the modes with decreasing volume, favouring a larger bulk modulus for a lighter isotope. With the normal isotope effect, the bulk modulus of the heavier isotope is larger, whereas with the anomalous isotope effect, the bulk modulus of the lighter isotope is larger.

After this analysis of Grüneisen constants, the curvature of the free energy is calculated to find the bulk modulus of the system, using the eq. 43. The results of the bulk modulus calculations at $T = 0$ K are given in Table. 8 and the temperature dependence of the bulk modulus is given in Fig. 16 for the vdW-DF$^{\mathrm{PBE}}$ functional with the k-point sampling over the Brillouin zone of proton ordered ice XI.

For DFT calculations, this analysis reproduces the anomalous effect on the isotopes of hydrogen atoms, i.e the bulk modulus of H_2O is larger than the bulk modulus of D_2O. However, the bulk modulus of the oxygen isotopes show a normal effect, i.e the bulk modulus of H_2O is smaller than the bulk

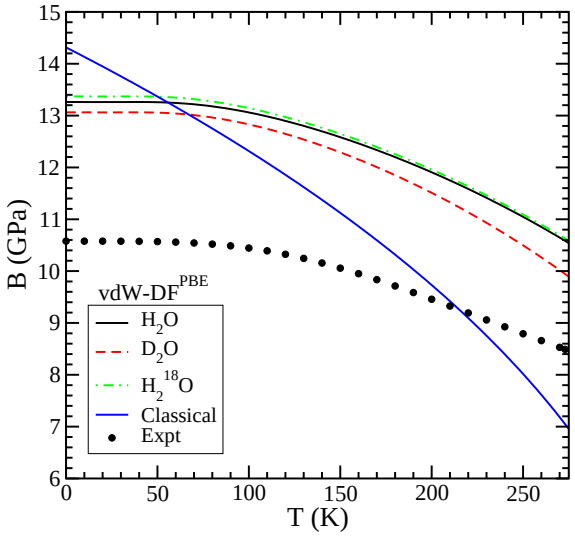

Figure 16: Bulk modulus as a function of temperature calculated with quasi-harmonic approximation for vdW-DF$^{\mathrm{PBE}}$ functional with k-point sampling over the Brillouin zone of proton ordered ice XI. The experimental results are taken from Ref. [4].

modulus of $H_2{}^{18}O$. This behaviour is reproduced qualitatively for both DFT functionals. Comparing our results with previous DFT plane wave studies [73], we see that our PBE calculations perform quite similarly. However, the plane wave calculations that include van der Waals forces with the vdW-DF2 functional [84] do not reproduce the anomalous isotope shift. Therefore, vdW-DF$^{\mathrm{PBE}}$ is still a better candidate for this type of analysis. This is in agreement with our vdW-DF2 results predicting normal isotope effect in volume, as seen in Table 2 of Chapter 3. These results clearly reveal that there is still room for improvement of van der Waals forces representation with the density functionals.

On the other hand, the TTM3-F force field model does not correctly predict the anomalous isotope effect at low temperatures. With this model, there is a crossing from normal to anomalous isotope effect at $\sim$ 270 K, close to the melting temperature, where the low frequency modes with positive Grüneisen parameter become classical and high frequency modes with negative Grüneisen parameter dominate with the quantum effects [71].

As the temperature increases, the bulk modulus of all systems decrease. The convergence to the classical bulk modulus occurs at the temperatures

Table 8: The bulk modulus including the quantum zero point effects given in units of GPa.

FF/XC	Ice	B_0	H_2O	D_2O	$H_2{}^{18}O$	IS(H-D)	IS(^{16}O-^{18}O)
TTM3-F	Ih	13.74	12.81	12.85	12.86	−0.31%	−0.39%
TTM3-F	aXI	14.13	13.03	13.08	13.09	−0.38%	−0.46%
TTM3-F	XI	14.24	13.04	13.09	13.10	−0.38%	−0.46%
PBE	Ih	14.24	14.18	13.44	14.33	+5.22%	−1.06%
PBE	aXI	14.31	13.79	13.15	13.95	+4.63%	−1.17%
PBE	XI	14.27	13.70	13.18	13.84	+3.80%	−1.02%
vdW-DF$^{\mathrm{PBE}}$	Ih	13.52	13.45	13.43	13.46	+0.15%	−0.07%
vdW-DF$^{\mathrm{PBE}}$	aXI	14.05	13.36	13.23	13.43	+1.00%	−0.53%
vdW-DF$^{\mathrm{PBE}}$	XI	14.32	13.26	13.06	13.37	+1.51%	−2.37%
Expt. [69, 74]	Ih		12.1				
Expt. [13]	Ih		8.48				
Expt. [2, 4]	Ih		10.9				
PBE [73]	XI	14.60	14.43	14.09		+2.35%	
vdW-DF2 [73]	XI	12.59	11.59	11.60		−0.09%	

much higher than the melting temperature of ice. This is an indication that the nuclear quantum effects are still important in the liquid phase water and must be considered for correct structural analysis.

4.8 Conclusion

We have shown that there is a clear need for a better and more accurate understanding of the bulk modulus of hexagonal ices. There is dispersion in experimental data of the isotropic bulk modulus, and very few experiments actually focus on the anisotropy in hexagonal ice. We have developed a fast and accurate computational method to obtain the optimal lattice parameters, and the volume dependence of the electronic Kohn-Sham energy, which is important for accurate bulk modulus calculations and will be even more important in the next chapter. The relationship between the strain tensor and the bulk modulus is used to calculate the anisotropic contributions to the overall bulk modulus. It is shown that the compressibility of the system is smaller along the $\hat{z}$-axis than x-y plane. Finally, the nuclear quantum effects on the isotropic bulk modulus are calculated using the QHA method. As expected, there is an anomalous isotope effect in the bulk modulus of

hexagonal ice. When H is replaced with D, the bulk modulus of the heavy ice is smaller than that of light ice. Similar to the isotope effect on the volume, the isotope effect is normal when ^{16}O is replaced by ^{18}O.

Now that we have a detailed analysis of the structure of proton ordered and disordered phases, we can also use our methodology to investigate the transitions between these phases.

5 Phase Transition from proton disordered Ice Ih to proton ordered Ice XI

From theoretical standpoint, the structure of proton ordered phase and existence of order-disorder phase transition have been studied extensively. However, the debate about the most stable phase of ice is not yet settled [79]. Simulation models based on experimental data cannot estimate the small differences between different proton orderings. Predicted stable phase of ice by empirical force field models depends strongly on the parametrization of the boundary conditions, electrostatic multipoles, and treatment of long range interactions. [79, 80, 85–89]. According to Ref. [79], TIP4P-FQ [90] model predicts proton disordered phase as the stable phase, while SPC/E [91], TIP4P [92], TIP5P-E [93] and NvdE [88] models predict proton ordered phases at low temperature limit.

There is also a debate on the structure of the proton ordered phase. As explained in the previous chapters, the experimental structure of proton ordered ice XI is such that hydrogen atoms are ordered with a net dipole moment along the $\hat{z}$-axis. This is called the ferroelectric ordered phase. From the models studied in Ref. [79], only NvdE model predicts ferroelectric ordered phase as the lowest energy phase, in agreement with the experiments. The rest of the mentioned models, predict the ordered phase with an antiferroelectric ordering, where hydrogen atoms are ordered with opposite dipole moments along different planes, with no net dipole moment along $\hat{z}$-axis. Furthermore, according to Ref. [80], SPC [94] , TIPS2 [95] , BSV-pol [96] , RWK2 [97, 98] and KW-pol [99] models predict that disordered configuration has lower energy than ferroelectric ordered phase. Modifying polarisability of KW-pol model (MKW-pol model), they obtained a potential energy surface where ferroelectric ordering has lower energy than disordered configurations [80]. Therefore, it is worth testing a polarisable force field model, TTM3-F to check if it will correctly predict that proton disordered phase has larger energy than proton ordered phase at low temperatures. Experiments with neutron diffraction [76–78], as well as experiments performed under an electric field [75] confirm that the low energy structure at low temperatures has ferroelectric ordering. Consequently, our goal is investigate the order-disorder transition of different isotopic configurations of ferroelectric ordered ice XI, antiferroelectric ordered ice aXI, and disordered ice Ih, from an *ab initio* perspective.

The effect of proton disorder on hexagonal ice structure has also been studied before using *ab initio* density functional theory (DFT). It has been shown that DFT calculations correctly reproduce lattice structure of ice XI [100], and cohesive energy of ice XI is larger than ice Ih [81, 82]. A DFT based Monte Carlo study, where DFT calculations of Hydrogen bond configuration energies are used to parametrize a model to perform Monte Carlo simulations, predicted ice XI as the most stable phase with a phase transition temperature at 98 K. [101, 102] Another recent DFT based Monte Carlo study of dielectric properties of ice, predicted the Curie temperature of the order-disorder phase transition to be around 70-80K [103]. The advantage of DFT based Monte Carlo simulations is that they can parse configurational entropy of the free energy surface in quite detail. However, none of these calculations include the zero point nuclear quantum effects, and investigate the transition temperature difference between different isotopes.

In the previous chapters, we have shown that *ab initio* DFT is essential to observe the correct behaviour of isotope effect in hexagonal ices and QHA with inclusion of van der Waals forces correctly predicts the anomalous isotope effect. Within the framework of quasi-harmonic approximation, we can obtain temperature and volume dependence of free energy. This is an important advantage in predicting the most stable phase not only at zero temperature limit, but also in a range of temperatures. We have also presented that a polarisable and flexible force field model, TTM3-F, predicts an anomalous isotope effect at high temperatures. Although it does not perform well at low temperatures, this is the only water model that shows an improvement on the prediction of the isotope effect, which makes it a good candidate to compare with the *ab initio* DFT results.

In this chapter, we use the quasiharmonic approximation to study how nuclear quantum effects change the phase transition temperature of ices with different isotopic configurations. In this chapter, we extend our study of nuclear quantum effects to analyse the contribution to order-disorder phase transition by using both *ab initio* DFT functionals and TTM3-F force field model. We again analyse the importance of van der Waals forces by comparing a generalized gradient approximated functional, PBE to a van der Waals functional, vdW-DF$^{\mathrm{PBE}}$. We obtain temperature dependence of free energy for both ice phases using the quasi-harmonic approximation and we compare the phase transition temperature of different isotopes.

5.1 Cohesive Energy

In order to understand the phase transition between proton ordered ice XI and proton disordered ice Ih, we have calculated the cohesive energy from eq.s 51 and 52. This is a good test to determine whether TTM3-F force field model or DFT can predict ice XI as the stable phase at the zero temperature limit correctly. We also consider how the cohesive energy changes when the zero point nuclear effects are added to the electronic energy, and the results are given in Table 9.

Table 9: The classical and quantum cohesive energy, E_c (meV) including the zero point effects.

FF/XC	Ice	E_c^0	H_2O	D_2O	$H_2{}^{18}O$
TTM3-F	Ih	601.07±0.22	521.17±0.22	536.24±0.22	522.87±0.23
TTM3-F	aXI	600.30	520.33	535.41	522.04
TTM3-F	XI	599.71	520.11	535.11	521.81
PBE	Ih	620.44	502.07	526.70	504.15
PBE	aXI	626.21	507.17	531.95	509.25
PBE	XI	629.06	509.02	534.07	511.11
vdW-DF$^{\mathrm{PBE}}$	Ih	723.94	601.64	627.65	603.64
vdW-DF$^{\mathrm{PBE}}$	aXI	725.53	602.58	628.80	604.57
vdW-DF$^{\mathrm{PBE}}$	XI	728.75	605.18	631.52	607.18

It is important to note that there is more than one possible proton disordered configuration in ice Ih. In order to accommodate for different possible proton disordered configurations, we have performed a large cell of 96 molecules in our DFT calculations. Because DFT calculations are computationally expensive, we cannot perform more than one of these structures; however, with the force field models it is computationally possible to do these calculations for multiple configurations. Therefore, we have performed all calculations with 5 different 96 molecule configurations of ice Ih with TTM3-F force field model. These results are incorporated in the cohesive energy results of TTM3-F model, given in Table 9. The dispersion in energy due to the residual entropy of hydrogen disorder is on the order of 0.22 meV, which makes it clear that our quantitative prediction of the most stable phase is within this dispersion. This also shows the dispersion in the free energy values and gives an error estimation for F(T) calculations. The difference in

cohesive energy between the ordered and disordered systems are in agreement with the free energy results at $T = 0$K.

Let us first concentrate on the proton disordered ice Ih and ferroelectric ordered ice XI. For both functionals, proton ordered ice XI is more stable than the disordered ice Ih with DFT calculations, while TTM3-F force field model predicts proton disordered ice Ih as the stable phase. When we want to put antiferroelectric ordered ice aXI into perspective of the energies of ferroelectric ordered ice XI and proton disordered ice Ih, we realize that aXI energy is in between ice Ih and ice XI. However, TTM3-F predicts the stability order to be Ih $\rightarrow$ aXI $\rightarrow$ XI, from high cohesive structure to low cohesive, which disagrees with the experiments. Furthermore, considering the error in the cohesive energy, it is impossible to exactly predict the correct stable phase at the zero temperature limit with this model. On the other hand, both DFT functionals predict the stability order to be XI $\rightarrow$ aXI $\rightarrow$ Ih, agreeing with the experiments that the most stable phase is the ferroelectric ordered phase.

5.2 Transition Temperature

In order to analyse the proton order to disorder phase transition temperature, we study the Helmholtz Free energy at zero pressure. First, we evaluate volume dependence of free energy, F(V) at a fixed temperature. Then we calculate value of free energy minimum, $F(V_0)$ for each temperature. Therefore we obtain the temperature dependence of free energy, by evaluating free energy minimum for each temperature, $F(V_0(T))$, as in eq.s 43, 44.

We first concentrate on the classical limit of the free energy, without considering the nuclear quantum effects, as given in eq. 44. Consistent with previously reported results, DFT predicts a phase transition in this limit, regardless of the chosen functional. In addition, both semi-local PBE and non-local vdW-DF$^{\mathrm{PBE}}$ functional overestimates the phase transition temperature, when nuclear quantum effects are not included in the calculations. On the other hand, TTM3-F force field model does not correctly predict the stable phase in the low temperature limit and the difference between the free energies of the two phases increases with temperature. Therefore, it does not show a phase transition, as shown in the first column of Table 10.

However, we need to consider the nuclear zero point effects to compare the predicted phase transition temperature to the experiments. Fig. 17 shows the temperature dependence of the free energy with zero point effects

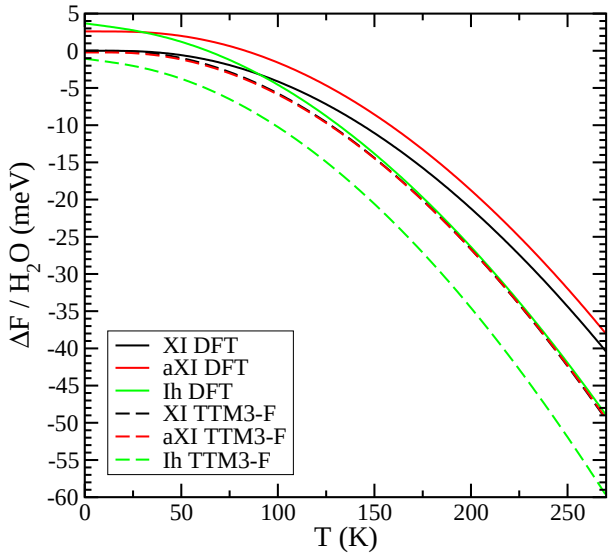

Figure 17: Relative free energy per molecule including the quantum zero point effects as a function of temperature. The lines show DFT results with the vdW-DF$^{\rm PBE}$ functional and the dotted lines are the results with TTM3-F model.

Table 10: The classical and quantum proton order to disorder transition temperature, T_c (K) including zero point effects for ice Ih-ice XI and ice Ih to ice aXI.

Ice	Method	T_c^0	H_2O	D_2O	$H_2{}^{18}O$
aXI	PBE	153	151	156	151
aXI	vdW-DF$^{\rm PBE}$	42	30	35	30
XI	PBE	221	202	215	203
XI	vdW-DF$^{\rm PBE}$	105	91	97	90
XI	Expt [52, 53]		72	76	

for H_2O. For low temperatures, TTM3-F model predicts ice Ih as the stable phase with ~ 1 meV energy difference from ice XI at zero temperature; and a divergence of energy at higher temperatures, making the prediction correct for high temperatures only. DFT correctly predicts the most stable phase as ice XI for low temperatures, with an energy difference of ~ 4.5 meV. As the temperature increases, there is a crossing at $T = 91$ K and ice Ih becomes the stable phase beyond this temperature for H_2O.

Inclusion of zero point effects also allows us to obtain the isotope effect in the phase transition temperature, since it is experimentally known that the order-disorder transition temperature of heavy ice (D_2O) is larger than light ice (H_2O) by 4K [52, 53]. Table 10 shows that we already observe the phase transition with the classical electronic energy calculations for both PBE and vdW-DF$^{\mathrm{PBE}}$ approximations, but this temperature decreases with the inclusion of zero-point effects. The vdW-DF$^{\mathrm{PBE}}$ results are below the glassy transitions where proton mobility diminishes around 100-110 K [104, 105] and in general agreement with the experimental order-disorder phase transition temperatures; whereas the PBE results are even above the glassy transitions. Although semi-local PBE functional gives a correct prediction of the stable phase, phase transition temperature is much larger than the experimental range. In agreement with the experimental 4K difference in the phase transition temperature of the isotopes, the vdW-DF$^{\mathrm{PBE}}$ functional predicted transition temperature of D_2O ice is larger than the light ice with 6 K difference. Therefore, it is important to note that inclusion of non-local van der Waals forces is critical for a reasonable prediction of the transition temperature.

5.3 Contribution from Each Term of QHA to Total Free Energy

5.3.1 Classical Free Energy

Let us now have a look at the classical limit of free energy to analyse the phase transition without zero-point effects, eq. 44. To understand how each component of eq. 44 contributes to the total free energy, we present in Fig. 18c, the temperature dependence of $E_0(V_0(T))$, and $-TS$ terms separately, in addition to the full temperature dependence of the classical free energy.

Different than the quantum free energy, we see an overall increase in the classical limit of the free energy, Fig. 18a. Therefore, it is worth looking into each component of the classical limit separately, from the equilibrium volume of classical free energy, $V_0^{F_0}$, for each temperature.

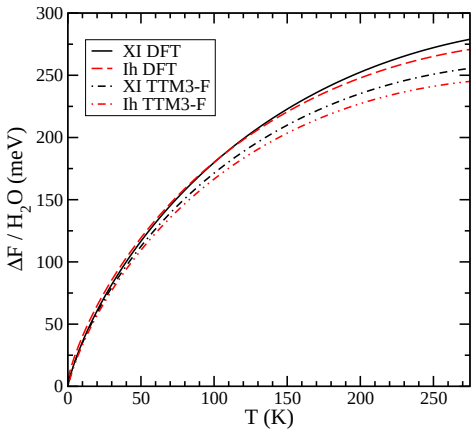

(a) Classical free energy with the vdW-DF$^{\mathrm{PBE}}$ functional and TTM3-F model.

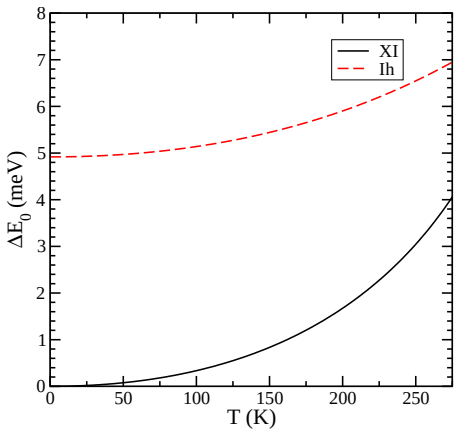

(b) Kohn-Sham energy contribution to the classical free energy.

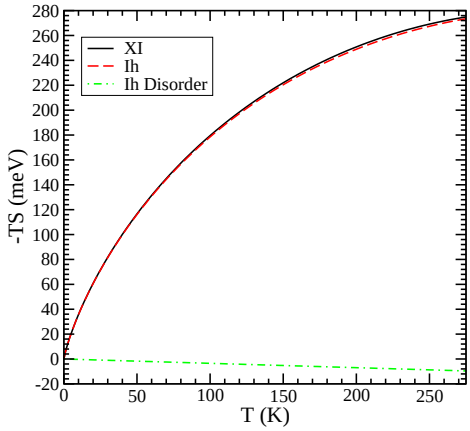

(c) Entropy related contribution to the classical free energy.

Figure 18: Contribution to the classical free energy from each term of eq. 44 calculated with the vdW-DF$^{\mathrm{PBE}}$ functional, with respect to ice XI energies.

The Kohn-Sham energy contribution to the classical free energy, $E_0(V_0^{F_0}(T))$ is increasing with the increasing temperature, similar to the quantum limit, as shown in Fig. 18b.

Since we do not have any zero point energy contribution, the only other contribution to the free energy comes from the classical limit of the entropy term. We again calculate the entropy contribution for a series of volumes and do a second order fit to obtain the full temperature dependence, $-TS = k_B T \ln\left(\frac{\hbar\omega_k(V_0^{F_0}(T))}{k_B T}\right)$.

We see that both parts of the classical free energy increases with the temperature, but the main contribution comes from the classical Kohn-Sham energy, which also plays the key role in determining the stable phase.

5.3.2 Free Energy with Zero Point Effects

In addition to the exact values, given in Fig. 19, we also present the difference between the energies of ice Ih and ice XI for H_2O and D_2O separately, in Fig. 20.

The temperature dependence of the Kohn-Sham energy is obtained by first calculating the equilibrium volume of the free energy, V_0 and then calculating the Kohn-Sham energy at that volume for each temperature: $E_0(V_0(T))$. As shown in Fig 19b and 20b this component of the energy increases with the temperature and the slopes of the increase of proton disordered ice Ih is smaller than proton ordered ice XI.

To analyse the temperature dependence of the phonon modes separately, we first calculate zero point vibrations for a series of volumes within the quasi-harmonic approximation (QHA) and do a linear fit. Then we calculate the zero point energy contribution to the free energy, from this fit.

$$E_{\mathrm{ZP}} = \sum_k \frac{\hbar\omega_k(V_0(T))}{2} \tag{69}$$

This part of the free energy is slowly decreasing with the temperature, given in Fig. 19c and 20c, but it is not strong enough to overcome the increase from the Kohn-Sham term. But more importantly, the stability of the structures is reversed: Proton ordered ice XI has smaller negative shift from the phonon energies to the electronic Kohn-Sham energy than proton disordered ice Ih.

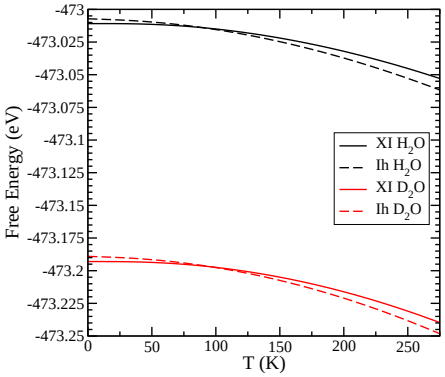

(a) Quantum free energy.

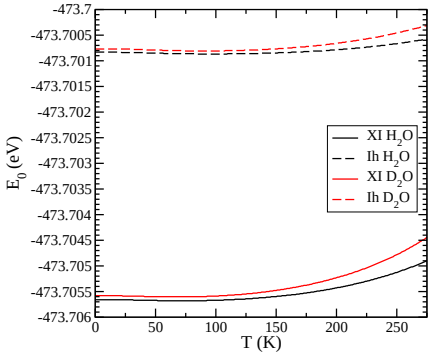

(b) Kohn-Sham energy contribution to free energy.

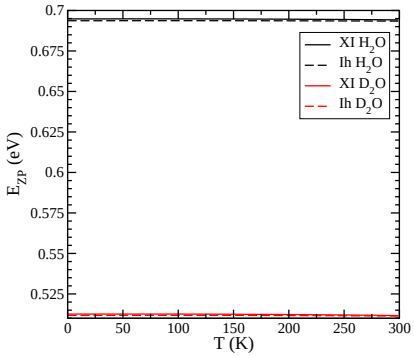

(c) Phonon zero point energy contribution to free energy.

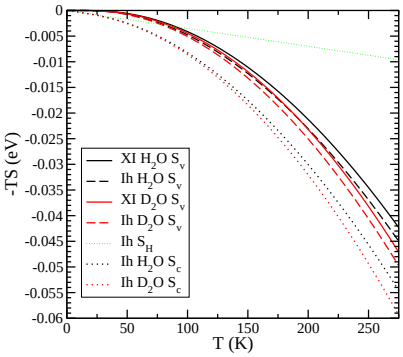

(d) Entropy contribution to free energy.

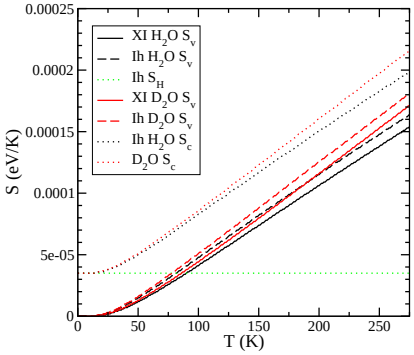

(e) Entropy as a function of temperature.

Figure 19: Contribution to quantum free energy from each term of eq. 43 calculated for H_2O and D_2O, with the vdW-DF^{PBE} functional.

Fig. 20b shows that the electronic energy difference between the two ices is larger for H_2O than D_2O, which would result as a larger transition temperature for H_2O than D_2O, and this is against the expectations from the experimental results. However, when we take the zero-point energies of the two isotopes into account, Fig. 20c shows that the difference between the two ices is smaller for H_2O than D_2O. When this is added to the electronic energy, as in Fig. 20d, it is clear that the transition temperature of H_2O is shifted below the transition temperature of D_2O, which agrees with the experimental results.

Similarly, we calculate the vibrational contribution to the entropy for a series of volumes and make a third order fit to obtain the temperature dependence in the form of

$$-TS_{\mathrm{v}} = \sum_k k_B T \ln\left(1 - e^{-\hbar\omega_k(V_0(T))/k_B T}\right) \tag{70}$$

For the residual entropy due to the Hydrogen disorder in ice Ih, we calculate the Pauling entropy $S_H = Nk_B \ln(3/2)$. [51] Then the total configurational energy for ice Ih is calculated as:

$$-TS_{\mathrm{c}} = -TS_{\mathrm{v}} - TS_H \tag{71}$$

The decrease of the entropy related term as the increase in the temperature, $-TS$, is given in Fig. 20e and 20f. On the other hand, both vibrational and configurational entropy terms work against the expectations, contributing to the free energy for H_2O more than D_2O, but this is small compared to the zero-point contributions.

This part of the free energy combined with the decrease in the zero point energy, overcomes the increase in Kohn-Sham part resulting with a net decrease in the total free energy. Therefore, this is the term that determines the overall temperature dependence of the total free energy.

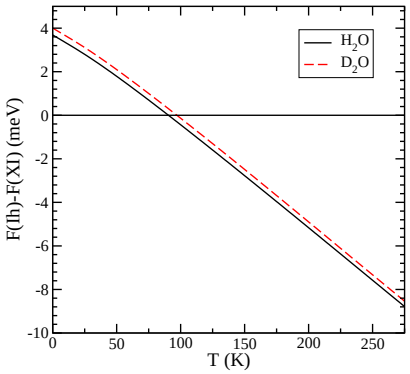

(a) Quantum free energy.

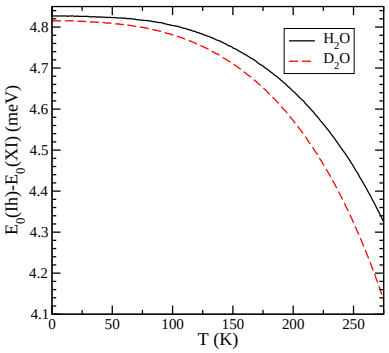

(b) Kohn-Sham energy contribution to free energy.

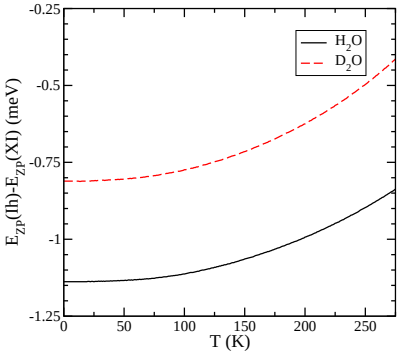

(c) Phonon zero point energy contribution to free energy.

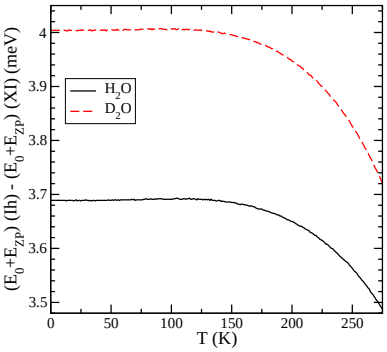

(d) Sum of Kohn-Sham energy and phonon zero point energy contributions to free energy.

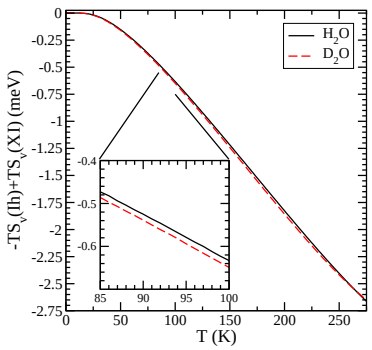

(e) Vibrational entropy contribution to free energy.

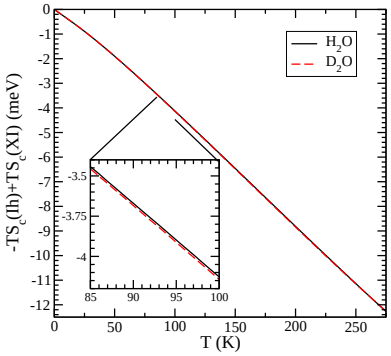

(f) Configurational entropy contribution to free energy.

Figure 20: Difference between proton disordered ice Ih and proton ordered ice XI, for each contribution to quantum free energy from each term of eq. 43 calculated for H_2O and D_2O, with the vdW-DF^{PBE} functional.

Furthermore, when all these energies are added up to the total free energy, Fig. 20a, it is clear that the reason H_2O crosses from positive to negative values at a lower temperature than D_2O, is due to zero-point effects of the phonon modes, while the overall shape of the free energy is determined by fine cancellations between the zero-point and entropic contributions. One of the reasons of the quantitative difference from the experimental results of transition temperature can be as a result of the error in the estimation of residual entropy due to disorder in both systems. The residual entropy at the transition that ice XI loses much but not all of the entropy at T_c [76], but this is more likely due to the existence of domains of ordered ice XI regions occurring around the impurity, and coexisting with disordered ice Ih [106]. Another reason of the quantitative difference can be due to the loss of precision of QHA at larger temperatures, as the temperature dependence of the phonon vibrations is not taken into account. This is also the case in the calculated V_0 with isotope effects; the calculated values deviate from the experimental values at larger temperatures [6].

All in all, QHA within DFT with non-local vdW forces, is predicting a 6K temperature difference between the isotopes, as compared to the experimental 4K difference. This difference is solely due to the nuclear quantum effects from the phonon vibrational energy differences, and it is predicted without invoking tunnelling effects.

5.4 Phonon Density of States

Now that we have shown the main reason behind the difference in the phase transition temperature of different isotopes is zero point energy, let us say a few words to compare phonon density of states of the two ices, before concluding this chapter.

Fig. 21 shows phonon density of states for H_2O for both proton ordered ice XI and proton disordered ice Ih at zero temperature. The colors represent the average Grüneisen parameter of each band separately. We observe a redshift in the low energy phonon modes of proton disordered ice Ih with respect to proton ordered ice XI. Translations are sharpened while librations are softened in ice Ih. On the other hand, there is a blueshift with softening in the symmetric and anti-symmetric stretching modes of ice Ih. Therefore, with proton ordering, we weaken the covalency of the intra-molecular bonds, while strengthening the inter-molecular Hydrogen bonding. This combined with the weights of the Grüneisen parameters results as an overall slightly

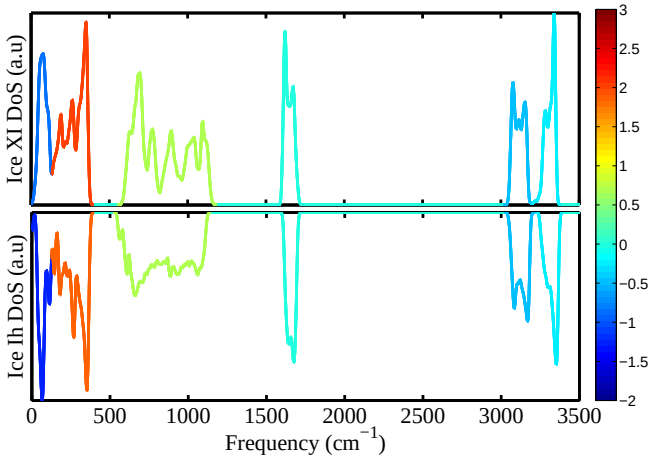

Figure 21: Density of vibrational states for H_2O for proton ordered ice XI and disordered Ih structures, as obtained with the vdW-DF^{PBE} functional. Average Grüneisen constants of the different modes are given in color code.

larger zero point energy for ice XI than ice Ih, as also shown previously in Fig. 20c.

5.5 Conclusion

In this chapter, we have shown that the *ab initio* DFT with van der Waals forces is the only robust functional that predicts the phase transition between proton ordered ice XI and proton disordered ice Ih. Without van der Waals forces, PBE functional correctly predicts that ice XI is the stable phase at low temperatures, but this functional overestimates the phase transition temperature. The antiferroelectric ordered ice aXI has free energy in between ferroelectric ordered ice XI and proton disordered ice Ih. As a result, the transition temperature from ice Ih to ice aXI is smaller than the transition temperature from ice Ih to ice XI. Comparing the vdW-DF^{PBE} functional, to the experiments, the most stable phase at zero temperature limit is ferroelectric proton ordered ice XI, and the phase transition is from ice Ih to ice XI. Force field models need improvement to correctly estimate the stable phases of hexagonal ices at low temperatures. TTM3-F model, cannot predict the low temperature phase as the proton ordered phase, therefore it cannot show the order-disorder phase transition.

We have also investigated how nuclear quantum effects are changing the

phase transition temperature. The vdW-DF$^{\mathrm{PBE}}$ functional is also a good candidate to look into the phase transition temperature difference of different isotopes. Although the transition temperature is larger than the experimental values, with 91 K for H_2O and 97 K for D_2O, the temperature difference between H_2O and D_2O is 6 K with this functional, in agreement with the experimental 4 K difference. We made a detailed analysis of the contribution of each term in QHA to the total Helmholtz free energy, and concluded that this temperature difference of different isotopes is only due to the difference in the zero point energy of different ices, and nuclear quantum effects play a crucial role in this phase transition.

6 Zero Point Effects in Other Ice Phases and Ice-like Structures

We have shown that *ab initio* density functional theory within quasi-harmonic approximation, is correctly predicting the isotope effect in hexagonal ices, ice Ih and ice XI. Experimental results show that this anomalous isotope effect of the replacement of H with D, also persists in liquid water, [1, 18] although the structure of the liquid is very different that ice. Even though there is still a hydrogen bond network, the molecules are not ordered as in hexagonal ice, meaning that there is no defined underlying lattice structure. Furthermore, there is a debate about the structure of liquid water, especially in the super-cooled regime. One of the theories is that there is a mixture of high density liquid and low density liquid phases, as it was introduced at the beginning of this thesis. Therefore, analysing nuclear quantum effects in liquid water is not straightforward.

In order to understand how the isotope effect changes with the density and Hbond distance, we have looked at several different phases of ice under different pressure regimes. By analysing how the isotope effect magnitude and sign (normal vs. anomalous) changes with different structures with different bond lengths, we can make links to the effects in liquid water. For this purpose, we have looked at cubic ice Ic, clathrate hydrate structure I, high density ices: ice IX, ice II, and ice VIII, and the amorphous ices with different densities. Each of these structures and the resulting phonon density of states, Grüneisen parameters, and the isotope effects will be detailed in this chapter.

6.1 Cubic Ice Ic

6.1.1 Structure

Cubic ice Ic is a metastable phase with a structure similar to hexagonal ice. Oxygen atoms of ice Ic are arranged in cubic structure of diamond. The relationship between the hexagonal ice and the cubic ice is defined by different stacking orders: ice Ih is stacked in a sequence of ABABAB while ice Ic is stacked in a sequence of ABCABC. There are also studies on the formation of ice with a mixture of ice Ih and ice Ic, with stacking disorders. However, the standard formation of ice Ic is obtained when the temperature of the

amorphous ice is increased above $\sim$ 130 K [107]. In addition, supercooled water crystallises to ice Ic upon cooling [108]. Ice Ic also forms when high pressure phases from ice II to ice IX are recovered in liquid nitrogen and heated [109, 110]. Therefore, there is no sharp phase transition between ice Ic and ice Ih.

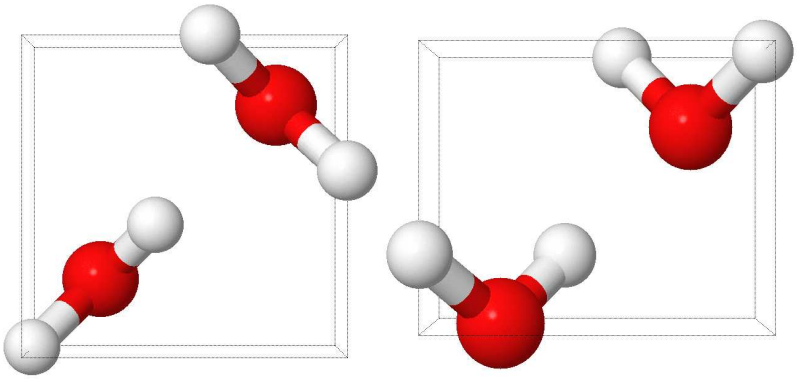

Figure 22: Cubic ice Ic structure. The image on the left is the top view of the x-y plane; the image on the right is the side view of the x-z plane.

We are only interested in understanding the isotope effect with changing density, and therefore the stacking disorder between ice Ic and ice Ih is beyond the scope of this thesis. Furthermore, we have shown that the isotope effect remains anomalous regardless of the proton ordering of the system. Hence, in this section, we will analyse only proton ordered ice Ic, which has a diamond lattice structure; i.e face centred cubic structure with 2 molecules in the unit cell, as shown in Fig. 22.

6.1.2 Computational Details

All structural relaxations are performed with tζ+p atomic orbital basis set initially, using a real-space mesh cutoff of 600 Ry for the real space integrals, electronic k-grid Monkhorst Pack of $6\times6\times6$ (corresponding to 132 k-points) for unit cell calculations, force tolerance of 0.001 eV/Å and a density matrix tolerance of 10^{-5} electrons. For the volume dependency of Kohn-Sham energy, the electronic energy of these relaxed configurations are recalculated using qζ+dp atomic orbital basis sets.

All the force constants calculations are performed with tζ+p basis sets. We used an atomic displacement Δx=0.06 Å for the frozen phonon calcula-

tion. The rest of the methodology follows from the previous chapters. The phonon frequencies, $\omega_k(V_0)$ and Grüneisen parameters $\gamma_k(V_0)$ are obtained by diagonalizing the dynamical matrix, computed by finite differences from the atomic forces in a $(3 \times 3 \times 3)$ supercell, at volumes slightly below and above V_0. The Grüneisen parameters are calculated for 3 volumes for k-point sampling and the phonon modes are calculated by diving Brillouin zone to a grid of $9 \times 9 \times 9$, with equal weights on each mode.

6.1.3 Results

6.1.3.1 Phonon Density of States and Grüneisen Parameters

First, we compare the phonon density of states projected on hydrogen and oxygen atoms for ice Ic, given in Fig. 23, with ice XI from previous calculations of Fig. 9. We also present the Grüneisen parameter of each mode, depicted by the black points in the lower panel, and the average Grüneisen parameter of each band, with a red line, in Fig. 23.

The grouping of the density of states is very similar for both structures. Very low frequency modes corresponding to stretching modes of Hydrogen bonds (~ 66 cm^{-1}) have negative γ_k, meaning that this structure also shows negative thermal expansion at low temperatures, similar to ice Ih. Bending modes (~ 1639 cm^{-1}) have an average γ_k at around zero and therefore these modes do not contribute to the isotope effect.

Translations (~ 272 cm^{-1}) and librations (~ 826 cm^{-1}) are defined by the changes in the Hbond, and they have positive γ_k. The high frequency antisymmetric (~ 3283 cm^{-1}) and symmetric (~ 3089 cm^{-1}) stretching modes, dominated by H atoms, have negative Grüneisen parameter. The inter-molecular Hbonding and intra-molecular OH covalent bonding of ice Ic is very similar to ice Ih. Therefore, the bonding of anticorrelation of these anharmonicities also exist for this system.

6.1.3.2 Isotope Effects on Volume and Bulk Modulus

As expected from the distribution of Grüneisen parameters with the phonon density of states, ice Ic presents a large anomalous isotope effect in the volume. The volume of heavy, D_2O ice Ic is 0.16% larger than normal ice Ic at $T = 0$ K, as presented in Table 11. Similar to hexagonal ices, the isotope effect is normal when ^{16}O is replaced by ^{18}O, and the volume decreases by 0.13%.

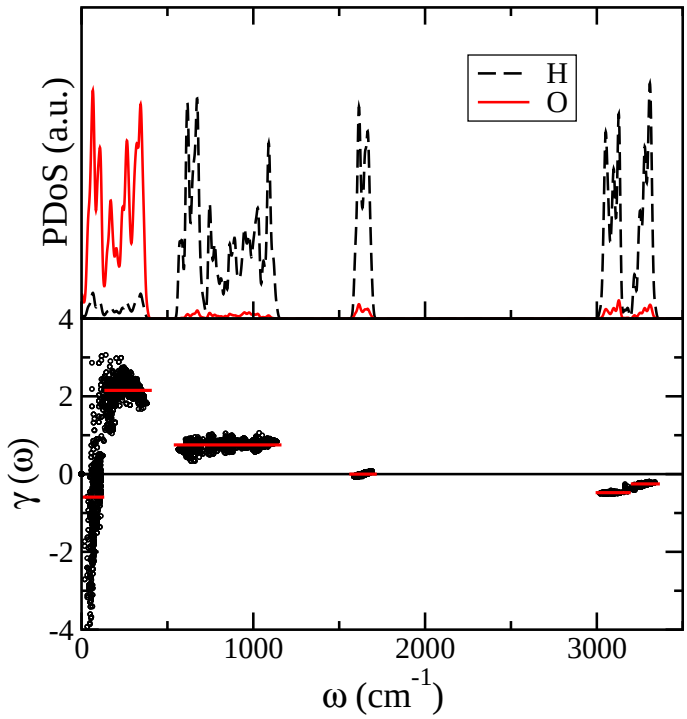

Figure 23: Top: Phonon density of states projected on H and O for ice Ic. Bottom: Corresponding Grüneisen parameters, γ_k (black dots), and the average Grüneisen parameter of each band (red lines).

Fig. 24a shows the temperature dependence of volume for different isotopes for ice Ic. Similar to hexagonal ices, there is a negative thermal expansion in ice Ic at $\sim$ 60 K, as obtained with the vdW-DF$^{\mathrm{PBE}}$ functional. The anomalous isotope effect increases with temperature, as the volumes of H_2O and D_2O get separated from each other, while the normal isotope effect decreases as the volumes of H_2O and $H_2{}^{18}O$ converge close to the melting point.

The isotope effect on the bulk modulus is similar to the isotope effect on the volume of ice Ic, as shown in the second part of Table 11 and presented in Fig. 24. The difference between the bulk modulus of H_2O and D_2O increases with temperature on the anomalous side, while bulk modulus of H_2O and $H_2{}^{18}O$ remain normal at all temperatures.

In summary, we have shown that the bonding of ice Ic is very similar to ice Ih, with similar phonon density of states, and Grüneisen parameters.

Table 11: Top: Frozen lattice parameter, classical volume, and isotope dependent volumes. Bottom: Classical and isotope dependent bulk modulus at $T = 0$ K. Distances are given in Å, volumes in Å^3, and bulk modulus in GPa.

XC	a	V_0	H_2O	D_2O	$H_2{}^{18}O$	IS(H-D)	IS(^{16}O -^{18}O)
PBE	6.25	30.47	30.87	30.99	30.83	−0.39%	+0.13%
vdW-DF$^{\text{PBE}}$	6.29	31.14	31.60	31.65	31.56	−0.16%	+0.13%
Expt. [111]	6.358		32.127				
XC		B_0	H_2O	D_2O	$H_2{}^{18}O$	IS(H-D)	IS(^{16}O -^{18}O)
PBE		14.24	12.74	12.32	12.92	+3.30%	−1.41%
vdW-DF$^{\text{PBE}}$		14.47	13.24	13.10	13.34	+1.02%	−0.81%

This results with an anomalous isotope effect on the volume and bulk modulus with increasing temperatures, for hydrogen isotopes, and normal isotope effect for oxygen isotopes, similar in both ice Ih and ice Ic.

6.2 Clathrate Hydrate Structure I

Gas hydrates, also known as clathrates are crystalline structures composed of cages of water molecule networks holding hosts of hydrocarbons and other molecules in their cavities [112, 113]. Clathrates are found in permafrost and continental margins under high pressures [114] and they are quite important for many practical reasons. They have a potential as a fuel resource, both as deposits of hydrocarbons with much larger reserves than oil or natural gas [113, 115] and also as a potential usage for H_2 storage [116]. Furthermore, they also can provide a possible solution to capture and store the excess atomospheric carbon [117]. However, besides the host of interesting applications they offer, they can also be a nuisance as they are known to clog the subsea gas pipelines and cause economical and ecological risks [115]. Therefore, it is quite important to understand the structural properties of the clathrates in detail.

In clathrates, the hydrogen bonding (Hbond) networks of tetrahedrally coordinated host water molecules are not significantly affected by the interactions of the guest molecules. Therefore, high pressures are required to stabilize these clathrate structures [113, 118]. Clathrates are known to form different structures, such as structure I, structure II, structure H, etc. (for more detail, refer to [112, 113, 118] and references within). In this section,

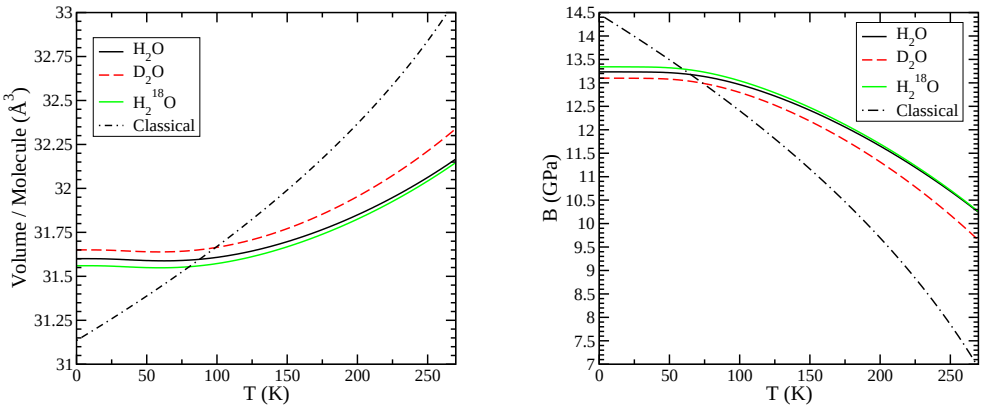

(a) Isotope effect in volume.

(b) Isotope effect in bulk modulus.

Figure 24: Volume per molecule and bulk modulus of ice Ic as a function of temperature for different isotopes calculated using the QHA with the vdW-DF$^{\mathrm{PBE}}$ functional.

we will focus on one of the most common forms, so called Structure I (sI) with CH_4 as the host molecule.

There has been recent theoretical interest in clathrates. There are quite a few *ab initio* density functional theory (DFT) and quantum chemical calculations on clathrates in terms of the structural stability [119–121], methane and hydrogen storage [122, 123], molecular vibrations [124, 125], energetics and kinetics between the host and the guest molecules [126–128]. In addition, the structural properties of clathrates have been investigated using empirical force field molecular dynamics to analyse nucleation and growth mechanisms [129–134] and the energy landscape [135].

However, the zero point effects have not been theoretically analysed for clathrates, until this work. Similar to hexagonal ices, the anomalous isotope effect has been experimentally observed for clathrates [5], where the lattice constant of the heavy hydrogen isotope (D_2O) is larger than that of the normal isotope (H_2O) at a fixed temperature and pressure. In this section, we make a similar analysis to hexagonal ices and we address the problem of understanding nuclear quantum effects in these structures. We investigate the same structure as the experimental clathrate structure I with CH_4 molecules inside the cages. We further compare the empty and filled structures and analyse how the size of empty water cages change in the presence of CH_4 molecules.

6.2.1 Structure

In this section, we study clathrate structure I, which is formed by two 5^{12} cages and six $5^{12}6^2$ cages for a total of 46 H_2O molecules per unit cell with a host of 8 CH_4 molecules. We will perform cohesive energy analysis on two cases of this structure:

(i) Filled sI: H_2O cages of sI with the host of 8 CH_4 molecules.

(ii) Empty sI: Empty H_2O cages of sI without the host CH_4 molecules.

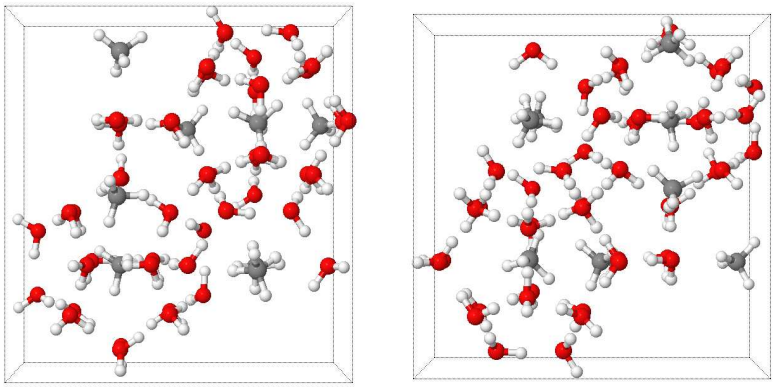

Figure 25: Clathrate hydrate structure I. The image on the left is the top view of the x-y plane; the image on the right is the side view of the x-z plane. Note that this is only a representation of the coordination of the unit cell of the system, and periodic boundary conditions apply during the calculations.

6.2.2 Computational Details

All the calculations are performed with the non-local van der Waals functional, vdW-DF$^{\text{PBE}}$ for exchange and correlation [8, 9, 60]. This functional has been shown, in previous chapters, to perform well for water and ice Ih [6, 9].

The relaxations for calculating the E_0(V) curve are perfomed using a real-space mesh cutoff of 500 Ry for the integrals, electronic k-grid cutoff of 10 Å, force tolerance of 0.005 eV/Å and a density matrix tolerance of 10^{-4} electrons. Instead of doing a variable cell optimization, we calculate the energy for a fixed volume by changing the lattice parameters. The curve

for Kohn-Sham energy as a function of volume is obtained and the classical volume is calculated from the minimum of a third order polynomial fit. The minimum of the energy-volume curve is the frozen volume of the system used in the free energy calculations with the quasi-harmonic approximation.

For the calculations of nuclear quantum effects, the vibrational modes are calculated using the frozen phonon approximation. The force constant calculations are performed with an atomic displacement of $\Delta x = 0.08$ Å.

6.2.3 Results

It is well established that clathrates are metastable structures at zero pressure and temperature. In order to confirm that our calculations agree with this, we have performed a detailed cohesive energy, E^c calculation of sI. We have calculated both classical, E_0^c and quantum, E_{H/D_2O}^c cohesive energy including the nuclear zero point effects. The results are given in Table 12.

Table 12: Classical and isotope dependent cohesive energy of the empty clathrate structure I, given in meV.

E_c^0	H_2O	D_2O	$H_2{}^{18}O$
712.204	595.48	620.23	597.41

Comparing these results to those of hexagonal ice from Table 9, it is clear that the zero point effects are quite important for cohesive energy calculations, because they tend to decrease the cohesive energy of the system in the direction of unstability, both for ice Ih and clathrate sI. In agreement with the experiments, at zero pressure and temperature, clathrate structure I is metastable compared to both proton disordered and proton ordered hexagonal ice.

6.2.3.1 Phonon Density of States and Grüneisen Parameters

In order to understand the zero point quantum effects on this structure, the phonon density of states projected on the oxygen and hydrogen atoms and the corresponding Grüneisen parameters are calculated. For the filled structures, there is a large numerical error in the low frequency modes. As explained in Chapter 3, the negative phonon modes in the low frequency modes are not included in the analysis and in this case, there are quite

a few modes that are thrown away in the filled structure. These are the contributions from the host CH_4 molecules, and they are coupled to the low frequency translational modes of the cage. Therefore, the results from the filled structures do not show the zero point effects from these modes. This is equivalent to removing contributions from CH_4 of filled cages, and provides a fairly good comparison to the empty cages. The main difference between the phonon modes of filled and empty cages is in the sign of the Grüneisen parameter of the low frequency modes. This will only affect the negative thermal expansion prediction at low temperatures and will not affect the sign of the isotope effect as will be shown in the next subsection.

Comparing the results in figures 9 and 26 shows that there is an overall softening of the modes in the clathrate structure compared to ice Ih.

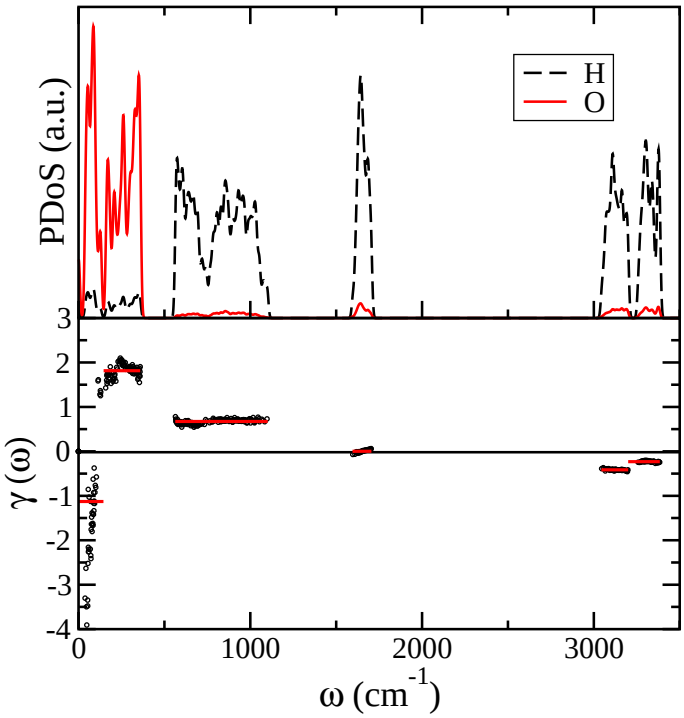

Figure 26: Top: Phonon density of states projected on H and O for the empty clathrate structure I. Bottom: Corresponding Grüneisen parameters, γ_k (black dots), and the average Grüneisen parameter of each band (red lines).

As expected, the anticorrelation between the Hbonds and covalent OH

bonds [6], is still observable in the empty sI, in the projected density of states and the corresponding Grüneisen parameters. If the average Grüneisen parameter of each phonon branch is compared between the empty sI and ice Ih, the clathrate has a smaller positive value for the translational and librational modes. On the other hand, for the symmetric and anti-symmetric stretching modes of the covalent OH bonds, empty structure I has larger negative values than H-ordered ice Ih. In the end, the anticorrelation between the positive and negative Grüneisen parameters with their corresponding frequencies results in an overall anomalous isotope shift in the volume and bulk modulus of H_2O and D_2O, as shown in the next section below.

6.2.3.2 Isotope Effects on Volume and Bulk Modulus

The cell volume per H_2O molecule and the bulk modulus results calculated from the minimum and the curvature of the energy as a function of volume are shown in Table 13. The initial calculations are performed at the free energy curve minimum, therefore at zero pressure.

Both Table 13, and Fig. 27a show one striking difference between the empty and filled structures. The volume per molecule of the empty structure is larger than the volume per molecule of the filled structure at the zero temperature limit. Inclusion of the zero point effects increases the volume, but does not change the fact that inclusion of the host CH_4 molecules decreases the volume of the structure. This continues up to $\sim$ 250 K, and then there is a crossing, where the volume of the filled structure becomes larger than the volume of the empty structures, as shown in Fig. 27a. It should be noted that the QHA does not involve the anharmonic terms on the phonon modes directly due to the temperature, as explained in the theory chapter. Therefore, the divergence of the volume with the temperature does not involve the temperature effects directly, and has larger error with increasing temperature. However, the difference in the volume between the isotopes in all temperature ranges are in good agreement regardless of the host molecules. And the isotopic volume change, IS(H-D) in the Table 13 is very similar for both structures.

Table 13: Top: For clathrate structure I, frozen lattice parameter, classical volume, and isotope dependent volumes. Bottom: Classical and isotope dependent bulk modulus at $T = 0$ K and experimental temperatures and pressures. Volumes are given in Å^3, bulk modulus in GPa, temperature in K, and pressure in bar.

Structure	P	T	V_0	H_2O	D_2O	$H_2{}^{18}O$	IS(H-D)	IS(^{16}O -^{18}O)
Empty	0.00	0	35.53	35.90	35.97	35.86	−0.20%	+0.11%
Empty	0.00	271	37.21	36.20	36.40	36.18	−0.55%	+0.06%
Empty	0.00	273	37.23	36.21	36.41	36.19	−0.55%	+0.06%
Empty	59.41	271	37.17	36.18	36.38	36.16	−0.55%	+0.06%
Empty	59.41	273	37.19	36.19	36.39	36.17	−0.55%	+0.06%
Empty	601.19	271	36.86	35.97	36.15	35.95	−0.50%	+0.06%
Empty	601.19	273	36.88	35.97	36.16	35.95	−0.53%	+0.06%
Filled	0.00	0	34.95	35.45	35.51	35.42	−0.17%	+0.09%
Filled	0.00	271	37.11	36.27	36.46	36.26	−0.52%	+0.03%
Filled	0.00	273	37.13	36.29	36.48	36.27	−0.52%	+0.06%
Filled	59.41	271	37.08	36.25	36.44	36.24	−0.52%	+0.03%
Filled	59.41	273	37.10	36.27	36.45	36.25	−0.50%	+0.06%
Filled	601.19	271	36.83	36.07	36.24	36.05	−0.47%	+0.06%
Filled	601.19	273	36.85	36.08	36.26	36.07	−0.50%	+0.03%
Expt. [5]	59.41	271	–	37.12	–	–	−0.40%	–
Expt. [5]	59.41	273	–	–	37.27	–	−0.40%	–
Expt. [5]	601.19	271	–	36.90	–	–	−0.43%	–
Expt. [5]	601.19	273	–	–	37.06	–	−0.43%	–

Structure	T	P	B_0	H_2O	D_2O	$H_2{}^{18}O$	IS(H-D)	IS(^{16}O -^{18}O)
Empty	0.00	0	11.46	10.56	10.38	10.65	+1.71%	−0.85%
Empty	0.00	271	5.85	8.78	8.24	8.82	+6.15%	−0.46%
Empty	0.00	273	5.79	8.75	8.20	8.79	+6.29%	−0.46%
Empty	600.00	271	6.81	9.39	8.89	9.42	+5.33%	−0.32%
Empty	600.00	273	6.75	9.36	8.86	9.40	+5.34%	−0.43%
Filled	0.00	0	14.55	13.39	13.26	13.47	+0.97%	−0.60%
Filled	0.00	271	7.73	10.31	9.75	10.31	+5.43%	+0.05%
Filled	0.00	273	7.64	10.27	9.70	10.26	+5.55%	+0.05%
Filled	600.00	271	8.49	10.85	10.33	10.85	+4.79%	+0.04%
Filled	600.00	273	8.42	10.81	10.28	10.80	+4.90%	+0.05%
Expt. [5]	600.00	271	–	9.11	–	–	+9.88%	–
Expt. [5]	600.00	273	–	–	8.21	–	+9.88%	–

There is also a difference in the negative thermal expansion of filled and empty clathrate cages. Similar to hexagonal ices, the empty cages show a negative thermal expansion at $\sim$ 96 K, while filled cages do not show a negative thermal expansion. This difference is due to removing the negative phonon modes from CH_4 molecules from the analysis, which are coupled to the low frequency modes of the H_2O cages. This, in return, removes the contributions from the Grüneisen parameters of these modes to the nuclear quantum effect. These are the modes with negative γ_k that lead to negative thermal expansion.

Therefore, the DFT prediction should be taken from the results of empty cages, as the main contribution to this effect would be from the water molecules. DFT predicts these structures to have negative thermal expansion. However, this difference between empty and filled systems, does not affect the isotopic volume change.

The next comparison we can make is between empty clathrate sI and hexagonal ices, to understand the structural differences of the cages to the ice. When we investigate the volume and bulk modulus of the clathrates to ice Ih results from previous studies [6], it is clear that clathrates are much softer structures than ice, with larger volume per molecule and correspondingly smaller bulk modulus.

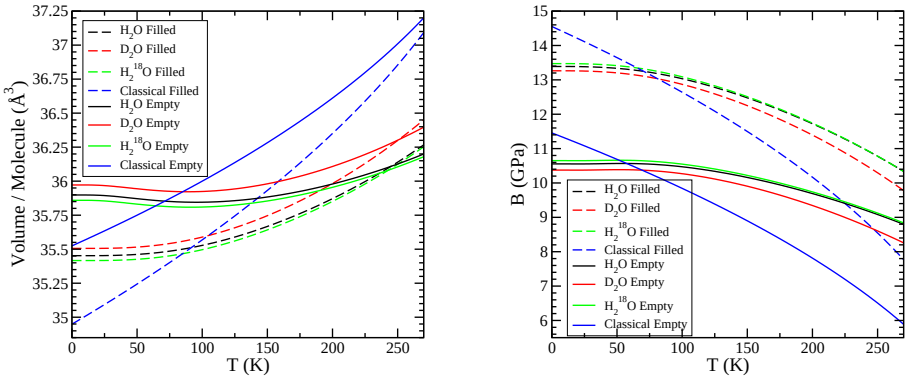

(a) Isotope effect in volume.

(b) Isotope effect in bulk modulus.

Figure 27: Volume per molecule and bulk modulus of clathrate structure I as a function of temperature for different isotopes calculated for zero pressure using the QHA with the vdW-DF$^{\mathrm{PBE}}$ functional. Dashed lines represent the filled structure and the straight lines represent the empty structure.

In addition to the absolute values of these calculations, it is also important

to understand the role of zero point quantum effects, and compare the relative isotope shift from H $\rightarrow$ D. Tables 3 and 13 show that the anomalous isotope shift is larger than ice Ih for higher temperatures, since volume difference increases from 0.20% at 0K to 0.55% at 271K for the empty clathrate sI. This comparison also shows that the isotope shift is enhanced in clathrate structures, in agreement with our results from the Grüneisen parameters.

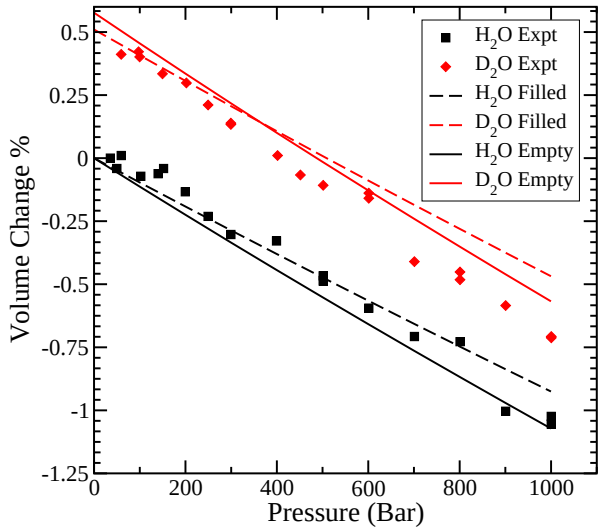

Figure 28: Volume change in clathrate structure I as a function of pressure relative to H_2O for both isotopes at their respective experimental temperatures. Dashed lines are the filled structures and the solid lines are the empty structures. Also shown are the experimental result from Ref. [5].

However, these structures are metastable at this pressure, making it hard to compare to experiments [5]. In order to compare our results of isotope effects to the experimental results [5], we look at the free energy profiles of corresponding temperatures. From Fig. 27a, we take free energy as a function of volume at the corresponding experimental temperatures, $T = 271$ K for H_2O and $T = 273$ K for D_2O. Then we calculate the pressure as a function of volume from this free energy function, as explained in eq. 54. The corresponding volume and pressure values are taken for comparison to two experimental temperature values of 271 K for H_2O and 273 K for D_2O. The absolute values of the pressure and volume for corresponding experimental temperatures are given in Table 13. In order to compare the relative isotope shift in structure I, the experimental H_2O volume at the lowest experimental

pressure and the calculated H_2O volume at zero pressure are both set to zero. Then the relative change in the volume from H_2O to D_2O are plotted in Fig. 28.

These results show that the vdW-DF$^{\mathrm{PBE}}$ functional captures the correct anomalous isotope effect. The relative isotope shift calculations in the volume from H to D for both empty and filled clathrate structure I are in agreement with the experiments. Even though there is a difference in the slopes of the experimental and the theoretical values, which is reflected in the bulk modulus results of the Table 13, the net isotope shift in the volume is well represented in these theoretical lines, as reflected in the volume results of the same table.

6.3 Ice Nice IX and Ice Two II

6.3.1 Structures

6.3.1.1 Structure of Ice IX

"Now suppose," chortled Dr. Breed, enjoying himself, "that there were many possible ways in which water could crystallize, could freeze. Suppose that the sort of ice we skate upon and put into highballs–what we might call ice-one– is only one of several types of ice. Suppose water always froze as ice-one on Earth because it had never had a seed to teach it how to form ice-two, ice- three, ice-four...? And suppose," he rapped on his desk with his old hand again, "that there were one form, which we will call ice-nine–a crystal as hard as this desk–with a melting point of, let us say, one-hundred degrees Fahrenheit, or, better still, a melting point of one-hundred-and-thirty degrees."

Kurt Vonnegut - Cat's Craddle

We are lucky that the structure of real ice nine is different than the one imagined by Kurt Vonnegut. Ice IX is a phase of ice that is stable under pressure and low temperatures, therefore it cannot cause ice I to nucleate at the ambient temperatures, and cannot be used to bring the world's end.

Instead, ice IX forms via a phase transition from metastable ice III. The proton ordering of ice III occurs when high permittivity due to the proton disorder of ice III falls gradually at around 173 K [136]. Neutron diffraction

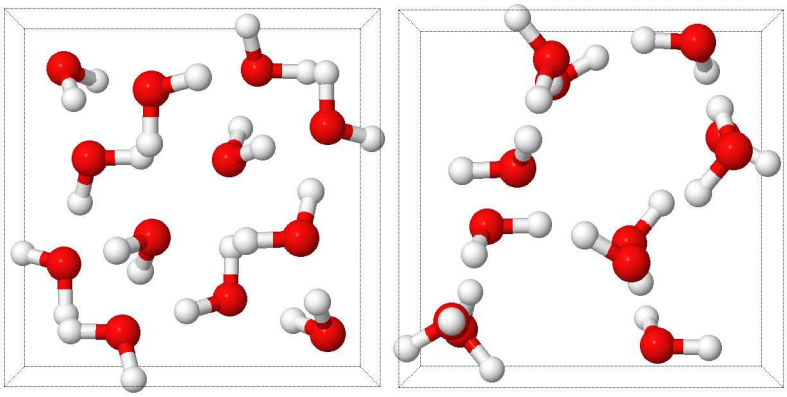

Figure 29: Ice IX structure. The image on the left is the top view of the x-y plane; the image on the right is the side view of the x-z plane.

experiments show that the unit cell of ice IX is tetragonal with proton ordering [137, 138]. Ice IX has 12 molecules in the unit cell as shown in Fig. 29.

6.3.1.2 Structure of Ice II

Ice II forms when pressure is applied on hexagonal ice Ih at temperatures between 193 K and 231 K, or when pressure is released from ice V at 243 K [139]. When ice II is heated, a phase transition to ice III occurs. However, cooling of ice III does not transform it back to ice II, instead, ice III stays metastable until it transforms into ice IX [139].

The structure of ice II is determined both from X-ray [140] and neutron diffraction measurements [141]. This structure is determined to be completely proton ordered.

The unit cell is rhombohedral with $\alpha = 113.1^\circ$ and has 12 molecules, as shown in Fig. 30. This angle is kept constant in all calculations.

Table 14 shows the frozen lattice parameters of ice IX and ice II at the zero temperature and pressure limit, compared with the experimental values. For ice IX, the PBE functional predicts slightly smaller a lattice parameter, but overestimates the tetragonality by predicting much larger c lattice parameter than the vdW-DF$^{\mathrm{PBE}}$ functional. Interestingly, the PBE functional and the vdW-DF$^{\mathrm{PBE}}$ functional give very similar lattice parameters for ice

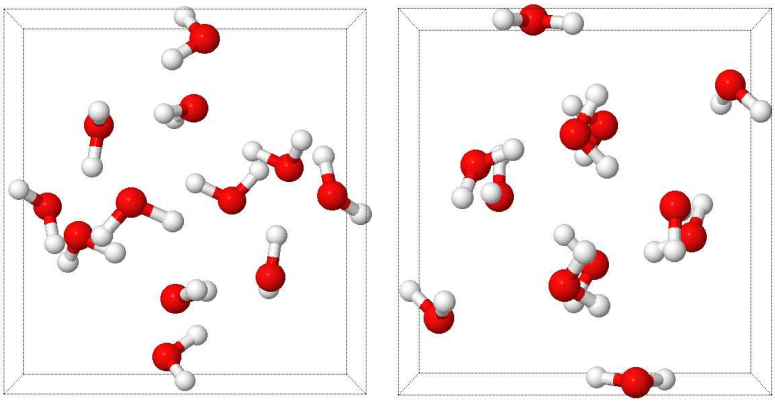

Figure 30: Ice II structure. The image on the left is the top view of the x-y plane; the image on the right is the side view of the x-z plane.

Table 14: Top: Frozen lattice parameters, a and c, and the tetragonality c/a, given in Å.

Ice	XC	a	c	c/a
IX	PBE	6.62	7.33	1.107
IX	vdW-DF$^{\mathrm{PBE}}$	6.65	6.76	1.102
IX	Expt. [137]	6.692	6.715	1.003
II	PBE	7.72	–	–
II	vdW-DF$^{\mathrm{PBE}}$	7.71	–	–
II	Expt. [140]	7.78	–	–

II. As compared to the PBE functional, inclusion of the van der Waals forces with the vdW-DF$^{\mathrm{PBE}}$ functional, shows an overall better agreement with the experiments, especially when the tetragonality of ice IX is considered.

6.3.2 Computational Details

All structural relaxations are performed with dζ+dp atomic orbital basis set developed in Ref. [36], using a real-space mesh cutoff of 500 Ry for the real space integrals, force tolerance of 0.001 eV/Å and a density matrix tolerance of 10^{-5} electrons. For unit cell calculations of ice II, electronic k-grid cutoff of 15Å (corresponding to 50 k-points) is employed, while electronic k-grid Monkhorst Pack of $6 \times 6 \times 6$ (corresponding to 132 k-points) is employed for

ice IX.

For the volume dependency of Kohn-Sham energy, the electronic energy of these relaxed configurations are recalculated using qζ+dp atomic orbital basis sets.

All the force constants calculations are performed with dζ+dp basis sets. We used a real-space mesh cutoff of 800 Ry for the real space integrals and an atomic displacement Δx=0.06 Å for the frozen phonon calculation. The rest of the methodology follows from the previous chapters. The phonon frequencies, $\omega_k(V_0)$ and Grüneisen parameters $\gamma_k(V_0)$ are obtained by diagonalizing the dynamical matrix, computed by finite differences from the atomic forces in a $(3 \times 3 \times 3)$ supercell, at volumes slightly below and above V_0. The Grüneisen parameters are calculated for 3 volumes with k-point sampling and the phonon modes are calculated by diving Brillouin zone to a grid of $9 \times 9 \times 9$, with equal weights on each mode.

6.3.3 Results

6.3.3.1 Phonon Density of States and Grüneisen Parameters

As the density of the ice structure increases from hexagonal ices, ice XI, ice Ih to higher density ices ice II, and ice IX, it becomes harder to distinguish the low frequency Hbond stretching modes from the rest of translations. These low frequency modes clearly have negative Grüneisen parameter in ice XI, ice Ih, and ice Ic, while low frequency modes of ice II, and ice IX have a mixture of negative and positive Grüneisen parameters. Therefore, we will analyse these five bands for the rest of the structures: translational, librational, bending, symmetric and anti-symmetric stretching modes.

Fig. 31 shows the phonon density of states of ice IX, which has a similar profile to ice II. At the low frequency limit, the translational modes ($\omega \sim 197$ cm^{-1}) have a mixture of positive and negative Grüneisen parameters, but overall the average is positive. Librational modes ($\omega \sim 783$ cm^{-1}) always have positive Grüneisen parameters. These two modes are in competition with symmetric ($\omega \sim 3203$ cm^{-1}) and anti-symmetric stretching ($\omega \sim 3385$ cm^{-1}) modes at the high frequency limit, but the Grüneisen parameter of these modes are less negative in magnitude. Similar to ice II, the weight of these modes is smaller than hexagonal ices at $T = 0$ K.

Fig. 32 shows the phonon density of states projected onto hydrogen and oxygen atoms, the corresponding Grüneisen parameters, and the average of

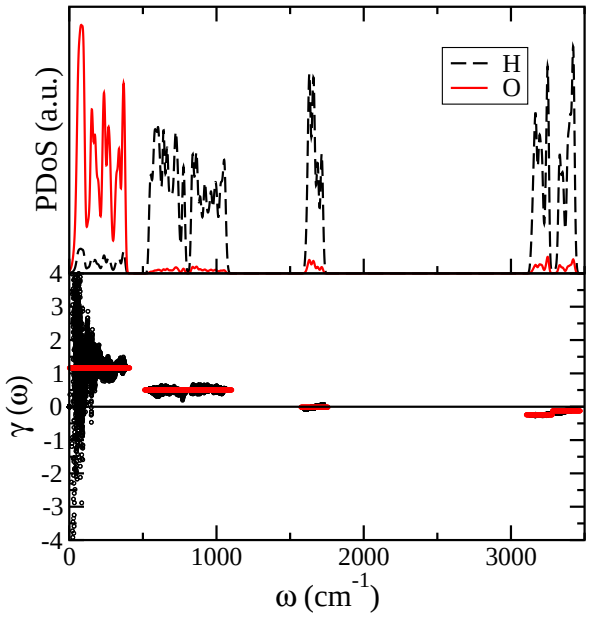

Figure 31: Top: Phonon density of states projected on H and O for ice IX. Bottom: Corresponding Grüneisen parameters, γ_k (black dots), and the average Grüneisen parameter of each band (red lines).

γ_k of each band. For ice II, the low frequency translational modes ($\omega \sim 197$ cm^{-1}) have an average of positive Grüneisen parameters, although the low energy end of the spectra has a mixture of positive and negative modes, pulling the average downwards. Librational modes ($\omega \sim 756$ cm^{-1}) also have positive Grüneisen parameters, and these modes contribute towards a normal isotope effect. As in all structures, the bending modes ($\omega \sim 1667$ cm^{-1}) are very harmonic and they have Grüneisen parameters that are zero, hence do not have a significant effect on the sign of the isotope effect. High frequency symmetric stretching modes ($\omega \sim 3237$ cm^{-1}) and anti-symmetric stretching modes ($\omega \sim 3404$ cm^{-1}) have negative Grüneisen parameters, but the magnitude of γ_k decreases as the density of the structure increases. Therefore, these modes that favour anomalous isotope effect, starts to have less weight at $T = 0$ K limit.

The results of the fine balance between these competing anharmonicities are discussed in the next section.

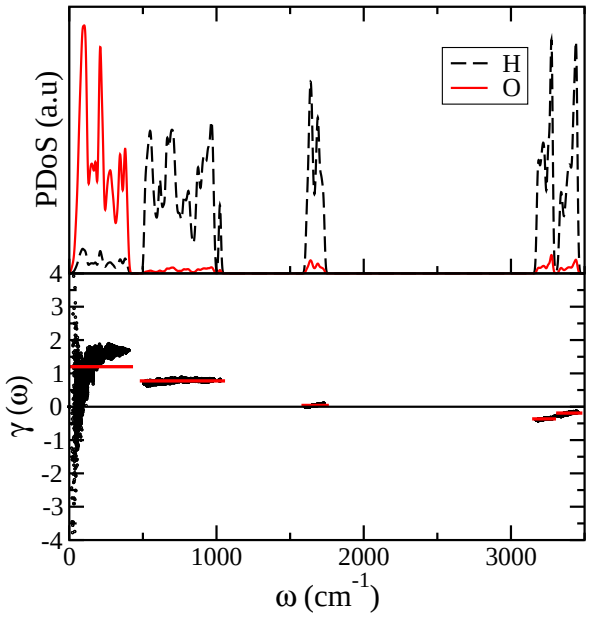

Figure 32: Top: Phonon density of states projected on H and O for ice II. Bottom: Corresponding Grüneisen parameters, γ_k (black dots), and the average Grüneisen parameter of each band (red lines).

6.3.3.2 Isotope Effects on Volume and Bulk Modulus

Differences from the results of previous calculations start to occur in ice structures with high densities. First, we compare the isotope effect on these structures predicted by different functionals. Table 15 compares the volume and bulk modulus results with the PBE and the vdW-DF$^{\mathrm{PBE}}$ functionals. For ice IX, the difference between these two functionals is the most clear. The vdW-DF$^{\mathrm{PBE}}$ functional favours interstitial sites, while it is energetically expensive to fill these interstitial sites with the PBE functional. As a result, this difference becomes visible in ice IX, which is the ice structure with lowest density amongst the high density ices. For ice IX, the PBE functional predicts an anomalous isotope effect on the volume for the replacement of hydrogen with deuterium, both at zero pressure and under experimental pressure values. The magnitude of the anomalous isotope effect is small at the $T = 0$ K limit, and the difference between the volumes of the isotopes, IS(H-D), gets separated with increasing temperature. While the isotope effect on the bulk modulus is consistent for the isotope effect on the volume for the

vdW-DF$^{\mathrm{PBE}}$ functional, the bulk modulus results of different isotopes are the same within the error of our numerical calculations for the PBE functional and this makes it hard to establish the sign of the isotope effect predicted by PBE.

Table 15: Top: For ice IX and ice II, classical volume, V_0, and isotope dependent volumes. Bottom: Classical and isotope dependent bulk modulus. Pressure is given in GPa, temperature in K, volume in Å^3 and bulk modulus in GPa.

Ice	XC	P	T	V_0	H_2O	D_2O	$H_2{}^{18}O$	IS(H-D)	IS(^{16}O -^{18}O)
IX	PBE	0.00	0	26.82	27.30	27.32	27.26	−0.072%	+0.125%
IX	PBE	0.00	165	27.82	27.54	27.59	27.52	−0.173%	+0.078%
IX	PBE	0.28	0	26.13	26.59	26.61	26.56	−0.070%	+0.123%
IX	PBE	0.28	165	27.04	26.80	26.84	26.77	−0.165%	+0.079%
IX	vdW-DF$^{\mathrm{PBE}}$	0.00	0	24.95	25.44	25.41	25.41	+0.095%	+0.103%
IX	vdW-DF$^{\mathrm{PBE}}$	0.00	165	25.84	25.76	25.76	25.74	+0.007%	+0.063%
IX	vdW-DF$^{\mathrm{PBE}}$	0.28	0	24.49	24.93	24.90	24.90	+0.087%	+0.094%
IX	vdW-DF$^{\mathrm{PBE}}$	0.28	165	25.25	25.20	25.19	25.18	+0.009%	+0.058%
IX	Expt. [137]	0.28	165	–	25.060	–	–	–	–
II	PBE	0.00	0	24.77	24.84	24.83	24.83	+0.010%	+0.014%
II	PBE	0.00	123	24.85	24.85	24.85	24.85	+0.005%	+0.010%
II	vdW-DF$^{\mathrm{PBE}}$	0.00	0	24.62	25.10	25.07	25.07	+0.118%	+0.099%
II	vdW-DF$^{\mathrm{PBE}}$	0.00	123	25.17	25.20	25.18	25.18	+0.080%	+0.074%
II	Expt. [140]	0.00	123	–	25.354	–	–	–	–
Ice	XC	P	T	B_0	H_2O	D_2O	$H_2{}^{18}O$	IS(H-D)	IS(^{16}O -^{18}O)
IX	PBE	0.00	0	10.67	10.58	10.57	10.58	+0.039%	−0.068%
IX	PBE	0.00	165	9.81	10.13	10.09	10.13	+0.325%	+0.028%
IX	PBE	0.28	0	10.79	10.71	10.71	10.72	+0.032%	−0.055%
IX	PBE	0.28	165	10.05	10.34	10.31	10.33	+0.276%	+0.035%
IX	vdW-DF$^{\mathrm{PBE}}$	0.00	0	14.36	13.18	13.24	13.24	−0.456%	−0.498%
IX	vdW-DF$^{\mathrm{PBE}}$	0.00	165	11.49	11.89	11.87	11.92	+0.120%	−0.306%
IX	vdW-DF$^{\mathrm{PBE}}$	0.28	0	15.44	14.42	14.47	14.48	−0.355%	−0.388%
IX	vdW-DF$^{\mathrm{PBE}}$	0.28	165	13.03	13.36	13.35	13.39	+0.089%	−0.221%
II	PBE	0.00	0	15.36	15.15	15.16	15.16	+0.010%	+0.014%
II	PBE	0.00	123	15.10	15.09	15.10	15.10	+0.005%	+0.010%
II	vdW-DF$^{\mathrm{PBE}}$	0.00	0	19.10	17.27	17.39	17.37	−0.666%	−0.561%
II	vdW-DF$^{\mathrm{PBE}}$	0.00	123	16.39	16.62	16.68	16.68	−0.373%	−0.370%

For ice II, the PBE and vdW-DF$^{\mathrm{PBE}}$ functionals give consistent results. For both functionals, the isotope effect on volume starts normal at low temperatures and the crossing to the anomalous isotope effect occurs close to the experimental temperature. At high temperatures, the anomalous isotope effect is recovered. While the isotope effect on the volume is robust, the isotope effect on the bulk modulus is different. For the PBE functional, the isotope effect results of different isotopes are close to each other, such that it is hard to determine the sign of the isotope effect within the numerical error of our calculations. However, it is clear that for the vdW-DF$^{\mathrm{PBE}}$ functional, the isotope effect on the bulk modulus becomes anomalous at high temperatures.

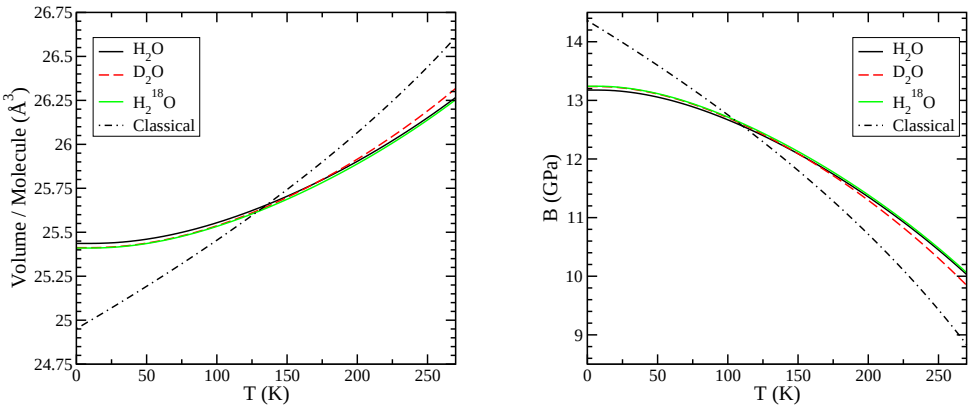

(a) Isotope effect in volume.

(b) Isotope effect in bulk modulus.

Figure 33: Volume per molecule and bulk modulus of ice IX as a function of temperature for different isotopes calculated using the QHA with vdW-DF$^{\mathrm{PBE}}$ functional.

The isotope effect results of the vdW-DF$^{\mathrm{PBE}}$ functional, which will be detailed below, are robust for these systems. Fig. 33 for ice IX and Fig. 34 for ice II show how the isotope effect on the volume and the bulk modulus changes with temperature, as obtained with the vdW-DF$^{\mathrm{PBE}}$ functional. Common for both ice IX and ice II, at $T = 0$ K, the isotope effect is normal. As explained before, this is due to the low frequency modes with $\gamma_k > 0$ dominating the temperature dependence of the volume and bulk modulus.

Fig. 33a, and Fig. 34a show the temperature dependence of the volume of ice IX and ice II respectively, for different isotopes, and the classical limit, where zero point effects are not taken into account. At temperatures after

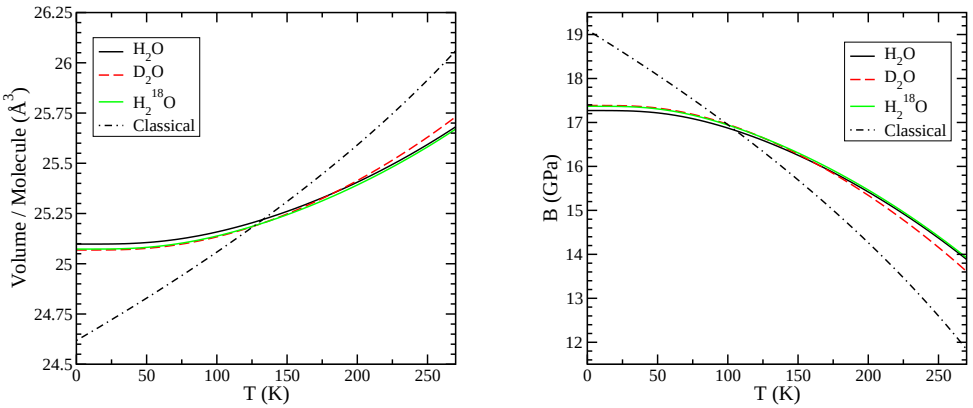

(a) Isotope effect in volume.

(b) Isotope effect in bulk modulus.

Figure 34: Volume per molecule and bulk modulus of ice II as a function of temperature for different isotopes calculated using the QHA with the vdW-DF$^{\mathrm{PBE}}$ functional.

the classical limit crosses the quantum limit, the isotope effect from H to D, becomes anomalous. This is because the low frequency modes become classical, while the energy of the high frequency modes are still above the classical limit at these temperatures. Therefore, the quantum effects of these high frequency modes with $\gamma_k < 0$ start to dominate, and the isotope effect becomes anomalous. The isotope effect on oxygen isotopes from ^{16}O to ^{18}O remains normal for all temperatures at all structures.

The results of bulk modulus are similar to the volume results, as given in Fig. 33b and Fig. 34b for ice IX and ice II respectively. The bulk modulus of D_2O is larger than H_2O at $T = 0$ K, as a normal isotope effect in this limit. As the temperature increases, there is a crossing and the bulk modulus of D_2O is becomes smaller than H_2O, resulting as an anomalous isotope effects at higher temperatures.

Therefore for these structures with increasing density, we see that the anomalous isotope effect is not robust any more and there is a crossing from normal isotope effect to anomalous isotope effect with increasing temperature.

6.4 Ice Eight VIII

6.4.1 Structure

Ice VII and its proton ordered form ice VIII are the most dense ice phases, located at the high pressure region of the ice phase diagram. Ice VIII has tetragonal structure with two interpenetrated networks [142, 143], that are independent of each other, each with underlying structure of ice Ic. Within each network, the aforementioned ice rules are satisfied, but there are no Hbond connection between the two networks. This results in having water molecules of one network in the interstitial cells of the other network. Existence of these interstitial molecules is very interesting. The structure of liquid water is in between ice Ih and ice VIII, where the interstitial sites are starting to be filled compared to ice Ih, but not entirely filled compared to ice VIII. The bonding between these unconnected networks of ice VIII is dominated by the van der Waals interaction. Therefore, the inclusion of vdW forces into the calculations become even more important for this case. We will study this using two different approximations to the exchange and correlation functionals, with and without including vdW interactions. Previous studies that have detailed analysis of the Hbonded O-O networks and non-bonded O$\cdots$O networks, do not include vdW effects in their calculations [144, 145].

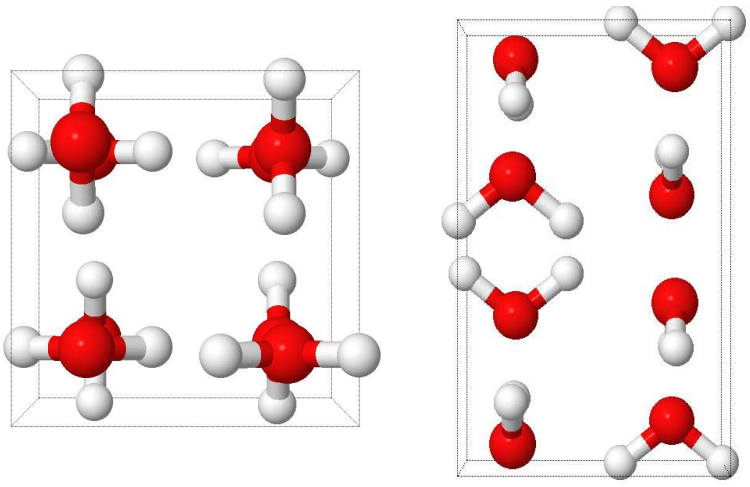

Figure 35: Ice VIII structure. The image on the left is the top view of the x-y plane; the image on the right is the side view of the x-z plane.

The structure of ice VIII is determined to be tetragonal from neutron diffraction experiments. Each interpenetrating layer has ferroelectric ordering along $\hat{z}$-axis with opposite signs, resulting in a net antiferroelectric structure [143, 146–148] Ice VIII has 8 molecules in the unit cell as shown in Fig. 35.

One interesting structural difference of ice VIII is that the oxygen-oxygen distance of the first Hbonded shell is shorter than the shortest non-bonded (vdW) configuration. Each molecule has 4 tetrahedral Hbonded configuration. Experimentally the distance between the molecules of this configuration is: $r_{\rm OO}^{\rm Hbonded} = 2.979(1)$Å [143] and for the vdW-DF$^{\rm PBE}$ functional it is $r_{\rm OO}^{\rm Hbonded} = 2.943$Å. Then, each molecule has 4 vdW bonded configuration, 2 of which are closer than the Hbond distance, and 2 are further. Experimentally, the first vdW bonded (non-bonded) configuration distance is: $r_{\rm OO}^{\rm vdW1} = 2.743(9)$Å [143] and for the vdW-DF$^{\rm PBE}$ functional it is $r_{\rm OO}^{\rm vdW1} = 2.822$Å. The second vdW bonded configuration distance for the vdW-DF$^{\rm PBE}$ functional is: $r_{\rm OO}^{\rm vdW2} = 3.075$Å, resulting an average of 4 vdW bond lengths of $r_{\rm OO}^{\rm vdW} = 2.949$Å, as shown in Table 18.

6.4.2 Computational Details

All structural relaxations are performed with dζ+dp atomic orbital basis set developed by Ref. [36], using a real-space mesh cutoff of 600 Ry for the real space integrals, electronic k-grid Monkhorst Pack of $4\times4\times4$ (corresponding to 32 k-points) for unit cell calculations, force tolerance of 0.001 eV/Å and a density matrix tolerance of 10^{-5} electrons. For the volume dependency of Kohn-Sham energy, the electronic energy of these relaxed configurations are recalculated using qζ+dp atomic orbital basis sets.

All the force constants calculations are performed with dζ+dp basis sets. We used a finer real-space mesh cutoff of 800 Ry with an atomic displacement Δx=0.06 Å for the frozen phonon calculation. The rest of the methodology follows from the previous chapters. The phonon frequencies, $\omega_k(V_0)$ and Grüneisen parameters $\gamma_k(V_0)$ are obtained by diagonalizing the dynamical matrix, computed by finite differences from the atomic forces in a $(3\times3\times3)$ supercell, at volumes slightly below and above V_0. The Grüneisen parameters are calculated for 3 volumes with k-point sampling and the phonon modes are calculated by diving Brillouin zone to a grid of $9\times9\times9$, with equal weights on each mode.

The QH2 level of approximation has been employed in all the ice struc-

tures of this thesis, except for ice VIII. In this case, QH2 makes the volume dependency of the free energy too soft, making the analysis impossible for high temperatures. Therefore, QH1 level of the QHA has been used for the free energy calculations of ice VIII.

6.4.3 Results

6.4.3.1 Phonon Density of States and Grüneisen Parameters

According to DFT calculations, in ice VIII, the nuclear quantum effects result in normal isotope effect [73, 149]. However, it is not immediately clear from these results why the anticorrelations between the Hbond and covalent bond balance each other, resulting in the normal isotope effect. The inelastic neutron scattering spectrum of ice VIII shows a weak coupling between the intra-molecular and inter-molecular modes [150], which may actually point to the normal isotope effect in this system. There are no experiments, to our knowledge, that measure the isotope effects on ice VIII. Therefore, we repeat our analysis of projected density of states and their corresponding Grüneisen parameters for ice VIII structure to compare with these previously established DFT calculations.

At the low frequency limit, the translational modes ($\omega \sim 194$ cm^{-1}), dominated by the oxygen atoms, have clearly positive Grüneisen parameters with a large average. Similarly, librational modes ($\omega \sim 724$ cm^{-1}), also have $\gamma_k > 0$. Bending modes ($\omega \sim 1628$ cm^{-1}), have positive Güneisen parameter, but they are very close to zero on average, similar to the rest of the analysed structures, contributing little to the isotope effect.

At the high frequency limit, the symmetric ($\omega \sim 3392$ cm^{-1}) and anti-symmetric stretching ($\omega \sim 3500$ cm^{-1}) modes have Grüneisen parameters that are slightly negative, but close to zero on average. The main difference between the structures occurs at this high frequency limit. As the density increases, the Grüneisen parameters of the stretching modes get closer to zero, contributing the least, among all the structures, towards the anomalous isotope effect.

6.4.3.2 Isotope Effects on Volume and Bulk Modulus

At the other extreme of the ice phase diagram, at high pressures, the density of the ice is largest. Therefore, in ice VIII, the isotope effect is normal at all temperatures. As explained in the previous section, the contributions from

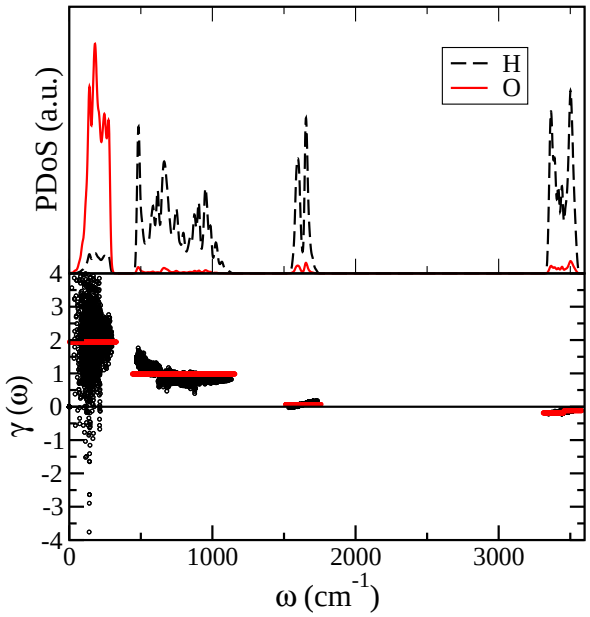

Figure 36: Top: Phonon density of states projected on H and O for ice VIII. Bottom: Corresponding Grüneisen parameters, γ_k (black dots), and the average Grüneisen parameter of each band (red lines).

the negative Grüneisen parameters become small enough to tip the balance of the anharmonities, and result in a normal isotope effect.

When we compare the results with the PBE functional to the vdW-DF$^{\mathrm{PBE}}$ functional, PBE gives larger volume both for classical and quantum limits. With the increase of the pressure, volume decreases significantly, and for both functionals, the isotope effect on volume starts to decrease with increasing temperature. Overall the isotope effect on volume IS(^{16}O -^{18}O) is smaller than IS(H-D).

When the PBE functional is considered, at the zero pressure limit, the isotope effect on bulk modulus is consistent with the isotope effect on volume, both being normal. However, there is an inconsistency in the isotope effect on the bulk modulus under pressure: at $P = 2.5$ GPa the isotope effect on the bulk modulus becomes anomalous. Inclusion of the van der Waals forces with the vdW-DF$^{\mathrm{PBE}}$ functional removes this inconsistency. This shows that the vdW-DF$^{\mathrm{PBE}}$ functional softens the system such that the slope and the curvature of the free energy surface of different isotopes are consistently shifted up to the experimentally measured pressures. At much

Table 16: Top: For ice VIII, classical volume, and isotope dependent volumes. Bottom: Classical and isotope dependent bulk modulus. Pressure is given in GPa, temperature in K, volume in Å^3 and bulk modulus in GPa.

XC	P	T	V_0	H_2O	D_2O	$H_2{}^{18}O$	IS(H-D)	IS(^{16}O -^{18}O)
PBE	0.0	0	20.57	21.70	21.53	21.67	+0.78%	+0.14%
PBE	2.5	0	20.57	19.16	19.03	19.14	+0.68%	+0.10%
vdW-DF$^{\mathrm{PBE}}$	0.0	0	20.04	21.09	20.90	21.06	+0.90%	+0.14%
vdW-DF$^{\mathrm{PBE}}$	2.5	0	18.33	19.06	18.94	19.04	+0.63%	+0.11%
Expt. [143]	2.4	10	–	18.359	–	–	–	–
XC	P	T	B_0	H_2O	D_2O	$H_2{}^{18}O$	IS(H-D)	IS(^{16}O -^{18}O)
PBE	0.0	0	16.39	14.75	15.07	14.82	−2.17%	−0.47%
PBE	2.5	0	23.87	24.71	24.64	24.70	+0.28%	+0.04%
vdW-DF$^{\mathrm{PBE}}$	0.0	0	21.82	16.22	17.42	16.42	−7.40%	−1.23%
vdW-DF$^{\mathrm{PBE}}$	2.5	0	33.51	32.28	32.58	32.33	−0.93%	−0.16%

higher pressures, for example at around $P \sim 5$ GPa, the isotope effects starts normal at low temperatures and then becomes anomalous. Further on, at around $P \sim 10$ GPa, it becomes completely anomalous for bulk modulus also with the vdW-DF$^{\mathrm{PBE}}$ functional. Isotope effect on the volume remains normal at these pressures.

Fig. 37 shows the isotope effect on the volume and the bulk modulus of ice VIII calculated with the vdW-DF$^{\mathrm{PBE}}$ functional. We first present the zero pressure limit where the volume is larger than the experimental pressure region, $P = 2.5$ GPa. Consistently, the bulk modulus is much smaller in the zero pressure limit, making the structure softer than the structure under pressure. For the vdW-DF$^{\mathrm{PBE}}$ functional, the isotope effect on volume and bulk modulus remains normal up to the melting point.

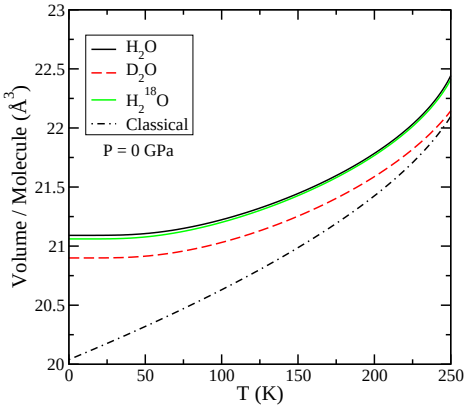

(a) Isotope effect in volume at zero pressure.

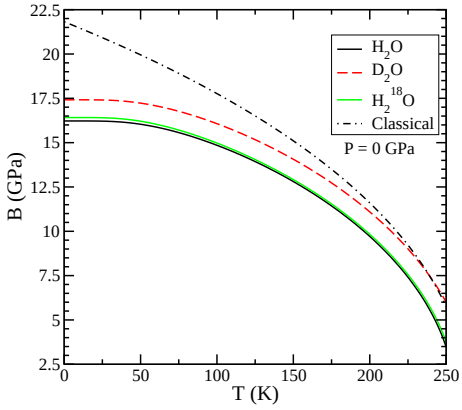

(b) Isotope effect in bulk modulus at zero pressure.

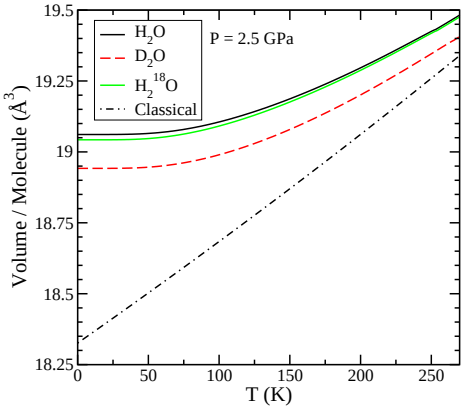

(c) Isotope effect in volume at $P = 2.5$ GPa.

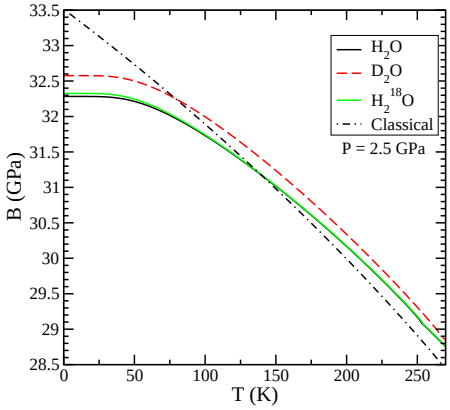

(d) Isotope effect in bulk modulus at $P = 2.5$ GPa.

Figure 37: Volume per molecule and bulk modulus of ice VIII as a function of temperature for different isotopes calculated using the QHA with the vdW-DF$^{\mathrm{PBE}}$ functional.

The normal isotope effect on the volume is very robust in the pressure range up to $P \sim 10$ GPa, and up to the melting point. Therefore, we can conclude that in liquid water, if the density gets higher such that the Hbond networks are broken, the resulting isotope effect would be normal instead of anomalous.

6.5 Amorphous Ices

6.5.1 Structure

Analysing different phases of ice with different densities, and bonding configurations shows the general changes in the isotope effect with increasing density. However, the structure of liquid water is different from these ice phases. In ices, there is always an underlying lattice, resulting in an ordered tetragonality, well defined Hbonds and interstitial sites. Upon melting, this underlying lattice vanishes. There are still Hbond networks in liquid water, but without any order to the system, which makes it difficult to make links from ices to the liquid water. Therefore, we have decided to investigate amorphous ices, where similar to the liquid, there is no long-range order, which can be seen in Fig. 40a.

Amorphous ices occur when the liquid is frozen at low temperatures such that molecular rearrangement cannot occur. High density amorphous ice (HDA) forms when ice Ih or ice Ic is frozen at 77 K at high pressures along the solid-liquid boundary extrapolation, with a sharp transition at 1.12 GPa [139, 151, 152]. When pressure is released to atmospheric pressure, and temperature is increased to ~ 125 K, it remains amorphous, but density decreases, and it transforms into low density amorphous ice (LDA) [153]. When LDA is further heated, above ~ 129 K it goes under a glass transition and then crystallises into ice Ic. The properties of LDA ice are similar to amorphous solid water (ASW) that forms when when liquid water is frozen below ~ 120 K at atmospheric pressure. Another method of producing amorphous ices is firing a jet of water into a cryoliquid at 77 K, and this phase is called hyperquenched glassy water (HGW) [154, 155]. Upon heating, ASW and HGW also go under a glass transition at ~ 136 K, and then crystallise into ice Ic above ~ 150 K [156]. Because they are all low density amorphous ices, ASW, HGW, and LDA are sometimes referred as LDA in the literature.

We prepare our amorphous ices by selecting from the inherent structures from *ab initio* molecular dynamics simulations of liquid water under differ-

ent densities and structures. We distinguish between different amorphous ices depending on their density in this section. In order to make links to the debate in the liquid, we call our structures that are obtained from low density liquid simulations, LDL-like and high density liquid simulations, HDL-like. We obtain one structure of LDL-like amorphous ice from 128 molecule simulations of liquid water with the PBE functional with density $\rho = 1$ g/cm^3 at $T = 300$ K. We obtain two structures of HDL-like amorphous ices from 64 molecule simulations of liquid water with the vdW-DF$^{\mathrm{PBE}}$ functional with density $\rho = 1$ g/cm^3 at $T = 300$ K and one structure at $T = 350$ K. Finally, we obtain one structure of HDL-like amorphous ices from 128 molecule simulations of liquid water with the vdW-DF$^{\mathrm{PBE}}$ functional with a higher density $\rho = 1.2$ g/cm^3 at $T = 300$ K.

Once we obtain the structures, we quench them to $T = 0$ K and repeat the same procedure as before. We calculate the Kohn-Sham energy for several fixed volumes to obtain $E_0(V)$ and calculate the phonon frequencies at around the energy minimum to obtain the free energy with QHA.

6.5.1.1 Changes in the Structure

The calculations start with an inherent structure from the molecular dynamics simulation of 64 molecule water simulation with the vdW-DF$^{\mathrm{PBE}}$ functional with density $\rho = 1$ g/cm^3 at $T = 300$ K, and the structure is quenched to zero temperature. As the volume is decreased, a jump in $E_0(V)$ curve occurs for some of these inherent structures.

Let us first focus on the first step of the procedure. Fixing the lattice parameter at $a = 12.415$ Å, keeping the volume constant, we do conjugate gradient relaxation of this configuration to its minimum energy. At this point, if we compare the number of Hbonds and vdW bonds in the system, we see that there is a change in the overall number of bonds as we relax the system. As a reference, the change in the number of Hbonds of each molecule from the snapshot of molecular dynamics to the conjugate gradient relaxed system is given in Fig. 38a. We see that that upon relaxation, several molecules gain and several of them lose a single Hbond, but there is one molecule that lost 2 Hbonds and one lost 3 Hbonds. This means that upon relaxation, the interstitial sites are closing around those molecules, resulting a lower energy with the van der Waals functional.

After this first relaxation, we change the volume of the cell and relax again for that fixed volume, and continue until a minimum energy is reached. We

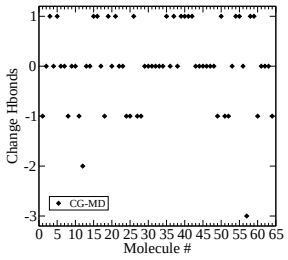

(a) The change in the number of Hbonds of each molecule before and after the relaxation.

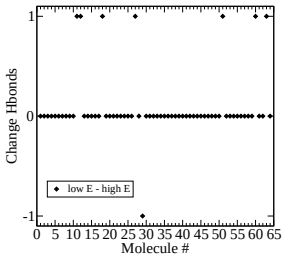

(b) The change in the number of Hbonds of each molecule at the energy change.

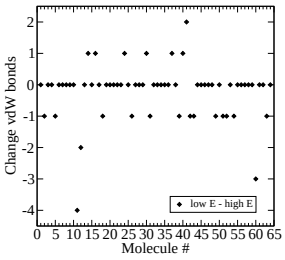

(c) The change in the number of vdW bonds of each molecule at the energy change.

Figure 38: The change, from conjugate gradient relaxed (CG) coordinates to molecular dynamics snapshot (MD), in the number of Hbonds of each molecule at the molecular dynamics cell parameter 12.415 Å is shown in the first panel. The second and third panels show change in the number of Hbonds and vdW bonds of each molecule for cell parameter 12.04 Å. "High E" labels the high energy configuration and "low E" labels the low energy configuration.

give the relaxed coordinates of the previous volume, in fractional coordinates of the lattice parameters, as an input of the new volume. In this way, as the system goes down in energy and volume, we search for a minimum of the Kohn-Sham energy. However, for this specific configuration, we see that there is a local to global minimum transition with a sharp change in the energy curve. This sharp change occurs when the volume decreased from the lattice parameter 12.04 Å to 12.03 Å. Furthermore, if we start with the relaxed fractional coordinates of 12.03 Å and give these as an input to the 12.04 Å cell, we see that this jump is not reversible. This $E_{KS}(V)$ curve if given in Fig. 39

In order to make sure that this is not due to a numerical error, we required the Mesh cutoff of 550.0 Ry and checked that there is not a large jump between the used cutoffs of each cell relaxation. In addition, we used a fine force tolerance of 0.005 eV/Å and density matrix tolerance of 10^{-5} electrons to reduce the numerical error in energy calculations.

Now that we know this is not due to a numerical error in parametrization, we can focus on the two configurations of lattice parameter of 12.04 Å, which corresponds to the volume at the energy drop. Fig. 39 shows

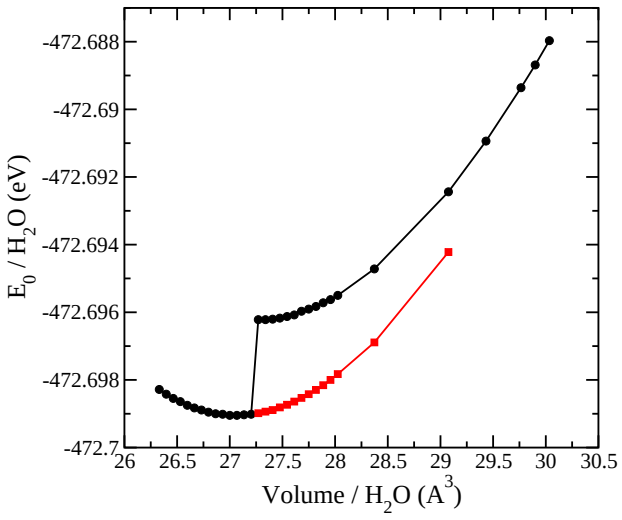

Figure 39: $E_0(V)$ for the selected configuration. The black circles are starting from the large cell size and decreasing the volume, and the red squares are starting from the cell right after the sudden change in the energy and increasing the volume. The lines are to guide the eye.

this sharp change in the Kohn-Sham energy. High energy phase with Kohn-Sham energies before the sharp change in the $E_0(V)$ curve is labelled as the black dots, whereas low energy phase with Kohn-Sham energy after the sharp change in the $E_0(V)$ curve is labelled as the red squares. If we have a look at the number of the bonds in the high and low energy configurations, and count the number of bonds with a cutoff of 4.5 Å around each molecule, we see that the change in energy roughly corresponds to the Hbond energy, consistent with the changes in the number of bonds as shown in Fig. 38b.

Similarly, the vdW energy bond count before and after the sharp change in the energy for the 12.04 Å cell is given in Fig. 38c. Comparing these two plots, the vdW bond configuration is subject to a lot more variation than the Hbond configuration. However, it can be concluded that after the drop in the energy, there is an overall decrease in the vdW bonded configurations, and increase in the Hbonded configurations, filling the interstitial sites and favouring higher density.

The plots of Hbonds (Fig. 38b) and vdW bonds (Fig. 38c) of each molecule show that there is a clear change in the environment of the molecules. The sign of the bond is assigned so that it shows the change in the number

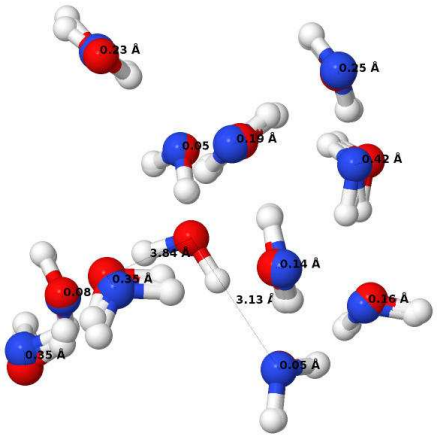

(a) For molecule # 1 the configuration of neighbours at the high energy (red) and the low energy (blue) phase.

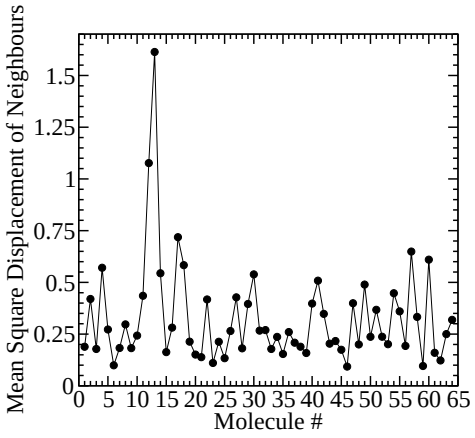

(b) The normalized mean square displacement of the neighbours from high energy phase to the low energy phase for each molecule.

Figure 40: The configuration of the amorphous ice before and after the change in the energy are investigated. Oxygen atoms are labelled with red for high energy phase and blue for low energy phase. Panel (b) shows the mean square displacement of neighbours of each molecule from high energy to the low energy phase.

of bonds in the low energy configuration with respect to the high energy configuration. When this is repeated for each molecule, the overall mean square displacement is given in Fig. 40b.

These results show how the structure finds its equilibrium density through relaxations after quenching from liquid water temperature to amorphous ice at $T = 0$ K. First, its volume decreases, therefore it favours a higher density that its liquid structure. As this happens, the interstitial sites are filled increasing the overall Hbond configuration of the system. At the sudden energy jump point, the change in the total energy is consistent with energy gained by making an Hbond. This jump in the energy is observed in several different inherent structures taken from this molecular dynamics simulations of the vdW-DF$^{\text{PBE}}$ functional at density $\rho = 1$ g/cm^3. The fact that it is irreversible, shows that a stable phase is reached through this change in the configuration. This shows that the vdW-DF$^{\text{PBE}}$ functional favours high density structures. This is in fact consistent with the findings of Ref. [61],

where they show that the vdW-DF$^{\mathrm{PBE}}$ functional tends to make liquid water more HDL-like. This can be seen in the radial distribution functions $g_{OO}(r)$ of this functional, where the second shell of the oxygen-oxygen distribution is almost inside the first shell [61].

For the rest of the discussion, the selected structures do not present the sudden change in the Kohn-Sham energy, and their $E_0(V)$ curve is smooth. This helps to select the configurations around the minimum volume to calculate phonon frequencies and the Grüneisen parameters. And all the following free energy surfaces are, therefore, smooth and do not show this behaviour.

6.5.2 Computational Details

Structural relaxations of LDL-like structure from the PBE functional simulations and HDL-like structure from the vdW-DF$^{\mathrm{PBE}}$ functional simulations of density $\rho = 1.2$ g/cm^3 are performed with dζ+p atomic orbital basis set. Relaxations of HDL-like structure from the vdW-DF$^{\mathrm{PBE}}$ functional simulations of density $\rho = 1$ g/cm^3 at $T = 300$ K are performed with tζ+p atomic orbital basis set. Relaxations of HDL-like structure from the vdW-DF$^{\mathrm{PBE}}$ functional simulations of density $\rho = 1$ g/cm^3 at $T = 350$ K are performed with dζ+dp atomic orbital basis set developed by Ref. [36]. For the volume dependency of Kohn-Sham energy, the electronic energy of these relaxed configurations are recalculated using qζ+dp atomic orbital basis sets.

We have used a real-space mesh cutoff of 550 Ry for the real space integrals, and the used mesh cutoff is consistent in all the fixed volume relaxations. A force tolerance of 0.005 eV/Å and a density matrix tolerance of 10^{-5} electrons is used in the configurational relaxations. All the force constants calculations are performed with the same basis sets used in the initial structural relaxations. The rest of the methodology follows from the previous chapters.

6.5.3 Results

6.5.3.1 Phonon Density of States and Grüneisen Parameters

Following the same methodology, the amorphous structures obtained from the molecular dynamics simulations are quenched to zero temperature. After relaxing the structure and finding its new equilibrium density and volume at the zero temperature limit, the vibrational spectra is calculated around this equilibrium volume and the Grüneisen parameters are obtained.

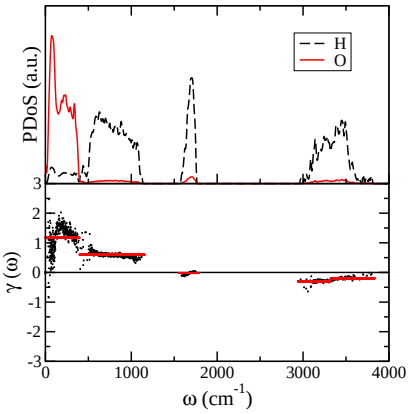

(a) PDoS of LDL-like amorphous ice.

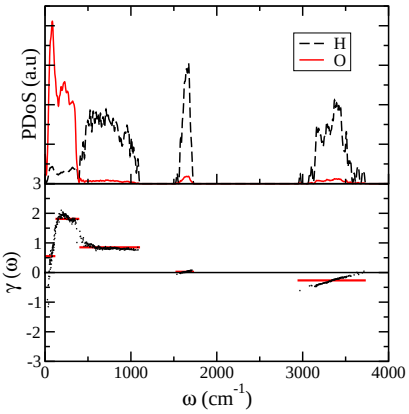

(b) PDoS of HDL-like amorphous ice from $\rho = 1.0\text{g/cm}^3$ $T = 300\text{K}$ simulation.

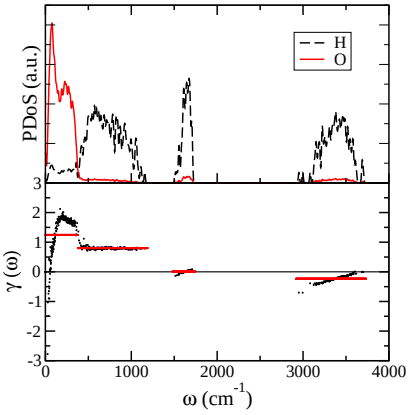

(c) PDoS of HDL-like amorphous ice from $\rho = 1.0\text{g/cm}^3$ $T = 350\text{K}$ simulation.

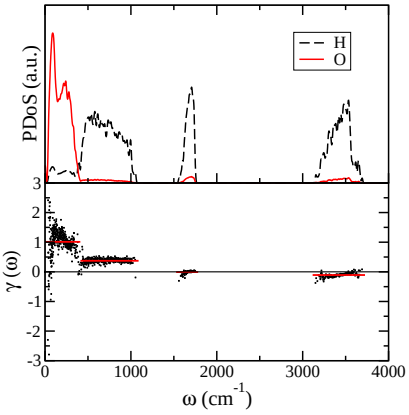

(d) PDoS of HDL-like amorphous ice from $\rho = 1.2\text{g/cm}^3$ $T = 300\text{K}$ simulation.

Figure 41: Top: Phonon density of states projected on H and O for amorphous ices. Bottom: Corresponding Grüneisen parameters, γ_k (black dots), and the average Grüneisen parameter of each band (red lines).

Fig. 41 shows the phonon density of states projected onto hydrogen and oxygen atoms and the corresponding Grüneisen parameter of each mode and the average of each branch. Similar to other ices, the low frequency translational modes ~ 180 cm^{-1} have a large weight from the oxygen atoms and these modes have positive Grüneisen parameter. The librational modes, ~ 700 cm^{-1} are dominated by the hydrogen atoms and these have positive Grüneisen parameter as well. As explained before, these two modes are signatures of hydrogen bonding and they have large positive γ_k. In all structures, the bending modes ~ 1600 cm^{-1} are very harmonic and their average γ_k is around zero, not contributing to the sign of the isotope effect.

The first difference from the ices is that the symmetric and anti-symmetric stretching frequencies, ~ 3300 cm^{-1}, are blueshifted compared to the hexagonal ices. The largest frequency of hexagonal ices is around 3500 cm^{-1}, while it is around 4000 cm^{-1} for amorphous ices. Moreover, the clear two peaks of hexagonal ices vanish, and the stretching modes of amorphous ices resemble liquid water; it is not possible to distinguish between the symmetric and anti-symmetric stretching modes, due to the long range disorder in these systems.

However, a common trend both in hexagonal and amorphous ices is that the slope of the Grüneisen parameters of the stretching modes is positive. The absolute value of γ_k corresponding to the symmetric stretching modes are larger in magnitude than anti-symmetric stretching modes. Furthermore, the magnitudes of the averages of these modes get closer to zero, as compared to hexagonal ices. Therefore, their contribution to the anomalous isotope effect is smaller in amorphous ices.

6.5.3.2 Isotope Effects on Volume and Bulk Modulus

The resulting isotope effect from the balancing of the phonon modes and the Grüneisen parameters is different for different amorphous structures. Table 17 shows both classical and quantum volume per molecule, and the corresponding isotope effect shift in the volume, as well as the bulk modulus. Furthermore, Fig. 42 presents the volume per molecule for different amorphous structures and similarly, Fig. 43 presents the corresponding bulk modulus. Comparing these two figures show that volume and bulk modulus results are consistent with each other. Therefore, the discussion here will focus on the isotope effect on the volume.

For LDL-like amorphous ice, the density is low, and the packing of the

Table 17: Top: For amorphous ices, classical volume, and isotope dependent volumes. Bottom: Classical and isotope dependent bulk modulus. Temperature is given in K, density in g/cm^3, volume in Å^3 and bulk modulus in GPa.

Structure from MD	T	V_0	H_2O	D_2O	$H_2{}^{18}O$	IS(H-D)	IS(^{16}O -^{18}O)
LDL-like $\rho = 1.0$ $T = 300$	0	29.60	30.07	30.12	30.03	−0.18%	+0.14%
LDL-like $\rho = 1.0$ $T = 300$	250	32.37	31.18	31.39	31.16	−0.69%	+0.06%
HDL-like1 $\rho = 1.0$ $T = 300$	0	26.80	27.71	27.63	27.66	+0.28%	+0.16%
HDL-like1 $\rho = 1.0$ $T = 300$	250	30.46	29.01	29.10	28.98	−0.29%	+0.09%
HDL-like2 $\rho = 1.0$ $T = 300$	0	27.21	27.81	27.77	27.78	+0.15%	+0.11%
HDL-like2 $\rho = 1.0$ $T = 300$	250	28.70	28.48	28.51	28.47	−0.10%	+0.05%
HDL-like $\rho = 1.0$ $T = 350$	0	26.78	27.63	27.53	27.58	+0.35%	+0.16%
HDL-like $\rho = 1.2$ $T = 300$	0	24.23	24.57	24.55	24.55	+0.09%	+0.07%
HDL-like $\rho = 1.2$ $T = 300$	250	25.10	25.01	25.02	24.00	−0.04%	+0.03%
Structure	T	B_0	H_2O	D_2O	$H_2{}^{18}O$	IS(H-D)	IS(^{16}O -^{18}O)
LDL-like $\rho = 1.0$ $T = 300$	0	8.87	8.28	8.22	8.33	+0.81%	−0.63%
LDL-like $\rho = 1.0$ $T = 300$	250	4.11	6.15	5.81	6.17	+5.61%	−0.36%
HDL-like1 $\rho = 1.0$ $T = 300$	0	11.74	9.90	10.06	9.99	−1.66%	−0.96%
HDL-like1 $\rho = 1.0$ $T = 300$	250	1.10	5.60	5.34	5.65	+4.60%	−0.95%
HDL-like2 $\rho = 1.0$ $T = 300$	0	11.70	10.80	10.86	10.84	−0.59%	−0.42%
HDL-like2 $\rho = 1.0$ $T = 300$	250	8.65	9.18	9.12	9.19	+0.60%	−0.18%
HDL-like $\rho = 1.0$ $T = 350$	0	14.02	9.69	10.20	9.92	−5.21%	−2.35%
HDL-like $\rho = 1.2$ $T = 300$	0	17.68	16.73	16.79	16.78	−0.38%	−0.29%
HDL-like $\rho = 1.2$ $T = 300$	250	14.45	14.85	14.82	14.86	+0.16%	−0.09%

structure is such that volume per molecule is the largest, both at the classical and the quantum limit. Furthermore, it has more negative Grüneisen parameters for the stretching modes than other amorphous ices. As a result, the isotope effect is normal for LDL-like amorphous ice, up to the melting point. Furthermore, the isotope effect IS(H-D) is divergent with increasing temperature, which signifies that the isotope effect in liquid water is expected to be anomalous.

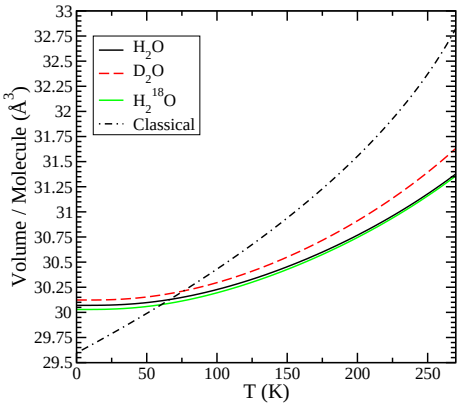

(a) V(T) of LDL-like amorphous ice.

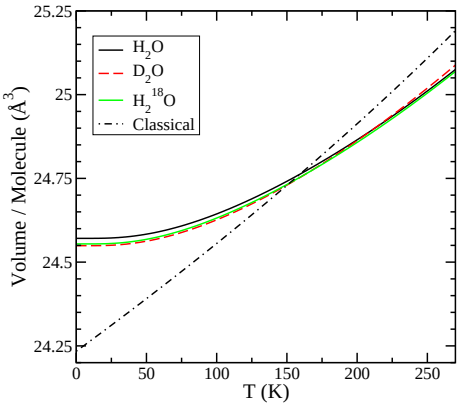

(b) V(T) of HDL-like amorphous ice from $\rho = 1.0\text{g/cm}^3$ $T = 300\text{K}$ simulation.

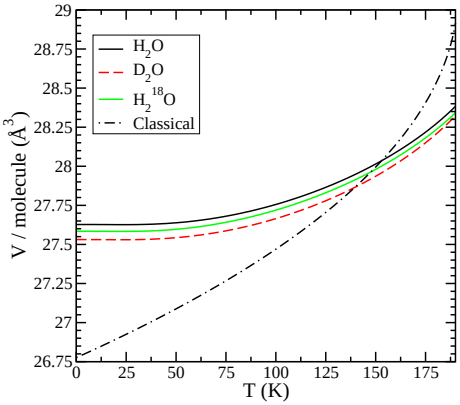

(c) V(T) of HDL-like amorphous ice from $\rho = 1.0\text{g/cm}^3$ $T = 350\text{K}$ simulation.

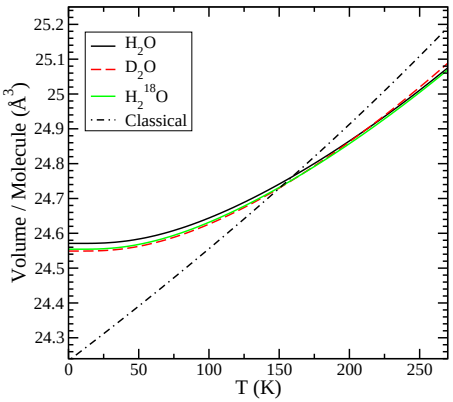

(d) V(T) of HDL-like amorphous ice from $\rho = 1.2\text{g/cm}^3$ $T = 300\text{K}$ simulation.

Figure 42: Volume per molecule for amorphous ices as a function of temperature for different isotopes calculated using the QHA with the vdW-DF$^{\text{PBE}}$ functional.

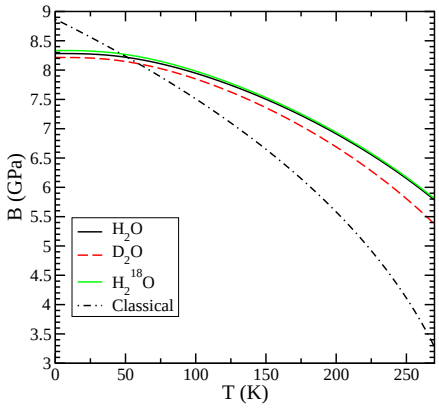

(a) B(T) of LDL-like amorphous ice.

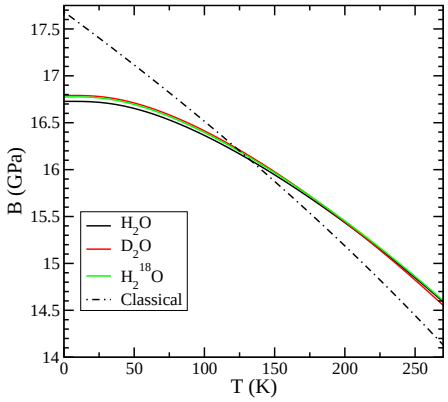

(b) B(T) of HDL-like amorphous ice from $\rho = 1.0\text{g/cm}^3$ $T = 300\text{K}$ simulation.

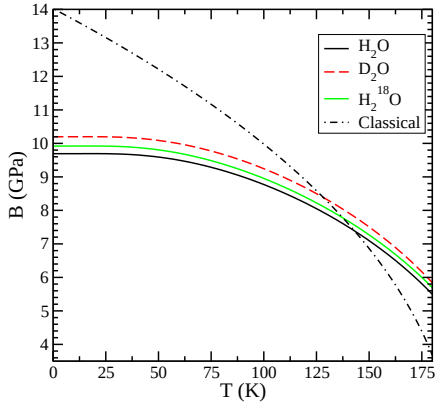

(c) B(T) of HDL-like amorphous ice from $\rho = 1.0\text{g/cm}^3$ $T = 350\text{K}$ simulation.

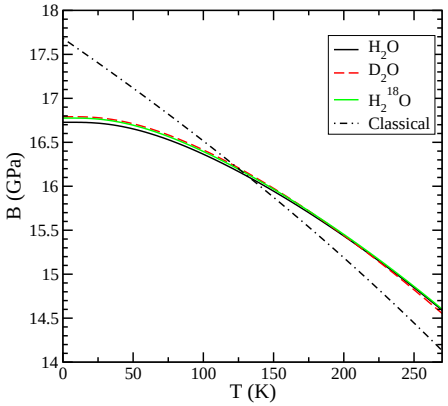

(d) B(T) of HDL-like amorphous ice from $\rho = 1.2\text{g/cm}^3$ $T = 300\text{K}$ simulation.

Figure 43: Bulk modulus for amorphous ices as a function of temperature for different isotopes calculated using the QHA with the vdW-DF$^{\text{PBE}}$ functional.

For HDL-like amorphous ices, the isotope effect is different than for LDL-like amorphous ice. All HDL-like ices, are more closely packed than LDL-like ices, having smaller volume per molecule. For all cases, it starts as the normal isotope effect, labelled with positive IS(H-D) in the zero temperature limit in Table 17. Unlike the LDL-like case, the isotope effect is convergent, with a crossing from normal isotope effect happening at $T \sim 211$ K. Then the isotope effect becomes anomalous and the volumes of H and D get separated up to the melting point. This predicts an anomalous isotope in the liquid phase of these structures as well.

The isotope effect in amorphous ices has largely been neglected before. The modelling for the experimental analysis of the structure factors and distribution functions assume that the structures of these systems do not change with the replacement of the isotope [157]. However, this thesis shows that the isotope effect is different for amorphous ices with LDL-like and HDL-like structures. HDL-like structures are more likely to have normal isotope effect, as the temperature decreases, while LDL-like structures are more likely to have anomalous isotope effect. Therefore, the modelling for these experimental analysis needs to be modified to take these differences into account for better accuracy.

Only the HDL-like structure obtained from molecular dynamics simulations of $\rho = 1.0$ g/cm^3 at $T = 350$ K, has a slightly different behaviour than the rest of the HDL-like structures. For this structure, QHA fails much sooner and it is possible to predict the isotope effect only up to $T \sim 175$K. For higher temperatures, the slope of the total energy from the phonon modes softens the system too much and it becomes unphysical; for example classical behaviour deviates from being linear. The reason for this is due to the high packing of this structure. It is obtained from a simulation that is around the compressibility minimum, and interstitial sites of this structure is more densely packed than the rest of the HDL-like ices. It has the largest positive IS(H-D) value for volume amongst all HDL-like ices, which means that it has the largest normal isotope effect at the zero temperature limit. This indicates that, as the structure of the liquid gets close to the compressibility minimum, the anomaly in the isotope effect is expected to be smaller.

6.6 Conclusion

To conclude this chapter, we have done an extensive analysis of different polymorphs of ice. Starting from cubic ice Ic, which has a similar struc-

ture to hexagonal ices, the investigation of the anomalous isotope effect is extended to high pressure ice phases, ice IX, ice II and the most dense ice phase, ice VIII. Furthermore, we have reproduced the experimental results of anomalous isotope effect in clathrate hydrates. Finally, we analysed LDL-like and HDL-like amorphous ices to obtain how the isotope effect changes in these structures. We concluded that both for the crystalline ice phases and the amorphous ices, the effect from the hydrogen isotopes is anomalous for less dense structures, which have open interstitial sites. There is a transition from anomalous isotope effect of least dense hexagonal ices to normal isotope effect of most dense ice VIII. This is directly linked to the density, but more importantly, the packing of the structures and how densely the interstitial sites are filled. In the next chapter, we will conclude this dissertation by making links between this packing of these structures, compressibility, and the anomalous isotope effect in liquid water.

7 Conclusion: From Ices to Liquid Water

Understanding how nuclear quantum effects change the structure of water is a challenging problem. In this thesis, this problem has been addressed by using the quasiharmonic approximation to understand isotope effect in different ice polymorphs.

We have first presented an anomaly in hexagonal ice, which, until our work, had never been explained. It has been experimentally known that the isotope effect on the hexagonal ice is anomalous, where the volume of D_2O is larger than H_2O [3]. This goes against normal isotope effect where the heavy isotope is expected to have smaller volume, such as in the case of Ne [37–39]. Although this anomaly has been known from experiments, surprisingly, it had never been explained and its relevance within the context of the anomalies of water is only now being explored. In this thesis, we have analysed how hydrogen bonds in ice change with the quantum effects, by calculating how zero point energy changes the structure of the system. To obtain the Helmholtz free energy, we have employed the QHA by calculating the Grüneisen parameter of each phonon mode. By projecting the phonon density of states on hydrogen and oxygen atoms of the system, and by comparing the corresponding Grüneinsen parameter of the mode, we have shown that there is a competition between intermolecular Hbonds, and intramolecular OH covalent bonds of hexagonal ices. The Grüneisen constants of intramolecular covalent stretching modes have opposite sign to those of the intermolecular Hbond bending modes. These can be understood as competing anharmonicities while fine balance is the origin of the anomalous isotope effect. While D_2O is a smaller molecule with shorter OH covalent bonds, the anticorrelation leads to longer Hbonds, resulting as a larger volume than H_2O.

We have also done a similar analysis on $H_2{}^{18}O$. Even though it has essentially the same molecular mass as D_2O, DFT has predicted that the cancellations of the Grüneisen parameters of anharmonicities leads to a normal isotope effect. This prediction has been confirmed by experiments on the volume of $H_2{}^{18}O$, which have also been done for the first time within our collaboration. The competition between the anomalous isotope effect from hydrogen atoms and the normal isotope effect from oxygen atoms, explains why the expansion from the classical frozen volume to the quantum volume is smaller in hexagonal ice than Ne [6, 39].

With the structural analysis of the lattice parameters and the volume of hexagonal ices, we have also computed quantum effects on the bulk modulus. Very little is know about this, even though it is a very relevant parameter given that understanding anomalous compressibility of ice might shed light into the anomalies of liquid water. There is a large dispersion in the experimental results on the bulk modulus, and no detailed experimental or theoretical analysis on the anisotropy of the bulk modulus. As there are different lattice parameters and directionality of the system, the bulk modulus along the x-y plane and the z-axis is different. Furthermore, a similar anomalous isotope effect is expected to exist on the bulk modulus. Therefore, we have conducted an analysis on the different components of the strain tensor and shown that the frozen bulk modulus along the z-axis is larger than the compressibility along the x-y plane. In addition, we have calculated the isotope effect on the total bulk modulus of the hexagonal ices. We have concluded that there is a similar anomalous isotope effect, that the bulk modulus of D_2O is smaller than H_2O, and normal isotope effect in the bulk modulus of oxygen atoms.

Although the qualitative results on the structural properties are similar for both hexagonal ices; proton ordered ice XI and proton disordered ice Ih, there is also an isotope effect in the phase transition temperature. Experimentally, the isotope effect on the phase transition between ice XI and ice Ih is such that the transition temperature is 4 K larger for D_2O than H_2. The source of this isotope effect has also been investigated by a detailed analysis of contributions to the total Helmholtz free energy from each term. There, we have resolved, for the first time, that this difference in the transition temperatures of different isotopes is entirely due to the difference in the zero point energies. DFT predicts this isotope effect in the temperature as 6 K, in good agreement with the experimental results. In addition, we have analysed that the most stable phase of ice at the zero temperature is ferroelectric proton ordered ice XI, and the free energy of antiferroelectric proton ordered hexagonal ice, ice aXI, is in between ice XI and proton disordered ice Ih.

After this detailed analysis on the structures of hexagonal ices, ice XI and ice Ih, we have moved on to investigating the isotope effect on different polymorphs of ice. First, we have obtained that in cubic ice, ice Ic, the isotope effect is anomalous, similarly to ice Ih. Next, we have looked into clathrate hydrates, where in structure I with CH_4 filling, it has been experimentally shown that the isotope effect is anomalous [5]. We have reproduced this anomalous isotope effect in good agreement with the experiments, and shown

that the effect is anomalous regardless of the filling of the ice cages. Then we have moved onto high pressure ice phases, where the interstitial sites of hexagonal ices start to get filled. In the intermediate ice phases, ice IX and ice II, we observe that the difference between the volumes of H and D, starts as a small and normal isotope effect and becomes anomalous at much higher temperatures. Once we get to the other end of the phase diagram, ice VIII is the most dense ice phase, where the interstitial sites are completely filled, the isotope effect on the volume becomes completely normal both at zero pressure and at high pressures. The isotope effect on the volume is very robust, unlike the isotope effect in the bulk modulus, which is much harder to obtain with high accuracy. The bonding is well defined in ice phases, while in liquid water, there is no underlying lattice and no long range order. Therefore, we have decided to look into amorphous ices. We have obtained our amorphous ices from *ab initio* molecular dynamics simulations of liquid water. Low and high density liquid like amorphous ices have been analysed, and a transition has been observed from the anomalous isotope effect in LDL-like amorphous ices to a normal isotope effect in HDL-like amorphous ices at the zero temperature limit.

Table 18: Average oxygen-oxygen distance in Å for Hbonded and vdW bonded configurations and average number of bonds per molecule for different configurations of structures. The quantum H_2O volume in Å^3 and isotope effect from hydrogen to deuterium, IS(H-D) at zero temperature and pressure are also included.

Ice	$< r_{OO}^{\text{Hbond}} >$	$< N^{\text{Hbond}} >$	$< r_{OO}^{\text{vdW}} >$	$< N^{\text{vdW}} >$	$V_{\text{H}_2\text{O}}$	IS(H-D)
XI	2.719	4.000	0.000	0.000	31.41	−0.32%
Clathrate	2.728	4.000	0.000	0.000	35.90	−0.20%
LDL-like$^{\rho=1.0}_{T=300}$	2.765	3.953	3.899	0.688	30.07	−0.18%
Ic	2.719	4.000	0.000	0.000	31.60	−0.16%
HDL-like$^{\rho=1.2}_{T=300}$	2.815	4.047	3.582	2.109	24.57	+0.09%
IX	2.737	4.000	3.489	2.000	25.44	+0.10%
II	2.756	4.000	3.487	2.000	25.10	+0.12%
HDL-like2$^{\rho=1.0}_{T=300}$	2.783	4.063	3.748	0.969	27.81	+0.15%
HDL-like1$^{\rho=1.0}_{T=300}$	2.790	4.063	3.622	0.969	27.71	+0.28%
HDL-like$^{\rho=1.0}_{T=350}$	2.917	3.781	3.834	1.938	27.63	+0.35%
VIII	2.943	4.000	2.949	4.000	21.09	+0.90%

These observations lets us make one final analysis on these systems. Table 18 shows the average distance between oxygen atoms when they are Hbonded,

$< r_{OO}^{\mathrm{Hbond}} >$, van der Waals bonded $< r_{OO}^{\mathrm{vdW}} >$, and the average number of each bond in the analysed configurations. Also included are the isotope effect with respect to H_2O and its quantum volume. The structures are listed from the most anomalous to least anomalous.

For the structures with anomalous effect, the Hbond length is small and is highly populated, while those systems have no (ice XI, clathrate, ice Ic) or very few (LDL-like amorphous) vdW bonds. As the density of the structures increases, moving on to ices IX, HDL-like amorphous, ice II, Hbond length keeps increasing, but more importantly, the systems have more van der Waals bonds, populating the interstitial sites. Then the effect starts to become normal, but small, and a transition to anomalous isotope effect happens at high temperatures.

In the most extreme case of ice VIII, both Hbond length is largest, vdW bond length is smallest and number of vdW bonds is largest. Then, for all temperatures and pressures, the isotope effect stays normal.

This shows that the density or r_{OO} distance by itself is not enough to predict the sign of the isotope effect. For example for HDL-like$_{T=300}^{\rho=1.2}$ structure, in spite of the fact that r_{OO} distance of both bonds are larger than ice IX and ice II, the volume is smaller, resulting as quite a large density. This is because both bonds are more populated, leading to a conclusion of smaller volume per molecule and a normal isotope effect, after all. Therefore, there is a fine balance between the bond length distances and how many bonds each molecule has. Although it is not enough by itself, the density is an overall signature of this fine balance.

Finally, we can make some links to liquid water, by exploiting the experimental results on the isotope effect on the volume of liquid water [1, 18]. Fig. 44 shows the difference between the volume per molecule of liquid water with D_2O and H_2O, $V_{D_2O} - V_{H_2O}$, replotted from Fig. 1a of Introduction. This shows that the volume difference decreases with increasing temperature, therefore the isotope effect goes from anomalous towards normal, but not crossing up to the boiling temperature. Fig. 44b shows the second derivative of the volume difference between the isotopes (Fig. 44), obtained to show how the slope of the isotope effect changes with increasing temperature. Here, we can observe an interesting result: There are two different regions in Fig. 44b, a rapidly decresing slope with increasing temperature up to $T \sim 310$ K, and a slowly decresing region until close to the melting temperature.

As the hexagonal ice Ih, which is already a structure with large anoma-

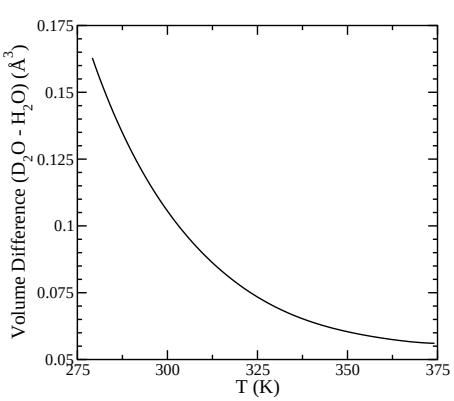

(a) Isotope effect in water.

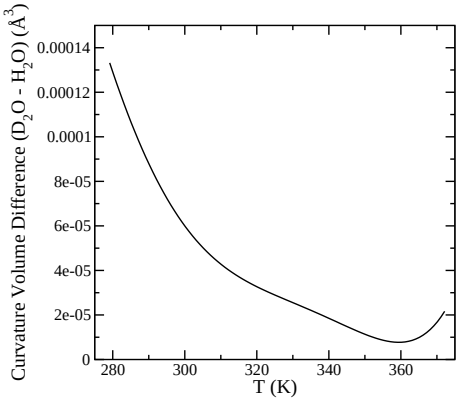

(b) Curvature of isotope effect in water.

Figure 44: Isotope effect on the volume per molecule of liquid water, calculated from Fig. 1a of Introduction, obtained from Ref. [1].

lous isotope effect, melts, the effect in liquid water also starts as large and anomalous. With the increasing temperature, the anomaly of the isotope effect decreases rapidly up to $T \sim 310$ K, which is close to isothermal compressibility minimum temperature, $T \sim 320$ K. Until the compressibility minimum temperature, all the interstitial sites are being filled, and the isotope effect goes towards being normal very quickly. This is similar to moving from ice Ih towards ice VIII in the analysed structures. Once the compressibility minimum is reached, then the change in the isotope effect is stabilised and it keeps on decreasing at a much slower rate, until it gets close to the boiling temperature. With this, we can conclude that the nuclear quantum effects and anomalous isotope effect are linked to the compressibility minimum of liquid water. This conclusion opens new horizons for the development of semi-empirical water models, showing that a complete theory should be able to explain different anomalies of water, in different regions of the phase diagram.

References

[1] George S. Kell. Effects of isotopic composition, temperature, pressure, and dissolved gasses on the density of liquid water. *J. Phys. Chem. Ref. Data*, 6:1109–1131, 1977.

[2] C. P. Herrero and Rafael Ramírez. Isotope effects in ice *ih*: A path-integral simulation. *J. Chem. Phys*, 134:094510, 2011.

[3] K. Röttger, A. Endriss, J. Ihringer, S. Doyle, and W. F. Kuhs. Lattice constants and thermal expansion of H_2O and D_2O ice i*h* between 10 and 265 K. *Acta Cryst.*, B50:644–648, 1994.

[4] Rainer Feistel and Wolfgang Wagner. A new equation of state for H_2O ice ih. *Journal of Physical and Chemical Reference Data*, 35:1021–1047, 2006.

[5] Alice Klapproth, Evgeny Goreshnik, Doroteya Staykova, Helmut Klein, and Werner F Kuhs. Structural studies of gas hydrates. *Canadian Journal of Physics*, 81:503–518, 2003.

[6] B. Pamuk, J. M. Soler, R. Ramirez, C. P. Herrero, P. W. Stephens, P. B. Allen, and M.-V. Fernandez-Serra. Anomalous nuclear quantum effects in ice. *Phys. Rev. Lett.*, 108:193003–193008, 2012.

[7] J. P. Perdew, K. Burke, and M. Ernzerhof. Generalized Gradient Approximation Made Simple. *Phys. Rev. Lett.*, 77:3865, 1996.

[8] M. Dion, H. Rydberg, E. Schröder, D. C. Langreth, and B. I. Lundqvist. Van der Waals Density Functional for General Geometries. *Phys. Rev. Lett.*, 92:246401, 2004.

[9] J. Wang, G. Roman-Perez, J. M. Soler, E. Artacho, and M.-V.Fernandez-Serra. Density, structure and dynamics of water: the effect of van der waals interactions. *J. Chem. Phys.*, 134:024516, 2011.

[10] Y. Zhang and W. Yang. Comment on "Generalized Gradient Approximation Made Simple". *Phys. Rev. Lett.*, 80:890, 1988.

[11] S. Habershon, T. E. Markland, and D. E. Manolopoulos. Competing quantum effects in the dynamics of a flexible water model. *J. Chem. Phys.*, 131(11):024501, 2009.

[12] George S. Fanourgakis and Sotiris S. Xantheas. Development of transferable interaction potentials for water. V. Extension of the flexible, polarizable, Thole-type model potential (TTM3-F, v. 3.0) to describe the vibrational spectra of water clusters and liquid water. *J. Chem. Phys.*, 128:074506, 2008.

[13] R. E. Gagnon, H. Kiefte, M. J. Clouter, and Edward Whalley. Pressure dependence of the elastic constants of ice ih to 2.8 kbar by brillouin spectroscopy. *J. Chem. Phys.*, 89:4522–4528, 1988.

[14] A. Sani, M. Hanfland, and D. Levy. Pressure and temperature dependence of the ferroelectric-paraelectric phase transition in $PbTiO_3$. *Journal of Solid State Chemistry*, 167:446–452, 2002.

[15] M.V Fernandez-Serra and E. Artacho. Electrons and hydrogen-bond connectivity in liquid water. *Phys. Rev. Lett.*, 96:016404, 2006.

[16] N.N. Smirnova, T.A. Bykova, K. Van Durme, and B. Van Mele. Thermodynamic properties of deuterium oxide in the temperature range from 6 to 350 k. *J. Chem. Thermodynamics*, 38:879–883, 2006.

[17] C. A. Angell, J. Shuppert, and J. C. Tucker. Anomalous properties of supercooled water. heat capacity, expansivity, and proton magnetic resonance chemical shift from 0 to $\sim 38^o$. *J. Phys. Chem.*, 77:3092, 1973.

[18] G. S. Kell. Precise representation of volume properties of water at one atmosphere. *Journal of Chemical & Engineering Data*, 12:66–69, 1967.

[19] Felix Franks. *Water - A Matrix of Life*. Royal Society of Chemistry, 2000.

[20] B. Guillot. *J. Mol. Liq.*, 101:219, 2002.

[21] D. Paschek. *J. Chem. Phys.*, 120:6674, 2004.

[22] J. L. F. Abascal and C. Vega. A general purpose model for the condensed phases of water: Tip4p/2005. *J. Chem. Phys.*, 123:234505, 2005.

[23] H. L. Pi, J. L. Aragones, C. Vega, E. G. Noya, J. L. F. Abascal, M. A. Gonzalez, and C. McBride. *Mol. Phys.*, 107:365, 2009.

[24] Pradeep Kumar, Giancarlo Franzese, and H Eugene Stanley. Dynamics and thermodynamics of water. *J. Phys.: Condens. Matter*, 20:244114–244126, 2008.

[25] F. Mallamace, C. Corsaro, and H. E. Stanley. *Proc. Nat. Acc. Sci.*, 110:4899, 2013.

[26] P. Kumar and H. E. Stanley. *J. Phys. Chem. B*, 115:14269, 2011.

[27] F. Sciortino, I. Saika-Voivod, and P. H. Poole. *Phys. Chem. Chem. Phys.*, 13:19759, 2011.

[28] J. L. F. Abascal and C. Vega. *J. Chem. Phys.*, 134:186101, 2011.

[29] D. Paschek. *Phys. Rev. Lett.*, 94:217802, 2005.

[30] D. Corradini, M. Rovere, and P. Gallo. *J. Chem. Phys.*, 132:134508, 2010.

[31] F. Sciortino, P. H. Poole, U. Essmann, and H. E. Stanley. *Phys. Rev. E*, 55:727, 1997.

[32] E. B. Moore and V. Molinero. *Nature*, 479:506, 2011.

[33] D. T. Limmer and D. Chandler. *J. Chem. Phys.*, 137:044509, 2012.

[34] C. Huang, K. T. Wikfeldt, T. Tokushima, D. Nordlund, Y. Harada, U. Bergmann, M. Niebuhr, T. M. Weiss, Y. Horikawa, M. Leetmaa, M. P. Ljungberg, O. Takahashi, A. Lenz, L. Ojamäe, S. Shin A. P. Lyubartsev, L. G. M. Pettersson, and A. Nilsson. *Proc. Nat. Acc. Sci.*, 106:15214, 2009.

[35] S. Kaya, D. Schlesinger, S. Yamamoto, J. T. Newberg, H. Ogasawara H. Bluhm, T. Kendelewicz, Jr. G. E. Brown, L. G. M. Pettersson, and A. Nilsson. *Sci. Rep.*, 3:1074, 2013.

[36] Fabiano Corsetti, M-V Fernández-Serra, José M Soler, and Emilio Artacho. Optimal finite-range atomic basis sets for liquid water and ice. *J. Phys.: Condens. Matter*, 25:435504–435515, 2013.

[37] D.N. Batchelder, D.L. Losee, and R.O. Simmons. Isotope effects in the lattice constant and thermal expansion of ^{20}Ne and ^{22}Ne single crystals. *Phys. Rev.*, 173:873, 1968.

[38] C. P. Herrero. Isotope effects in structural and thermodynamic properties of solid neon. *Phys. Rev. B*, 65:014112, 2001.

[39] P. B. Allen. Zero-point and isotope shifts: relation to thermal shifts. *Phil. Mag. B*, 70:527–534, 1994.

[40] K. Röttger, A. Endriss, J. Ihringer, S. Doyle, and W. F. Kuhs. Lattice constants and thermal expansion of H_2O and D_2O ice ih between 10 and 265 K. addendum. *Acta Cryst.*, B68:91, 2012.

[41] A. K. Soper and C. J. Benmore. Quantum differences between heavy and light water. *Phys. Rev. Lett.*, 101:065502, 2008.

[42] Rafael Ramírez and C. P. Herrero. Quantum path integral simulation of isotope effects in the melting temperature of ice ih. *J. Chem. Phys.*, 133:144511, 2010.

[43] J. A. Morrone and R. Car. Nuclear quantum effects in water. *Phys. Rev. Lett.*, 101:017801, 2008.

[44] Xin-Zheng Li, Brent Walker, and Angelos Michaelides. Quantum nature of the hydrogen bond. *Proc. Nat. Acc. Sci.*, 108:6369–6373, 2011.

[45] A. Zeidler, P. S. Salmon, H. E. Fischer, J. C. Neuefeind, J. M. Simonson, H. Lemmel, H. Rauch, and T. E. Markland. Oxygen as a site specific probe of the structure of water and oxide materials. *Phys. Rev. Lett.*, 107:145501, 2011.

[46] E. Libowitzky. Correlation of o-h stretching frequencies and o-h$\cdots$o hydrogen bond lengths in minerals. *Monatschefte für Chemie*, 130: 1047–1059, 1999.

[47] B. Minceva-Sukarova, W. F. Sherman, and G. R. Wilkinson. The raman spectra of ice (i_h, ii, iii, vi and ix) as functions of pressure and temperature. *J. Phys. C: Solid State Phys.*, 17:5833–5850, 1984.

[48] F. O. Libnau, J. Toft, A. A. Christy, and O. M. Kvalheim. Structure of liquid water determined from infrared temperature profiling and evolutionalry curve resolution. *J. Am. Chem. Soc.*, 116:8311–8316, 1994.

[49] William R. Cook Jr. Thermal expansion of crystals with KH_2PO_4 structure. *J. Appl. Phys.*, 38:1637, 1967.

[50] J. D. Bernal and R. H. Fowler. A Theory of Water and Ionic Solution, with Particular Reference to Hydrogen and Hydroxyl Ions. *J. Chem. Phys.*, 1:515, 1933.

[51] Linus Pauling. The structure and entropy of ice and of other crystals with some randomness of atomic arrangement. *J. Am. Chem. Soc.*, 57: 2680–2684, 1935.

[52] Y. Tajima, T. Matsuo, and H. Suga. Phase transition in koh-doped hexagonal ice. *Nature*, 299:810, 1982.

[53] Takasuke Matsuo, Yoshimitsu Tajima, and Hiroshi Suga. Calorimetric study of a phase transition in D_2O ice ih doped with KOD: Ice xi. *J. Phys. Chem. Solids*, 47:165–173, 1986.

[54] Richard M. Martin. *Electronic Structure*. Cambridge University Press, Cambridge, UK, 2004.

[55] L.H. Thomas. The calculation of atomic fields. *Proc. Cambridge Phil. Soc.*, 23:542–548, 1927.

[56] P.A.M. Dirac. Note on exchange phenomena in the thomas-fermi atom. *Proc. Cambridge Phil. Soc.*, 26:376–385, 1930.

[57] P. Hohenberg and W. Kohn. Inhomogeneous Electron Gas. *Phys. Rev.*, 136:b864, 1964.

[58] W. Kohn and L. J. Sham. Self-Consistent Equations Including Exchange and Correlation Effects. *Phys. Rev.*, 140:a1133, 1965.

[59] D. M. Ceperley and B. J. Alder. Ground state of the electron gas by a stochastic method. *Phys. Rev. Lett.*, 45:566, 1980.

[60] Guillermo Román-Pérez and José M. Soler. Efficient implementation of a van der waals density functional: Application to double-wall carbon nanotubes. *Phys. Rev. Lett.*, 103(9):096102, 2009.

[61] Fabiano Corsetti, Emilio Artacho, José M. Soler, S. S. Alexandre, and M.-V. Fernández-Serra. Room temperature compressibility and diffusivity of liquid water from first principles. *J. Chem. Phys.*, 139(19): 194502, 2013.

[62] P. Ordejón, E. Artacho, and J. M. Soler. Self-consistent order-N density-functional calculations for very large systems. *Phys. Rev. B*, 53:10441, 1996.

[63] J. M. Soler, E. Artacho, J. D. Gale, A. García, J. Junquera, P. Ordejón, and D. Sánchez-Portal. The Siesta method for ab initio order-N materials simulation. *J Phys. Condens. Matter*, 14:2745, 2002.

[64] J. M. Ziman. *Principles of the Theory of Solids*. Cambridge University Press, 1979.

[65] R. Ramírez, N. Neuerburg, M.-V. Fernández-Serra, and C. P. Herrero. Quasi-harmonic approximation of thermodynamic properties of ice ih, ii, and iii. *J. Chem. Phys.*, 137:044502–044513, 2012.

[66] W. F. Giauque and J. W. Stout. The entropy of water and the third law of thermodynamics. the heat capacity of ice from 15 to 273 K. *J. Am. Chem. Soc.*, 58 (7):1144–1150, 1936.

[67] W. F. Giauque and Muriel F. Ashley. Molecular rotation in ice at 10 K. free energy of formation and entropy of water. *Phys. Rev.*, 43:81–82, 1933.

[68] Yoshimitsu Tajima, Takasuke Matsuo, and Hiroshi Suga. Calorimetric study of phase transition in hexagonal ice doped with alkali hydroxides. *J. Phys. Chem. Solids*, 45:1135–1144, 1984.

[69] I. Hamada. A van der waals density functional study of ice ih. *J. Chem. Phys.*, 133:214503, 2010.

[70] Francesco Paesani, Sotiris S. Xantheas, and Gregory A. Voth. Infrared spectroscopy and hydrogen-bond dynamics of liquid water from centroid molecular dynamics with an ab initio-based force field. *The Journal of Physical Chemistry B*, 113:13118–13130, 2009.

[71] Sriram Ganeshan, R. Ramírez, and M. V. Fernández-Serra. Simulation of quantum zero-point effects in water using a frequency-dependent thermostat. *Phys. Rev. B*, 87:134207, 2013.

[72] C. Zhang, J. Wu, G. Galli, and F. Gygi. Structural and vibrational properties of liquid water from van der waals density functionals. *J. Chem. Theory. Comput.*, 7 (10):3054–3061, 2011.

[73] Éamonn D. Murray and Giulia Galli. Dispersion interactions and vibrational effects in ice as a function of pressure: A first principles study. *Phys. Rev. Lett.*, 108:105502–105507, 2012.

[74] P. H. Gammon, H. Klefte, and M. J. Clouter. Elastic constants of ice samples by brillouin spectroscopy. *The Journal of Physical Chemistry*, 87:4025–4029, 1983.

[75] S. M. Jackson and R. W. Whitworth. Evidence for ferroelectric ordering of ice ih. *J. Chem. Phys.*, 103:7647–7648, 1995.

[76] Christina M. B. Line and R. W. Whitworth. A high resolution neutron powder diffraction study of D_2O ice xi. *J. Chem. Phys.*, 104:10008–10013, 1996.

[77] S. M. Jackson, V. M. Nield, R. W. Whitworth, M. Oguro, and C. C. Wilson. Single-crystal neutron diffraction studies of the structure of ice xi. *J. Phys. Chem. B*, 101:6142–6145, 1997.

[78] Susan M. Jackson and R. W. Whitworth. Thermally-stimulated depolarization studies of the ice xi-ice ih phase transition. *J. Phys. Chem. B*, 101:6177–6179, 1997.

[79] Steven W. Rick. Simulations of proton order and disorder in ice ih. *J. Chem. Phys.*, 122:094504–094510, 2005.

[80] V. Buch, P. Sandler, and J. Sadlej. Simulations of H_2O solid, liquid, and clusters, with an emphasis on ferroelectric ordering transition in hexagonal ice. *J. Phys. Chem. B*, 102:8641–8653, 1998.

[81] Ding Pan, Li-Min Liu, Gareth A. Tribello, Ben Slater, Angelos Michaelides, and Enge Wang. Surface energy and surface proton order of ice ih. *Phys. Rev. Lett.*, 101:155703–155707, 2008.

[82] Ding Pan, Li-Min Liu, Gareth A. Tribello, Ben Slater, Angelos Michaelides, and Enge Wang. Surface energy and surface proton order of ice ih basal and prism surfaces. *J. Phys. Condens. Matter*, 22: 074209–074220, 2010.

[83] Charles Kittel. *Introduction ot Solid State Physics.* John Wiley & Sons, Inc., 2005.

[84] Kyuho Lee, Éamonn D. Murray, Lingzhu Kong, Bengt I. Lundqvist, and David C. Langreth. Higher-accuracy van der waals density functional. *Phys. Rev. B*, 82:081101, 2010.

[85] Luis A. Báez and Paulette Clancy. Phase equilibria in extended simple point charge ice water systems. *J. Chem. Phys.*, 103:9744–9755, 1995.

[86] Brendan W. Arbuckle and Paulette Clancy. Effects of the ewald sum on the free energy of the extended simple point charge model for water. *J. Chem. Phys.*, 116:5090–5098, 2002.

[87] Margot J. Vlot, Jan Huinink, and Jan P. van der Eerden. Free energy calculations on systems of rigid molecules: An application to the TIP4P model of H_2O. *J. Chem. Phys.*, 110:55–61, 1999.

[88] Hiroki Nada and Jan P. J. M. van der Eerden. An intermolecular potential model for the simulation of ice and water near the melting point: A six-site model of H_2O. *J. Chem. Phys.*, 118:7401–7413, 2003.

[89] E. Sanz, C. Vega, J. L. F. Abascal, and L. G. MacDowell. Tracing the phase diagram of the four-site water potential (tip4p). *J. Chem. Phys.*, 121:1165–1166, 2004.

[90] Steven W. Rick, Steven J. Stuart, and B. J. Berne. Dynamical fluctuating charge force fields: Application to liquid water. *The Journal of Chemical Physics*, 101(7):6141–6156, 1994.

[91] H. J. C. Berendsen, J. R. Grigera, and T. P. Straatsma. The Missing Term in Effective Pair Potentials. *J. Chem. Phys.*, 91:6269, 1987.

[92] W. L. Jorgensen, J. Chandrasekhar, J. D. Madura R. W. Impey, and M. L. Klein. Comparison of simple potential functions for simulating liquid water. *J. Chem. Phys.*, 79:926, 1983.

[93] M. W. Mahoney and W. L. Jorgensen. A five-site model for liquid water and the reproduction of the density anomaly by rigid, nonpolarizable potential functions. *J. Chem. Phys.*, 112:8910, 2000.

[94] F. H. Stillinger and A. Rahman. Revised central force potentials for water. *J. Chem. Phys.*, 68:666, 1978.

[95] William L. Jorgensen, Jayaraman Chandrasekhar, Jeffry D. Madura, Roger W. Impey, and Michael L. Klein. Comparison of simple potential functions for simulating liquid water. *J. Chem. Phys.*, 79:926, 1983.

[96] John Brodholt, Marco Sampoli, and Renzo Vallauri. Parameterizing polarizable intermolecular potentials for water with the ice 1h phase. *Mol. Phys.*, 85:81–90, 1995.

[97] J.R. Reimers and R.O. Watts. Intermolecular potential functions and the properties of water. *Chem. Phys.*, 64:95–114, 1982.

[98] R. E. Miller D. F. Coker and R. O. Watts. The infrared predissociation spectra of water clusters. *J. Chem. Phys.*, 82:3554, 1985.

[99] Satoru Kuwajima and Arieh Warshel. Incorporating electric polarizabilities in water-water interaction potentials. *J. Phys. Chem.*, 94: 460–466, 1990.

[100] Jer-Lai Kuo, Michael L. Klein, and Werner F. Kuhs. The effect of proton disorder on the structure of ice-ih: A theoretical study. *J. Chem. Phys.*, 123:134505–134511, 2005.

[101] Sherwin J. Singer, Jer-Lai Kuo, Tomas K. Hirsch, Chris Knight, Lars Ojamae, and Michael L. Klein. Hydrogen-bond topology and the ice vii/viii and ice ih/xi proton-ordering phase transitions. *Phys. Rev. Lett.*, 94:135701–135705, 2005.

[102] Chris Knight, Sherwin J. Singer, Jer-Lai Kuo, Tomas K. Hirsch, Lars Ojamae, and Michael L. Klein. Hydrogen bond topology and the ice vii/viii and ih/xi proton ordering phase transitions. *Phys. Rev. E*, 73: 056113–056127, 2006.

[103] Mandes Schönherr, Ben Slater, Jürg Hutter, and Joost VandeVondele. Dielectric properties of water ice, the ice ih/xi phase transition and an assessment of dft. *J. Phys. Chem. B*, 118:590–596, 2014.

[104] Paul J. Wooldridge and J. Paul Devlin. Proton trapping and defect energetics in ice from ft-ir monitoring of photoinduced isotopic exchange of isolated D_2O. *J. Chem. Phys.*, 88:3086–3091, 1988.

[105] Hiroshi Suga. A facet of recent ice sciences. *Thermochimica Acta*, 300: 117–126, 1997.

[106] Hiroshi Suga. Ultra-slow relaxation in ice and related substances. *Proc. Japan Acad. Ser. B*, 81:349–362, 2005.

[107] M. Blackman and N. D. Lisgarten. Electron diffraction investigation into the cubic and other forms of ice. *Advances in Physics*, 7:189–198, 1958.

[108] I. M. Svishchev and P. G. Kusalik. Crystallization of liquid water in a molecular dynamics simulation. *Phys. Rev. Lett.*, 239:349–353, 1994.

[109] J. E. Bertie, Calvert L. D., and E. Whalley. Transformations of ice ii, ice iii, and ice v at atmospheric pressure. *J. Chem. Phys.*, 38:840–846, 1963.

[110] J. E. Bertie and E. Whalley. Infrared spectra of ices ii, iii, and v in the range 4000 to 350 cm^{-1}. *J. Chem. Phys.*, 40:1646–1659, 1964.

[111] W. F Kuhs, D. V Bliss, and J. L. Finney. High resolution neutron powder diffraction study of ice ic. *Journal de Physique, Colloque C1*, 48:631, 636, 1987.

[112] E. D. Sloan and C. A. Koh. *Clathrate Hydrates*. CRC, Boca Raton, FL, 2008.

[113] E. Dendy Sloan Jr. Fundamental principles and applications of natural gas hydrates. *Nature (London)*, 426:353–359, 2003.

[114] Timothy S. Collett and Myung W. Lee. Reservoir characterization of marine and permafrost associated gas hydrate accumulations with downhole well logs. *Annals New York Academy of Sciences*, 912:51–64, 2006.

[115] Carolyn A. Koh. Towards a fundamental understanding of natural gas hydrates. *Chem. Soc. Rev.*, 31:157–167, 2002.

[116] Yu Lina, Wendy L. Maoa, and Ho kwang Mao. Storage of molecular hydrogen in an ammonia borane compound at high pressure. *PNAS*, 106:8113–8116, 2009.

[117] Peter G. Brewer, Gernot Friederich, Edward T. Peltzer, and Franklin M. Orr Jr. Direct experiments on the ocean disposal of fossil fuel CO_2. *Science*, 284:943–945, 1999.

[118] Amadeu K. Sum, Carolyn A. Koh, and E. Dendy Sloan. Clathrate hydrates: From laboratory science to engineering practice. *Ind. Eng. Chem. Res.*, 48:7457–7465, 2009.

[119] V.P. Shpakov, J.S. Tse, C.A. Tulk, B. Kvamme, and V.R. Belosludov. Elastic moduli calculation and instability in structure i methane clathrate hydrate. *Chemical Physics Letters*, 282:107,114, 1998.

[120] Luzhi Xua, Xu Wang, Liuxia Liuc, and Minghui Yang. First-principles investigation on the structural stability of methane and ethane clathrate hydrates. *Computational and Theoretical Chemistry*, 977:209–212, 2011.

[121] K. R. Ramya and Arun Venkatnathan. Stability and reactivity of methane clathrate hydrates: Insights from density functional theory. *J. Phys. Chem. A*, 116:7742–7745, 2012.

[122] Saman Alavi and John A. Ripmeester. Hydrogen-gas migration through clathrate hydrate cages. *Angew. Chem.*, 119:6214–6217, 2007.

[123] Xuemei Lang, Shuanshi Fan, and Yanhong Wang. Intensification of methane and hydrogen storage in clathrate hydrate and future prospect. *Journal of Natural Gas Chemistry*, 19:203–209, 2010.

[124] John S Tse. Vibrations of methane in structure i clathrate hydrate - an ab initio density functional molecular dynamics study. *Journal of Supramolecular Chemistry*, 2:429–433, 2002.

[125] Masaki Hiratsuka, Ryo Ohmura, Amadeu K. Sum, and Kenji Yasuoka. Molecular vibrations of methane molecules in the structure i clathrate hydrate from ab initio molecular dynamics simulation. *J. Chem. Phys.*, 136:044508, 2012.

[126] Niall J. English and John S. Tse. Mechanisms for thermal conduction in methane hydrate. *Phys. Rev. Lett.*, 103:015901, 2009.

[127] Guillermo Román-Pérez, Mohammed Moaied, Jose M. Soler, and Felix Yndurain. *Phys. Rev. Lett.*, 105:145901–145905, 2010.

[128] Qi Li, Brian Kolb, Guillermo Román-Pérez, José M. Soler, Felix Yndurain, Lingzhu Kong, D. C. Langreth, and T. Thonhauser. Ab initio energetics and kinetics study of H_2 and CH_4 in the si clathrate hydrate. *Phys. Rev. B*, 84:153103, 2011.

[129] Liam C. Jacobson, Waldemar Hujo, and Valeria Molinero. Thermodynamic stability and growth of guest-free clathrate hydrates: A low-density crystal phase of water. *J. Phys. Chem. B*, 113:10298–10307, 2009.

[130] Liam C. Jacobson, Waldemar Hujo, and Valeria Molinero. Amorphous precursors in the nucleation of clathrate hydrates. *J. Am. Chem. Soc.*, 132:11806–11811, 2010.

[131] Andrew H. Nguyen, Liam C. Jacobson, and Valeria Molinero. Structure of the clathrate/solution interface and mechanism of cross-nucleation of clathrate hydrates. *J. Phys. Chem. C*, 116:19828–19838, 2012.

[132] Brandon C. Knott, Valeria Molinero, Michael F. Doherty, and Baron Peters. Homogeneous nucleation of methane hydrates: Unrealistic under realistic conditions. *J. Am. Chem. Soc.*, 134:19544–19547, 2012.

[133] Yen-Tien Tung, Li-Jen Chen, Yan-Ping Chen, and Shiang-Tai Lin. Molecular dynamics study on the growth of structure i methane hydrate in aqueous solution of sodium chloride. *J. Phys. Chem. B*, 116: 14115–14125, 2012.

[134] Sapna Sarupria and Pablo G. Debenedetti. Homogeneous nucleation of methane hydrate in microsecond molecular dynamics simulations. *J. Phys. Chem. Lett.*, 3:2942–2947, 2012.

[135] A. Desmedt, L. Bedouret, E. Pefoute, M. Pouvreau, S. Say-Liang-Fat, and M. Alvarez. Energy landscape of clathrate hydrates. *Eur. Phys. J. Special Topics*, 213:103–127, 2012.

[136] E. Whalley, J. B. R. Heath, and D. W Davidson. Ice ix: An antiferroelectric phase related to ice iii. *J. Chem. Phys.*, 48:2362–2370, 1968.

[137] Londono J.D, W. F Kuhs, and J. L. Finney. Neutron diffraction studies of ices iii and ix on under-pressure and recovered samples. *J. Chem. Phys.*, 98:4878–4888–, 1993.

[138] W. F Kuhs, C Lobban, and J. L. Finney. Partial h-ordering in high pressure ices iii and v. *The Review of High Pressure Science and Technology*, 7:1141–1143, 1998.

[139] Robert W. Whitworth and Victor F. Petrenko. *"Physics of ice"*. Oxford University Press, 1999.

[140] B Kamb. Ice ii: A proton-ordered form of ice. *Acta Crystallographica*, 17:1437–1449, 1964.

[141] B Kamb, W. C. Hamilton, S. J. LaPlaca, and A Prakash. Ordered proton configuration of ice ii, from single-crystal neutron diffraction. *J. Chem. Phys.*, 55:1934–1945, 1971.

[142] Noboru Watanabe James D. Jorgensen, R. A. Beyerlein and T. G. Worlton. Structure of d2o ice viii from in situ powder neutron diffraction. *J. Chem. Phys.*, 81:3211, 1984.

[143] C. Vettier W. F. Kuhs, J. L. Finney and D. V. Bliss. Structure and hydrogen ordering in ices vi, vii, and viii by neutron powder diffraction. *J. Chem. Phys.*, 81:3612, 1984.

[144] Koichiro Umemoto and Renata M. Wentzcovitch. Amorphization in quenched ice viii: A first-principles study. *Phys. Rev. B*, 69:180311, 2004.

[145] Koichiro Umemoto and Renata M. Wentzcovitch. Theoretical study of the isostructural transformation in ice viii. *Phys. Rev. B*, 71:012102, 2005.

[146] R. J. Nelmes, J. S. Loveday, R. M. Wilson, J. M. Besson, Ph. Pruzan, S Klotz, and *et. al.* Neutron diffraction study of the structure of deuterated ice viii to 10 GPa. *Phys. Rev. Lett.*, 71:1192–1195, 1993.

[147] J. M. Besson, Ph. Pruzan, S Klotz, G Hamel, B Silvi, R. J. Nelmes, and *et. al.* Variation of interatomic distances in ice viii to 10 GPa. *Phys. Rev. B*, 49:12540–12550, 1994.

[148] R. J. Nelmes, J. S. Loveday, J. M. Besson, S Klotz, and G Hamel. Structure of ice vii and ice viii to 20 GPa. *The Review of High Pressure Science and Technology*, 7:1138–1140, 1998.

[149] Stefano de Gironcoli Koichiro Umemoto, Renata M. Wentzcovitch and Stefano Baroni. Order-disorder phase boundary between ice vii and viii obtained by first principles. *Chemical Physics Letters*, 499:236–240, 2010.

[150] A. I. Kolesnikov J-C. Li, C. Burnham and R. S. Eccleston. Neutron spectroscopy of ice viii in the region of 20-500 meV. *Phys. Rev. B*, 59: 9088, 1999.

[151] O. Mishima, Calvert L. D., and E. Whalley. 'melting ice' i at 77 K and 10 kbar: a new method of making amorphous solids. *Nature*, 310: 393–395, 1984.

[152] E. Whalley, D. D. Klug, M. A. Floriano, E. C. Svensson, and V. F. Sears. Recent work on high-density amorphous ice. *Journal de Physique, Colloque C1*, 48:429–434, 1987.

[153] Y. P. Handa, O Mishima, and E Whalley. High-density amorphous ice. iii. thermal properties. *J. Chem. Phys.*, 84:2766–2770, 1986.

[154] E. Mayer and P Brüggeller. Vitrification of pure liquid water by high pressure jet freezing. *Nature*, 298:715–718, 1982.

[155] A. Hallbrucker, E. Mayer, and G. P. Johari. The heat capacity and glass transition of hyperquenched glassy water. *Philosophical Magazine B*, 60:179–187, 1989.

[156] P. Jenninkens and D. F. Blake. Structural transition in amorphous water ice and astrophysical implications. *Science*, 265:753–756, 1994.

[157] D. T. Bowron, J. L. Finney, A. Hallbrucker, I. Kohl, T. Loerting, E. Mayer, and A. K. Soper. The local and intermediate range structures of the five amorphous ices at 80 K and ambient pressure: A faber-ziman and bhatia-thornton analysis. *J. Chem. Phys.*, 125:194502, 20062.

[158] Kristian Berland and Per Hyldgaard. Exchange functional that tests the robustness of the plasmon description of the van der waals density functional. *Phys. Rev. B*, 89:035412, 2014.

[159] S.J. Callori, J. Gabel, D. Su, J. Sinsheimer, M.-V. Fernandez-Serra, and M. Dawber. Ferroelectric $PbTiO_3/SrRuO_3$ superlattices with broken inversion symmetry. *Phys. Rev. Lett.*, 109:067601, 2012.

Appendices

A Atomic Orbital Basis Sets

The SIESTA basis set input files, with information about the cutoff radii of the orbitals of each basis set used in this dissertation.

Double-ζ Polarized Basis (dζ+p):

```
%Block PAO.Basis
O 3 -0.24233
  n=2 0 2 E 23.36061 3.39721
      4.50769 2.64066
      1.00000 1.00000
  n=2 1 2 E 2.78334 5.14253
      6.14996 2.59356
      1.00000 1.00000
  n=3 2 1 E 63.98188 0.16104
      3.54403
      1.00000
H 2 0.46527
  n=1 0 2 E 99.93138 2.59932
      4.20357 1.84463
      1.00000 1.00000
  n=2 1 1 E 24.56504 2.20231
      3.52816
      1.00000
%EndBlock PAO.Basis
```

Triple-ζ Polarized Basis (tζ+p):

```
%Block PAO.Basis
O 3 -0.18361
  n=2 0 3 E 50.06241 5.0
      7.0 4.0 2.4
      1.00000 1.00000 1.0
  n=2 1 3 E 10.0 6.0
      7.0 4.0 2.2
```

```
      1.00000 1.00000 1.0
  n=3 2 1 E 50.0 0.0
      6.0
      1.00000
H 2 0.94703
  n=1 0 3 E 50.0 6.0
      7.0 4.0 2.0
      1.00000 1.00000 1.0
  n=2 1 1 E 1000.0 0.0
      6.0
      1.00000
%EndBlock PAO.Basis
```

Double-ζ Double Polarized Basis (dζ+dp):

```
%Block PAO.Basis
O 3
  n=2 0 2 E 50.0 7.5
      8.0 2.7
  n=2 1 2 E 10.0 8.3
      8.5 2.6
  n=3 2 1 E 40.0 8.3 Q 6.8 0.22
      8.5
H 2
  n=1 0 2 E 50.0 8.3
      8.5 2.2
  n=2 1 1 E 20.0 7.8 Q 6.5 0.9
      8.0
%EndBlock PAO.Basis
```

Quadrupole-ζ Double Polarized Basis (qζ+dp):

```
%Block PAO.Basis
O 3
  n=2 0 4 E 50.0 8.0
```

```
      10.0 5.0 3.5 2.0
  n=2 1 4 E 10.0 8.0
      10.0 5.0 3.5 2.0
  n=3 2 2 E 40.0 9.0 Q 6.0
      10.0 2.2
H 2
  n=1 0 4 E 50.0 8.0
      10.0 5.0 3.5 2.0
  n=2 1 2 E 50.0 9.0 Q 3.5
      10.0 2.0
%EndBlock PAO.Basis
```

B Coordinates of Ice Structures

The coordinates and lattice vectors of the crystalline ice structures are given in this section. These are relaxed configurations obtained with the initial selection of basis sets, and they provide a good starting point for calculations with these structures.

Table 19: Coordinates and lattice vectors of ice structures.

ice IX				ice Ih			
	0.000000	4.440000	0.000000		13.320000	0.000000	0.000000
	3.845153	2.220000	0.000000		0.000000	15.380611	0.000000
	0.000000	0.000000	7.230000		0.000000	0.000000	14.480000
O	0.037408	-0.065154	0.166902	O	-0.032649	2.602335	0.501545
H	0.981330	-0.094337	0.496610	H	-0.009003	2.634055	1.501072
H	-0.409000	-0.897461	0.496412	H	0.009681	3.545100	0.171201
O	2.601639	-0.066362	1.065865	O	2.252376	1.271024	4.078566
H	3.082069	-0.899478	0.790754	H	2.256987	1.231584	5.078058
H	2.587135	-0.041233	2.065395	H	2.263922	0.327190	3.747496
O	2.526048	0.065181	3.781947	O	2.168166	1.291769	-0.419371
H	1.582116	0.094286	4.111687	H	1.353824	1.742801	-0.054449
H	2.972390	0.897554	4.111409	H	2.156310	0.343752	-0.100381
O	-0.038093	0.066459	4.680771	O	0.025690	2.581576	3.219588
H	-0.023739	0.041281	5.680321	H	0.844906	2.108364	3.543923
H	-0.518736	0.899452	4.405643	H	0.070424	3.517829	3.570601
Clathrate				O	0.050589	5.140613	4.109920
	11.680000	0.000000	0.000000	H	0.879160	5.616982	3.813182
	0.000000	11.680000	0.000000	H	0.038075	5.155849	5.109948
	0.000000	0.000000	11.680000	O	2.239104	6.449679	0.456563
O	2.901512	0.077849	5.825032	H	2.247145	6.450493	1.456446
O	5.836069	2.932283	-0.037540	H	2.231600	7.407989	0.168340
O	-0.028056	5.852349	2.897311	O	2.255691	6.415069	3.183515
O	2.145925	2.184956	2.165205	H	3.091313	5.972608	3.509419
O	-2.150960	-2.114181	2.083479	H	2.264413	7.355831	3.523852
O	-2.154567	2.173754	-2.168953	O	0.038804	5.145219	-0.470021
O	2.107971	-2.105301	-2.158584	H	0.857153	5.633266	-0.166702
O	-2.164093	-2.102020	-2.179754	H	0.046155	5.123852	-1.470000
O	2.139071	2.166517	-2.154121	O	4.397347	2.595789	0.431834
O	2.126815	-2.095798	2.135684	H	3.569191	2.138973	0.107208
O	-2.156563	2.167529	2.118606	H	4.377495	3.533106	0.082758
O	-0.009964	3.620790	1.342617	O	6.665369	1.302818	4.076357
O	0.005482	-3.608238	1.333891	H	5.865636	1.772786	3.701353

O	-0.009524	3.632539	-1.388949	H	7.473941	1.796954	3.756409
O	-0.037866	-3.583352	-1.385974	O	6.620931	1.289402	-0.428161
O	1.347150	0.031561	3.609423	H	5.792270	1.753903	-0.115031
O	1.346498	0.044276	-3.630502	H	6.587304	0.356316	-0.067270
O	-1.382376	0.019114	3.573269	O	4.450297	2.579413	3.149120
O	-1.380085	0.031756	-3.637048	H	3.639899	2.095493	3.481053
O	3.602299	1.407776	-0.002995	H	4.398614	2.582664	2.149928
O	-3.618209	1.386922	-0.031990	O	4.482198	5.136016	4.085886
O	3.587680	-1.341313	-0.026879	H	4.485307	4.201068	3.730405
O	-3.645296	-1.330509	-0.044141	H	5.303800	5.589749	3.741076
H	-2.730806	-2.688006	2.665821	O	6.674409	6.424800	0.451272
H	2.675411	-2.698075	-2.734096	H	5.871853	5.942437	0.099029
H	-0.058689	5.036779	2.320222	H	7.483188	5.927501	0.136331
H	2.311890	0.094820	5.017415	O	6.693838	6.434513	3.170666
H	4.997122	2.384541	-0.046199	H	6.674790	6.459328	2.171040
H	-0.843926	5.850215	3.475257	H	6.695982	7.380941	3.494488
H	5.840235	3.969738	1.327264	O	4.447439	5.159212	-0.465017
H	3.490198	0.885478	5.788013	H	3.638713	5.652548	-0.142758
H	-0.022620	4.468281	-1.936670	H	4.412353	5.161277	-1.464746
H	-4.493491	1.870065	-0.042628	O	8.844929	2.555429	0.479547
H	0.001656	-4.439845	1.888806	H	8.015300	2.085220	0.176861
H	-0.023231	-4.450993	-1.881979	H	8.842827	2.547076	1.479856
H	1.885688	0.055394	-4.472606	O	11.112833	1.307687	4.091998
H	-1.923267	-0.001952	4.413389	H	11.106785	1.293909	5.092573
H	-0.013199	3.717868	0.348663	H	11.944143	1.787197	3.808265
H	-0.013521	-3.756369	-0.403980	O	11.086030	1.315849	-0.427799
H	0.352654	0.005221	3.697337	H	10.266436	1.776130	-0.085080
H	-0.385224	0.023659	-3.726896	H	11.873133	1.820143	-0.071732
H	-3.780948	0.401915	-0.029844	O	8.894341	2.583182	3.192754
H	3.664728	-0.346285	-0.034166	H	9.722197	2.137061	3.534989
H	-0.814339	3.104885	-1.663746	H	8.921037	3.532017	3.508051
H	1.620386	-0.775673	-3.125682	O	8.918763	5.157661	4.058186
H	-1.648484	-0.790896	3.047370	H	8.121113	5.653715	3.713443
H	3.060677	1.665119	0.797722	H	9.731637	5.626962	3.713165
H	3.034625	-1.592611	-0.823496	O	11.134008	6.405161	0.439446
H	-3.115603	-1.620858	0.754818	H	11.120748	7.347872	0.105848
H	-0.813399	3.070092	1.574975	H	11.962021	5.976648	0.076067
H	-1.620408	-0.773055	-3.091152	O	11.160541	6.405250	3.156567
H	1.611826	-0.772341	3.071870	H	11.189160	6.388138	2.156741
H	3.047096	1.672080	-0.794097	H	11.981889	5.938907	3.485662
H	1.344197	2.696979	1.852525	O	8.895630	5.120537	-0.419919
H	-1.370590	-2.677993	1.811747	H	8.897595	4.182705	-0.072343
H	1.328097	-2.658029	-1.864244	H	9.730984	5.564882	-0.095858
H	1.810864	1.404904	2.695234	O	-0.026149	10.289555	0.428910
H	-1.857517	1.371718	-2.690555	H	-0.063067	11.222685	0.068685

H	-2.706872	1.844011	-1.402321	H	-0.846140	9.822957	0.095745
H	-1.403229	-2.658624	-1.844059	O	2.232974	8.984107	4.071877
H	1.331937	2.692852	-1.879696	H	1.423676	9.471145	3.742763
H	-1.878784	1.360059	2.643494	H	2.199564	8.987029	5.071345
H	1.815852	1.390192	-2.698994	O	2.222299	9.017266	-0.418024
H	2.669505	-1.803542	1.346849	H	1.412903	9.509001	-0.095653
H	-2.707301	1.843359	1.349030	H	3.027550	9.495505	-0.067016
H	2.722514	-2.678944	2.691164	O	0.031685	10.289305	3.146830
H	0.807704	-3.081829	1.617616	H	0.004969	10.326620	2.147355
O	9.424776	5.919888	4.438480	H	0.034245	11.232657	3.478497
O	2.205084	5.872456	4.466003	O	0.040276	12.839345	4.104876
O	9.461059	5.890271	7.176535	H	0.870654	13.296305	3.784671
O	2.226050	5.875291	7.195341	H	0.072497	12.829055	5.104341
O	5.806386	7.238222	2.198656	O	2.189569	14.087658	0.429318
O	5.831868	7.239235	9.385921	H	1.379884	13.616074	0.079819
O	5.843160	4.521603	2.161545	H	2.988032	13.598165	0.076979
O	5.851084	4.504503	9.430142	O	2.254530	14.095081	3.150236
O	7.163358	9.520141	5.802618	H	2.242459	14.069671	2.150445
O	7.199556	2.281800	5.796332	H	3.082646	13.616985	3.445456
O	4.436118	9.505348	5.815469	O	-0.046454	12.838696	-0.485858
O	4.473969	2.291031	5.810191	H	-0.855526	13.329059	-0.160883
O	7.945081	8.059062	3.652675	H	-0.062221	12.866246	-1.485922
O	3.710402	3.763834	3.674729	O	4.464823	10.262531	0.483391
O	8.002977	3.742634	7.943781	H	5.267308	9.770360	0.145334
O	3.675788	8.035230	7.962303	H	4.500170	10.234578	1.482725
O	3.688416	3.732930	7.973390	O	6.700216	8.987570	4.111016
O	7.969406	8.044799	7.921941	H	7.523980	9.453113	3.786189
O	3.676520	8.014930	3.688457	H	6.737698	8.984588	5.110851
O	7.978212	3.756286	3.651118	O	6.652915	8.972270	-0.488208
O	8.741839	0.044075	5.811433	H	6.667052	8.020559	-0.179661
O	5.810210	8.768343	-0.049485	H	6.627093	8.953964	-1.487978
O	-0.006396	5.875894	8.740601	O	4.477985	10.250162	3.200690
H	9.500130	5.918848	5.435220	H	3.666736	9.773222	3.539518
H	1.365091	5.840919	3.926197	H	5.278938	9.772907	3.563450
H	5.830114	6.242133	9.462045	O	4.463096	12.822146	4.069193
H	6.169759	9.618789	5.820874	H	4.492920	11.875576	3.745661
H	2.113596	5.852879	6.203106	H	5.295977	13.272948	3.747597
H	5.792555	7.721137	1.324424	O	6.621982	14.118701	0.482821
H	7.743592	1.443084	5.793156	H	6.622232	14.101288	1.483247
H	8.875935	6.719109	4.191944	H	5.807801	13.628912	0.171257
H	8.923340	5.086237	7.439374	O	6.691098	14.109096	3.194979
H	7.149046	7.751344	3.131379	H	7.526139	13.659517	3.512289
H	5.028720	7.486125	8.840919	H	6.708736	15.051358	3.529926
H	6.643337	4.226474	8.884822	O	4.420369	12.814017	-0.446954
H	4.239713	2.835224	5.002179	H	4.447635	11.868941	-0.120054

H	2.757163	5.061227	7.439113	H	4.457772	12.781049	-1.446044
H	8.914862	6.681392	7.454647	O	8.854068	10.267248	0.442457
H	2.749597	5.084640	4.171920	H	8.040080	9.814007	0.078595
H	5.052104	4.223584	8.895394	H	8.835081	11.216892	0.129298
H	4.170076	8.970483	5.012185	O	11.140601	8.973763	4.039520
H	7.490057	2.807748	4.995630	H	11.183096	8.032886	3.701508
H	7.412231	8.983608	6.611084	H	11.954057	9.444483	3.697835
H	4.485472	4.043961	3.106718	O	11.078343	8.980831	-0.447042
H	3.144604	7.252554	7.633581	H	10.252832	9.455734	-0.141017
H	7.608445	8.592917	4.429611	H	11.048393	8.974351	-1.447191
H	7.708995	3.194726	7.158995	O	8.912023	10.250767	3.157964
H	8.520308	4.542792	3.947738	H	8.894197	10.238766	2.157933
H	7.193796	7.729208	8.471686	H	9.740450	9.767859	3.443865
H	4.442625	7.676983	3.141429	O	8.928727	12.820398	4.046120
H	3.990713	3.192172	7.186712	H	8.953473	11.881930	3.700544
H	8.564861	3.138763	8.512808	H	9.755671	13.277605	3.718090
H	3.110774	3.131602	8.529058	O	11.082041	14.135504	0.470126
H	8.531894	8.612088	8.527582	H	11.123936	14.150739	1.469457
H	3.136210	7.218814	3.967107	H	11.090023	15.089338	0.166665
H	5.825811	6.253888	2.033148	O	11.153624	14.125919	3.188781
H	5.466397	2.180302	5.792894	H	11.977569	13.683135	3.543590
H	8.574649	3.182606	3.086663	H	11.159966	15.065319	3.533082
H	6.654847	4.242995	2.677060	O	8.860518	12.850114	-0.415940
H	3.135047	3.175173	3.102411	H	8.049735	13.327073	-0.077668
H	3.898136	10.346904	5.789965	H	9.657967	13.344552	-0.068090
H	3.947172	8.568585	7.158660	O	-0.017697	2.537408	7.663125
H	-4.477380	-1.883585	-0.045626	H	0.789944	2.049208	7.331573
H	-2.694996	-1.813028	-1.380601	H	-0.822428	2.046169	7.329145
H	9.320770	0.011381	6.625452	O	2.188003	1.292966	11.343950
H	8.142135	-0.756295	5.838317	H	1.361164	1.739055	11.001093
H	0.788522	5.870739	8.133656	H	2.139617	1.310419	12.342893
H	-0.813042	5.886478	8.146174	O	2.226687	1.263885	6.798060
H	5.786389	8.196601	-0.869751	H	3.029378	1.745781	7.150320
H	5.003256	9.358510	-0.073107	H	2.267783	0.330926	7.157047
H	5.825786	3.502094	-0.861691	O	-0.032083	2.533215	10.381155
C	-0.042351	-0.080489	0.012287	H	-0.044617	2.505404	9.381012
H	-0.288767	-1.147627	-0.016247	H	-0.862258	2.076636	10.701817
H	0.318642	0.185555	1.012015	O	-0.019390	5.089844	11.294029
H	-0.936163	0.508740	-0.222400	H	-0.039392	4.153938	10.940491
H	0.739606	0.133563	-0.725498	H	-0.848019	5.540273	10.960480
C	2.870182	5.688782	-0.178774	O	2.203242	6.405785	7.720347
H	3.397708	4.804915	0.203460	H	2.183533	6.411484	8.720546
H	3.571388	6.530823	-0.246718	H	1.374488	5.931463	7.421137
H	2.049149	5.950460	0.501353	O	2.192908	6.416535	10.439454
H	2.464129	5.469904	-1.175442	H	1.368196	5.947442	10.756662

C	8.714724	5.881324	-0.182637	H	2.155519	7.351201	10.794845
H	8.028718	5.057246	0.053077	O	-0.015941	5.126629	6.825458
H	9.215577	5.680899	-1.138906	H	-0.041528	4.177473	7.139183
H	9.467884	5.969042	0.611673	H	-0.845782	5.576596	7.155988
H	8.147426	6.818626	-0.255729	O	4.413393	2.592672	7.720676
C	0.074279	8.739912	5.868273	H	4.418893	2.597250	8.720761
H	-0.117266	7.960008	5.119861	H	4.413511	3.544447	7.414191
H	0.950908	9.330171	5.570154	O	6.637719	1.255219	11.333807
H	0.261462	8.272162	6.843874	H	6.668865	0.309251	11.011651
H	-0.799349	9.401464	5.939627	H	6.628758	1.227532	12.334016
C	-0.056556	2.873094	5.723895	O	6.623946	1.306048	6.793881
H	-0.365942	1.836568	5.909037	H	6.607154	1.332169	5.793922
H	1.030097	2.910223	5.569722	H	5.809214	1.788396	7.115770
H	-0.324176	3.496281	6.587505	O	4.419557	2.546170	10.437361
H	-0.565963	3.253425	4.828209	H	3.607781	2.077853	10.787258
C	5.809269	-0.049876	2.854006	H	5.216335	2.047364	10.779241
H	5.788235	-0.998578	2.301424	O	4.424087	5.125111	11.296789
H	6.775552	0.055611	3.365215	H	3.592661	5.574759	10.969551
H	5.001823	-0.038529	3.597379	H	4.399500	4.176518	10.980044
H	5.674297	0.783941	2.152468	O	6.694450	6.385527	7.691773
C	5.699233	-0.040060	8.714631	H	5.871391	5.932708	7.348748
H	6.026708	-1.046524	9.008120	H	7.479082	5.876716	7.335956
H	6.455452	0.414990	8.061299	O	6.633801	6.417127	10.407103
H	5.568891	0.577877	9.612253	H	5.809898	5.930680	10.700137
H	4.744880	-0.108640	8.175597	H	6.652261	6.377378	9.407504
C	5.822667	5.826597	5.754443	O	4.434876	5.155031	6.804808
H	5.911314	4.894220	6.323809	H	4.429599	5.154722	5.804987
H	6.579750	6.540167	6.099487	H	3.603725	5.618484	7.112096
H	4.823762	6.251672	5.905064	O	8.868553	2.534018	7.712082
H	5.975502	5.620302	4.689072	H	8.030735	2.088608	7.394343
ice Ic				H	8.829008	2.553091	8.711211
	0.000000	3.140000	3.140000	O	11.055419	1.300701	11.329116
	3.140000	0.000000	3.140000	H	10.234289	1.788541	11.030283
	3.140000	3.140000	0.000000	H	11.059887	1.328254	12.328885
O	-0.001706	-0.001705	-0.021491	O	11.072610	1.245029	6.800576
H	0.565225	0.565225	0.576866	H	10.248493	1.683619	7.160817
H	-0.569160	-0.569160	0.575928	H	11.082205	0.304424	7.141032
O	1.568398	1.568399	1.549257	O	8.838155	2.586808	10.435544
H	1.001524	2.136099	2.147069	H	8.027545	2.116079	10.783743
H	2.136099	1.001524	2.147069	H	8.804194	3.525394	10.780918
ice IX				O	8.844418	5.143523	11.345103
	6.600000	0.000000	0.000000	H	8.019694	5.620956	11.041857
	0.000000	6.600000	0.000000	H	8.848543	5.149065	12.345536
	0.000000	0.000000	6.600000	O	11.073527	6.414941	7.700884
O	2.367953	0.825109	-0.763825	H	10.264767	5.950925	7.339086

H	1.519561	1.227186	-1.105580	H	11.068552	7.348456	7.342500
H	2.641754	1.458006	-0.044041	O	11.080711	6.387409	10.420123
O	-0.291169	-2.255919	1.481233	H	10.249381	5.933663	10.741746
H	0.411315	-2.115332	0.784851	H	11.045555	6.391320	9.420622
H	0.183858	-2.029106	2.327730	O	8.892181	5.090002	6.769010
O	-2.082156	1.818274	0.139800	H	8.903660	5.084365	5.768544
H	-2.228062	0.833620	0.225942	H	8.889767	4.140209	7.081496
H	-2.059841	2.125337	1.087884	O	0.024938	10.222916	7.712068
O	-2.529386	-0.805900	0.819752	H	0.856852	9.749822	7.421239
H	-1.681056	-1.207805	1.161820	H	0.012710	10.218433	8.712319
H	-2.802847	-1.438815	0.099849	O	2.171406	8.978289	11.339863
O	0.129792	2.275684	-1.424502	H	1.343190	9.456705	11.045363
H	-0.572916	2.134599	-0.728398	H	2.187537	9.015501	12.339218
H	-0.344806	2.048909	-2.271205	O	2.239207	8.957356	6.788178
O	1.920775	-1.799539	-0.083832	H	2.246861	8.020917	7.139899
H	2.066704	-0.814921	-0.169961	H	3.075187	9.405587	7.105276
H	1.898375	-2.106522	-1.031917	O	-0.040601	10.257211	10.428741
O	3.230223	0.146758	2.618392	H	-0.061450	11.205869	10.744280
H	3.051225	1.049242	2.231471	H	-0.870030	9.807749	10.761256
H	3.904734	-0.277097	2.021034	O	-0.014404	12.840884	11.278117
O	-1.253186	-0.012785	4.067380	H	0.805308	13.317640	10.960717
H	-0.352939	-0.430704	3.962017	H	-0.808311	13.346911	10.940450
H	-1.907803	-0.762079	4.028890	O	2.259620	14.089022	7.723083
O	0.359111	3.796956	1.805690	H	2.289024	14.090276	8.723201
H	-0.378414	3.287689	2.244835	H	3.085913	13.625138	7.402411
H	-0.073393	4.345483	1.096108	O	2.245237	14.108248	10.440996
O	-3.391679	-0.127127	-2.562879	H	3.071693	13.658926	10.780742
H	-3.212477	-1.029535	-2.175966	H	2.246992	15.043923	10.794176
H	-4.066296	0.296542	-1.965494	O	0.046048	12.792912	6.829166
O	1.092421	0.032353	-4.011660	H	0.065773	11.850043	7.163171
H	0.192128	0.450128	-3.906205	H	0.868833	13.240734	7.180400
H	1.746938	0.781730	-3.972603	O	4.465123	10.244131	7.669642
O	-0.519755	-3.777528	-1.749754	H	5.302385	9.790933	7.364076
H	0.217755	-3.268295	-2.189062	H	4.496209	11.183329	7.325316
H	-0.087344	-4.326232	-1.040248	O	6.605886	8.985667	11.270800
ice II				H	6.585780	8.044119	10.931663
	7.660000	0.000000	0.000000	H	5.774238	9.429419	10.936374
	-3.005302	7.045833	0.000000	O	6.713346	8.963845	6.828616
	-3.005302	-4.549137	5.380438	H	6.738911	8.019333	7.156625
O	2.367953	0.825109	-0.763825	H	7.536430	9.422548	7.163774
H	1.519561	1.227186	-1.105580	O	4.376448	10.257891	10.382769
H	2.641754	1.458006	-0.044041	H	3.549102	9.793704	10.697989
O	-0.291169	-2.255919	1.481233	H	4.375265	10.242821	9.382531
H	0.411315	-2.115332	0.784851	O	4.471574	12.811688	11.314839
H	0.183858	-2.029106	2.327730	H	4.446146	11.879416	10.953927

O	-2.082156	1.818274	0.139800
H	-2.228062	0.833620	0.225942
H	-2.059841	2.125337	1.087884
O	-2.529386	-0.805900	0.819752
H	-1.681056	-1.207805	1.161820
H	-2.802847	-1.438815	0.099849
O	0.129792	2.275684	-1.424502
H	-0.572916	2.134599	-0.728398
H	-0.344806	2.048909	-2.271205
O	1.920775	-1.799539	-0.083832
H	2.066704	-0.814921	-0.169961
H	1.898375	-2.106522	-1.031917
O	3.230223	0.146758	2.618392
H	3.051225	1.049242	2.231471
H	3.904734	-0.277097	2.021034
O	-1.253186	-0.012785	4.067380
H	-0.352939	-0.430704	3.962017
H	-1.907803	-0.762079	4.028890
O	0.359111	3.796956	1.805690
H	-0.378414	3.287689	2.244835
H	-0.073393	4.345483	1.096108
O	-3.391679	-0.127127	-2.562879
H	-3.212477	-1.029535	-2.175966
H	-4.066296	0.296542	-1.965494
O	1.092421	0.032353	-4.011660
H	0.192128	0.450128	-3.906205
H	1.746938	0.781730	-3.972603
O	-0.519755	-3.777528	-1.749754
H	0.217755	-3.268295	-2.189062
H	-0.087344	-4.326232	-1.040248
ice VIII			
	4.770000	0.000000	0.000000
	0.000000	4.770000	0.000000
	0.000000	0.000000	6.900000
H	-0.098339	2.592267	5.267611
O	-0.098518	3.380241	5.868872
H	-0.098227	4.168129	5.267489
H	1.498694	3.380243	0.092218
O	2.286695	3.380413	0.693464
H	3.074609	3.380129	0.092076
H	2.286691	2.592256	4.529108
O	2.286822	3.380304	3.927908
H	2.286583	4.168179	4.529363
H	2.286578	0.207315	1.817444
O	2.286759	0.995168	2.418884
H	5.301490	13.241796	10.957707
O	6.687663	14.114991	7.680215
H	7.515045	13.683922	7.318434
H	6.673548	15.055777	7.341336
O	6.694567	14.074313	10.401652
H	6.729173	14.084504	9.402045
H	7.513394	13.598643	10.723294
O	4.474580	12.813877	6.790149
H	4.484110	12.828895	5.789786
H	5.300377	13.292098	7.091945
O	8.927010	10.283718	7.694317
H	9.747808	9.835726	7.338682
H	8.929970	11.218439	7.337745
O	11.065007	8.954952	11.315838
H	11.055569	8.014262	10.975587
H	10.234877	9.393619	10.969105
O	11.119471	8.976123	6.765579
H	11.156309	8.983758	5.766349
H	11.952542	9.422442	7.093281
O	8.853848	10.237347	10.409863
H	8.010152	9.774234	10.683610
H	8.870094	10.257975	9.410060
O	8.900880	12.790242	11.346439
H	8.882688	11.838345	11.040803
H	8.887006	12.789599	12.346406
O	11.132341	14.066321	7.704106
H	11.121005	14.077780	8.704345
H	11.966193	13.591796	7.420805
O	11.074734	14.128086	10.414166
H	10.277603	13.640768	10.770787
H	11.029697	15.063781	10.765995
O	8.900071	12.838727	6.763715
H	8.936667	12.835863	5.763773
H	9.735068	13.285342	7.087026

H	2.286690	1.783165	1.817668	
H	-0.098218	0.207275	1.079291	
O	-0.098467	0.995209	0.477917	
H	-0.098335	1.783208	1.079186	
H	1.498740	0.995134	6.254029	
O	2.286642	0.995178	5.652692	
H	3.074518	0.995261	6.254074	
H	-0.886250	3.380130	2.804164	
O	-0.098428	3.380408	2.202701	
H	0.689527	3.380253	2.803957	
H	-0.886266	0.995312	3.542077	
H	0.689650	0.995201	3.542198	
O	-0.098348	0.995194	4.143454	

C Ongoing Projects: $PbTiO_3/H_2O$ Interfaces

The main focus of this dissertation has been understanding the structure of water. An accurate knowledge of the structure of water is important to understand how it interacts with other materials. One purpose of investigating how water interacts with different surfaces is to find a good material for cheap and efficient photocatalysis. It is known that TiO_2 is a good photocatalysis material, however this surface does not dissociate water unless there are impurities in the system. Presence of OH^- ions are crucial for water oxidation reaction. In this section, we are interested in ferroelectric $PbTiO_3$, which has a different structure and has bulk polarization. We perform a study to understand how we can control the dynamics of adsorption and dissociation of water on $PbTiO_3$ thin film surfaces by changing polarity. The first question that needs to be answered is how many layers of $PbTiO_3$ are needed to have a stable thin film. Once this is established, water is placed on the thin film and *ab initio* DFT molecular dynamics simulations are performed, both at the semi-local PBE and van der Waals level of approximation, with a recently developed vdW-DF-cx functional [158]. We are interested in understanding how changing the direction of polarity of the perovskite and changing the termination layer from TiO_2 to PbO, changes the structure and reactivity of water.

C.1 Structures

At room temperature, bulk $PbTiO_3$ has a tetragonal perovskite structure and is ferroelectric [14]. Ti and O atoms are displaced with respect to Pb atoms, and the displacement of the O atoms are larger than Ti atoms. This is a result of the ferroelectric distortions and leads to a net dipole moment in the bulk structure. Above 763 K, $PbTiO_3$ goes under a phase transition to the cubic structure [14].

We have performed two simulations with two different $PbTiO_3$ slab thicknesses of $2\sqrt{2}a \times 2\sqrt{2}a \times c$ and $2\sqrt{2}a \times 2\sqrt{2}a \times 2c$. This provides a stability check of having one or two layers of the slab. This configuration also provides both TiO_2 terminated and PbO terminated surfaces. In addition, we have also looked at these two configurations with $+\hat{z}$ and $-\hat{z}$ polarisation, resulting in four different molecular dynamics simulations run at the same time. Moreover, with the vdW-DF-cx functional, we have also included one

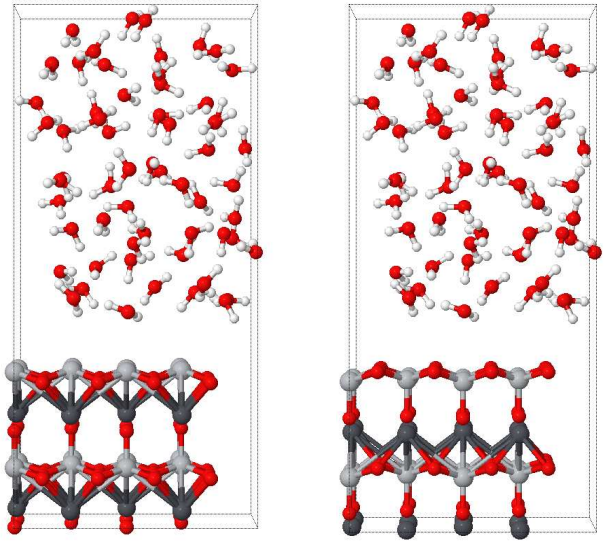

Figure 45: Initial conditions of the unit cell for simulations of $PbTiO_3$/water surfaces with $+\hat{z}$ polarisation on the left and $-\hat{z}$ polarisation on the right, as obtained with the PBE functional lattice parameters. Light grey atoms are Ti, dark grey atoms are Pb, red atoms are O and white atoms are H. The top layer of the slab is TiO_2 terminated, which is shown as directly interacting with the liquid water, and the bottom layer of the slab is PbO terminated, interacting with the liquid water as the periodic boundary conditions are applied.

and two layers of slab of the cubic structure configuration, to investigate the stability of the system without any polarisation.

Once the water is placed on the slab, periodic boundary conditions provides us to check TiO_2/water and PbO/water interactions simultaneously. We have placed liquid water of 15 Å thickness along the c axis. Depending on the functional, box size along the x-y axis varies, therefore, the systems have 59 H_2O molecules for simulations with the PBE functional, and 65 H_2O molecules for simulations with the vdW-DF-cx functional. Two of the initial configurations of the simulations are shown in Fig. 45 for two layered slab structure, while the other two configurations are one layered slab with the exact same water configuration.

C.2 Computational Details

We have performed *ab initio* molecular dynamics (AIMD) simulations as implemented in the SIESTA code. There are two sets of interface calculations: The first set of simulations were performed with PBE functional, with the same basis set and pseudopotentials as in Ref. [159] for Pb, Ti, O and H. The second set of simulations were performed with a recently developed vdW-DF-cx functional and we have switched to the dζ+dp basis sets for O and H atoms for this set of AIMD simulations. A real-space mesh cutoff of 500 Ry for the real space integrals, a force tolerance of 0.01 eV/Å and a density matrix tolerance of 10^{-4} electrons have been used for the structural relaxations to obtain the bulk lattice parameters of $PbTiO_3$. For the surface/water interactions, AIMD simulations were performed for an initial equilibration by means of temperature annealing to 330 K, with a time step of 0.5 fs. The simulations with PBE functional are annealed for 3.5 ps, while the ongoing simulations with vdW-DF-cx functional presented here are annealed for $\sim$ 1-1.5 ps depending on the system size.

C.3 Results

C.3.1 Lattice Parameters of Bulk $PbTiO_3$

The lattice parameters of bulk $PbTiO_3$ are obtained by calculating the electronic Kohn-Sham energy, E(V) of a unit cell of five atoms. The structure is relaxed for a fixed volume, and the lattice parameters are varied for several volumes. The optimal lattice parameters are selected for the volume that minimises the Kohn-Sham energy, E(V).

Table 20: Lattice parameters given in Å of bulk $PbTiO_3$ for PBE and vdW-DF-cx functionals and the corresponding tetragonality c/a. The experimental values are at room temperature and zero pressure, from Ref. [14].

XC	a	c	c/a
PBE	3.85	4.60	1.195
vdW-DF-cx	3.92	4.03	1.028
Expt.	3.9036(1)	4.1440(2)	1.0616

This structural relaxations are performed both by PBE and vdW-DF-cx functionals. As semi-local functional, PBE functional overestimates the

tetragonality of the system, by mainly overestimating the c lattice parameter, and slightly underestimating the a lattice parameter. When the non-local interactions are included, vdW-DF-cx functional gives a larger a lattice parameter, but decreases c lattice parameter substantially, such that the tetragonality of the system is comparable to the room temperature experimental results of Ref [14].

Our initial goal has been investigating how the structural properties of the liquid water under the influence of an external dipole, therefore the large dipole moment from the overestimated tetragonality of the PBE functional was desirable. However, once the simulations with the PBE functional started, we have observed structural deformations on the $PbTiO_3$ slab. Therefore, XC functional has been changed to obtain more realistic tetragonality of the slab structure, and the vdW-DF-cx functional has been selected for a better simulation of the liquid water, as it has been shown that vdW effects are important for the liquid structure. These lattice parameter results for the bulk shows that the inclusion of vdW effects also important for the structure of the slab.

C.3.2 Stability of the Slab with the PBE Functional

The four configurations of $PbTiO_3$ slab with water, with different slab thickness and polarisation direction, have been annealed to 330 K for 3.5 ps. Fig. 46 shows the configuration at the end of this simulation.

These results show that the one or two layers of $PbTiO_3$ slabs with the PBE functional are not stable. During the annealing process, they lose their crystal lattice structure completely, therefore making the analysis of the polarisation difficult. One of the reasons for this can be due to the overestimation of the tetragonality with the PBE functional. As mentioned before, to test the validity of this solution to the stability problem, we have stopped our simulations with this functional and switched to the vdW-DF-cx functional. Preliminary results with this functional will be provided in the following section.

However, already with these results, there are conclusions we can withdraw for these interfaces. As expected, TiO_2 terminated surface is highly interactive with the liquid water. There is molecular adsorption of water to the TiO_2 terminated surface in all four simulations. Moreover, there exists a dissociation event of a water molecule on the TiO_2 terminated surface, when the slab thickness is increased to two layers.

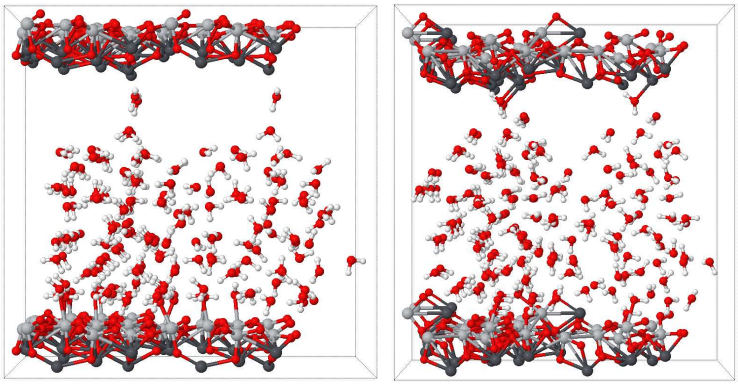

(a) 1 layer $PbTiO_3$/water.

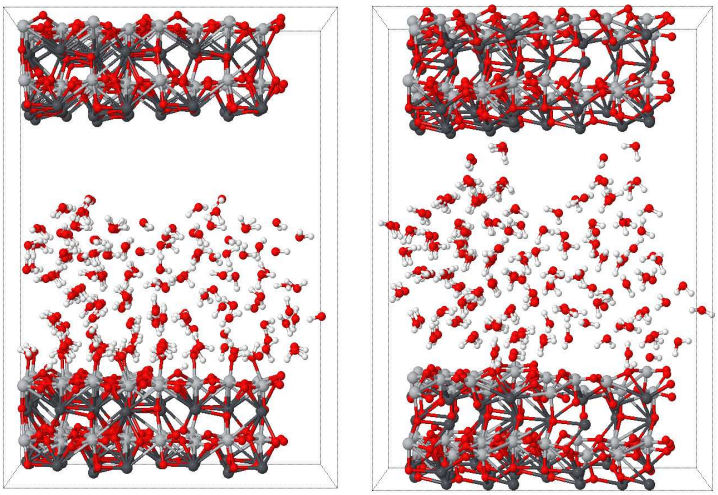

(b) 2 layers $PbTiO_3$/water.

Figure 46: The configuration of the slab/water interface at the end of 3.5 ps annealing with the PBE functional. The structures on the left are $+\hat{z}$ polarised and the structures on the right are $-\hat{z}$ polarised. The unit cell is repeated in +x and -y direction, and the slab is repeated once in +z direction to show the full interaction with the liquid water within the periodicity.

On the other hand, the PbO terminated surface are more hydrophobic than the TiO_2 terminated surface. There is a clear separation of the liquid water from the PbO surface, creating voids between the liquid and the PbO surface. This is most extreme when the slab is positively polarised with a thickness of 2 layers.

The structural instability of the slab and the existence of the separation between the surface and the liquid makes the analysis of the polarisation very difficult. Therefore, these simulations have been stopped at this point and the functional has been changed.

C.3.3 Simulations with the vdW-DF-cx Functional

Once the functional is changed to the vdW-DF-cx, the instability problem of $PbTiO_3$ slab is partially fixed. At this point, we have also decided to increase the number of configurations, and included one and two layers of slab with cubic symmetry, without any polarisation.

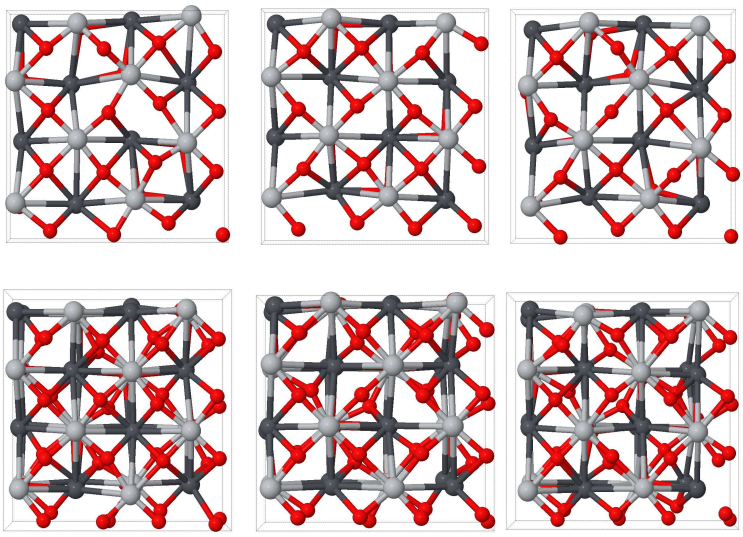

Figure 47: $PbTiO_3$ slab shown from the top, along x-y direction, simulated with 15 Å vacuum on top, at the last step of AIMD with annealing to 330 K for 2.5 ps. 1 layer of slabs are shown on top, and 2 layers of slabs are shown at the bottom. The cubic structure without polarisation on the right, $+\hat{z}$ polarisation in the middle, and $-\hat{z}$ polarisation on the right, as obtained with the vdW-DF-cx functional.

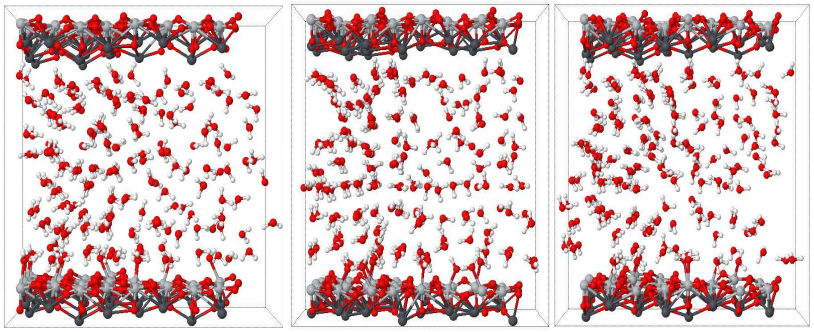

(a) 1 layer $PbTiO_3$/water.

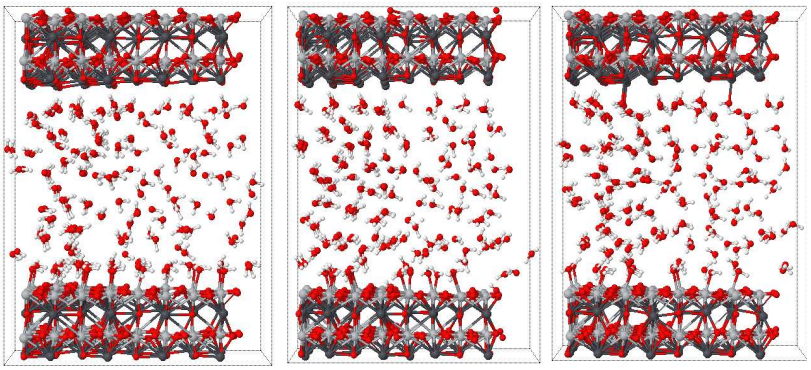

(b) 2 layers $PbTiO_3$/water.

Figure 48: The configuration of the slab/water interface with the vdW-DF-cx functional. The structures on the left are unpolarised cubic, the structures in the middle are $+\hat{z}$ polarised, and the structures on the right are $-\hat{z}$ polarised. The unit cell is repeated in +x and -y direction, and the slab is repeated once in +z direction to show the full interaction with the liquid water within the periodicity.

In addition, to check the stability of the slab, we have performed annealing of the slab only, with dipole corrections, with 15 Å vacuum instead of liquid water. The run time of these AIMD simulations of annealing to 330 K are 2.5 ps. Although lattice distortions are present during the annealing process, and the change from the crystal structure is highly reduced as compared to the PBE simulations. The configurations at the end of 2.5 ps, are given in Fig. 47.

Next, liquid water has been placed on these slabs, and the instability of the slab is again reduced with respect to the previous case. At the end of 1 ps, the separation of the liquid from PbO surface is reduced, but it is still more actively interacting with the TiO_2 terminated surface. So far, with run times vary depending on the system size. Cubic structure with 1 layer has 4216, with 2 layers has 2781, $+\hat{z}$ polarised structure with 1 layer has 3751, 2 layers has 2849, $-\hat{z}$ polarised structure with 1 layer has 4033, 2 layers has 2134 time steps, with step size of 0.5 fs. The configurations at the end of these time steps are also shown in Fig. 48. We aim to continue these equilibration runs at least up to the same time length of the PBE simulations, for a better comparison. However, these configurations already shows that water is not separated from the PbO surface any more, resolving the problem of having vacuum between the interfaces. And these results are in agreement with our conclusions from the PBE simulations. The majority of configuration of the water molecules on the PbO terminated surface are up/down, meaning that the H atoms are either pointing towards or away from the surface, in this case, they seem to point towards the surface. On the other hand, the majority of the water molecules on the TiO_2 surface are flat, meaning that the H atoms are parallel to the surface. On this surface, water molecules are adsorbed such that the O atoms of the water molecule are coordinated to the Ti atoms of the surface. Furthermore, there is a dissociation event of the water molecule, for the $+\hat{z}$ polarised surface, the adsorbed water molecule loses one of its H atom to the O atom of the TiO_2.

Up to these run times, the slab keeps its crystal structure, making it possible to analyse the interaction of water with the surfaces. However, all the conclusions presented before have been done by observations with visualisation tools. In order to quantify the interactions of water with the surface, the vibrational spectrum of the liquid water has been analysed. This is accomplished by separating the liquid into two sections, half interacting with the TiO_2 surface, and other half interacting with the PbO surface. Then, the vibrational spectrum is obtained by calculating the Fourier transformation of

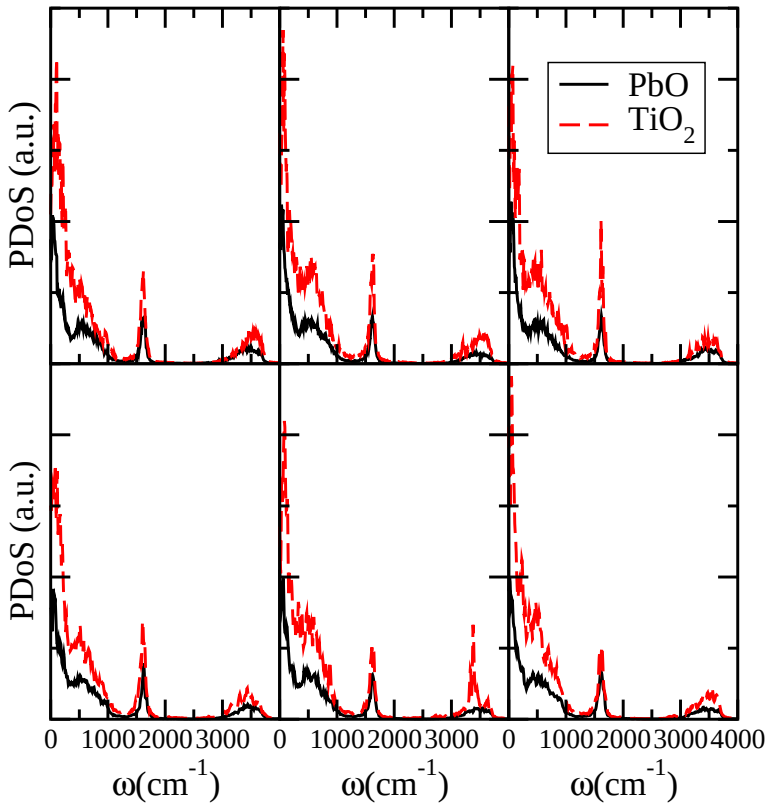

Figure 49: Projected vibrational density of states of liquid water interacting with the PbO terminated and TiO_2 terminated surfaces. 1 layer of slabs are shown on top, and 2 layers of slabs are shown at the bottom. The cubic structure without polarisation on the right, $+\hat{z}$ polarisation in the middle, and $-\hat{z}$ polarisation on the right, as obtained with the vdW-DF-cx functional.

the velocity-velocity autocorrelation function. With this method, we expect to see differences, especially in the stretching modes of the liquid water interacting with different surfaces. The phonon density of states are projected to show the spectrum of the molecules on the PbO terminated surface, and TiO_2 terminated surface separately, and the results up to these simulation times are shown in Fig. 49. The main difference between these vibrational density of states emerge when the dissociation events start. This can already be seen in the difference of the stretching frequencies of the water molecules on the TiO_2 terminated surface when the slab is $+\hat{z}$ polarised. The stretching frequencies of the water molecules interacting with the TiO_2 surface is larger,

mainly due to the existence OH^- ions. Longer simulations will allow more water molecules to dissociate on this surface, making this difference between the vibrational density of states more clear.

C.4 Conclusion and Future Work

In this section, an ongoing project of the investigation of the $PbTiO_3$/water inferface has been introduced. Four different configurations for two different slab thickness of one or two layers have been analysed. These configurations have perovskite structure with $+$ or $-\hat{z}$ polarisation, or cubic structure without any polarisation. The periodicity of the configuration is such that it allows us to analyse how water interacts with two possible interfaces: one interface is PbO terminated, while the other is TiO_2 terminated.

The results with the PBE functional show that the perovskite with high tetragonality and large dipole moment is not stable when the thickness of the slab is one or two layers. This instability is reduced when the functional is changed to the vdW-DF-cx functional, which brings the tetragonality of the bulk perovskite closer to the experimental values.

More importantly, these reveal that the TiO_2 terminated surface is more hydrophilic than the PbO terminated surface. There is a clear separation of water and the PbO terminated surface, making this surface more hydrophobic compared to the TiO_2 terminated surface. There are molecular adsorption events already happening with the TiO_2 surface regardless of the thickness of the slab. Moreover, there exists dissociation of water molecules on this surface.

Now, the AIMD simulations of these systems with the vdW-DF-cx functional are performed. These simulations need to continue for longer times, before more water molecules dissociate on the interfaces. In the future, we aim to quantify our investigation of the structural changes in the liquid water under the external dipole moment from the perovskite $PbTiO_3$ slab. As shown in the preliminary plots, we will analyse how the vibrational spectrum of the liquid water, especially with the focus on the stretching modes of the OH covalent bond, differ as the interaction is clearly different with different surfaces. Another possible future analysis is to check the changes in the dipole moment of the water molecules along the $\hat{z}$ direction, and make links to other work that has been performed in our group. We hope to keep our collaboration active for this project and other future projects to come...